



THE UNIVERSITY OF SYDNEY
SCHOOL OF AEROSPACE, MECHANICAL AND MECHATRONIC ENGINEERING
AERO4701 SPACE ENGINEERING 3

LUNATICS

Critical Design Review

Authors:

Kelly Chen	520439977	kche4214@uni.sydney.edu.au
Austin Cleary	520481220	acle6540@uni.sydney.edu.au
Elise (Ellie) Deveson	520452507	edev3158@uni.sydney.edu.au
Joshua Dickford	520455047	jodi7575@uni.sydney.edu.au
James Hocking	520461831	jhoc6907@uni.sydney.edu.au
Jasmine Khuu	520472790	jkhu7518@uni.sydney.edu.au
Aum Mehta	520422898	ameh3151@uni.sydney.edu.au
William Ridley-Smith	520466021	wrid7227@uni.sydney.edu.au

Contents

List of Figures	iv
List of Tables	vii
Nomenclature	ix
Acronyms	xi
1 Introduction	1
1.1 Background	1
1.2 Vision	2
1.3 Orbital Parameters	2
2 System Overview	3
2.1 Component Overview	3
2.1.1 OBC	3
2.1.2 ADCS	5
2.1.3 Structure	5
2.1.4 Power	6
2.1.5 Communications	6
2.1.6 Payload	7
2.1.7 Thermal	7
3 Payload Design	8
3.1 Scientific Justification	8
3.2 Component Overview	9
3.2.1 Technical Specifications of AS7265x Sensor	11
3.3 Expected Results & Scientific Application	12
3.3.1 AS7265x Sensor Processed Test Output	14
3.3.2 Mock Atmospheric Composition Determination Model	14
3.4 Data Collection	16
4 Structural Subsystem	17
4.1 Material Choices	17
4.2 Chassis Design	17
4.2.1 Ease of Manufacture	19
4.2.2 Joints	20
4.2.3 Ease of Assembly	20
4.3 Structural Design (Internal Components)	21
4.3.1 ADCS Magnetorquer Assembly	21
4.3.2 PCB Assembly	22
4.3.3 EPS Assembly	22
4.3.4 Payload Assembly	23
4.3.5 Sun Sensor Assembly	23
4.3.6 Communications Assembly	24
4.3.7 Deployment Switch Mechanism	24
4.3.8 Nichrome Release Mechanism	24
4.3.9 Mass Budget	25
4.3.10 Centre of Gravity	26
4.4 Finite Element Analysis	27
4.4.1 Quasi-static Acceleration	29
4.4.2 Natural Resonance Frequency	30



4.4.3	Sinusoidal Vibration	31
4.4.4	Random Vibration	33
4.4.5	Shock Loads	34
4.4.6	Conclusion of Structural FEA Results	36
5	Attitude Determination and Control	38
5.1	Overview	38
5.1.1	Modes of Operation: ADCS	38
5.2	Attitude Determination System	38
5.2.1	IMU	38
5.2.2	Sun Sensor System	42
5.2.3	Attitude Determination Algorithm	45
5.2.4	Quaternion Estimator	45
5.2.5	Extended Kalman Filter	47
5.3	Attitude Control System	52
5.3.1	Magnetorquers	52
5.3.2	Detumbling Algorithm (B-Dot)	55
5.3.3	Nadir Pointing Algorithm (PID)	58
6	Electrical Power Subsystem	63
6.1	Overview	63
6.2	Block Diagram	63
6.3	Components	63
6.3.1	Solar Panels	64
6.3.2	Batteries	65
6.3.3	Reverse-Polarity Protection Circuit	66
6.3.4	Solar Charge Controller Circuit	67
6.3.5	Battery Protection Circuit	68
6.3.6	Voltage Regulation Circuit	69
6.3.7	Current Sensing Circuit	70
6.3.8	Kill-Switch	70
6.4	PCB Design	70
6.5	Power Budget	70
6.5.1	Power Generation Analysis	71
6.5.2	EPS Power Consumption	71
6.5.3	OBC Power Consumption	72
6.5.4	ADCS Power Consumption	72
6.5.5	Comms Power Consumption	72
6.5.6	Payload Power Consumption	73
7	On-Board Computer and On-Board Data Handling Subsystem	74
7.1	Overview	74
7.2	PCB Design	74
7.2.1	PCB Dimensions	74
7.2.2	PCB Stack	76
7.2.3	Trace Width	76
7.2.4	PCB and Structural Grounding	77
7.2.5	Connectors	77
7.2.6	Design For Assembly	78
7.2.7	Design For Debugging	79
7.2.8	PCB Component Placement and Routing	79
7.2.9	Conformal Coating	80
7.3	OBC Components	81



7.3.1	Main Board and Mini Board	81
7.3.2	Watchdog	82
7.3.3	Real Time Clock	82
7.3.4	Analog to Digital Converter	82
7.3.5	I2C Multiplexer	83
7.4	OBC Validation	83
7.5	Bus Connections	84
7.6	Modes of Operation	85
7.7	Code Structure	86
7.8	Data Budget	87
7.8.1	Uplink Data	88
7.8.2	Downlink Data	88
8	Communication Subsystem	90
8.1	General Information	90
8.2	Uplink	90
8.3	Downlink	91
8.4	Testing	91
8.5	Link Budgets	93
8.5.1	Uplink	93
8.5.2	Downlink	94
8.5.3	Link Budget Assumptions	94
9	Thermal Subsystem	97
9.1	Overview	97
9.2	Thermal Design Objectives	97
9.3	Thermal Environment	97
9.4	Temperature Cycles for 4 Orbital Periods	98
9.5	Thermal Temperatures of Components	98
9.6	Finite Element Analysis	99
9.6.1	Thermal Vacuum Cycling	99
9.6.2	Thermal Vacuum Bake-Out	101
9.7	Thermal Controls	102
References		103
A	Mission requirements	106
A.1	CubeSat System Requirements	106
A.2	Payload Requirements	113
B	Appendix	114
B.1	CubeSat Reference Frame	114
B.2	QUEST Variable Definitions	114
B.3	External Disturbance Justification [1]	115
B.4	B-Dot Supplementary Simulations	116
B.5	TRL Definition	117
B.6	FCS Calculation	118
B.7	Data Downlink Storage	118
B.8	Code repository	119
B.9	Electrical Diagrams	119
B.10	CubeSat Overview Spreadsheet	124



List of Figures

1	Render of LUNATICS-0 without solar panels.	1
2	LUNATICS-0 TLE	2
3	Overall system design	3
4	Distribution of XCO ₂ measured by OCO-2 from 10/2015 to 03/2016 [2].	8
5	The AS7265x multi-spectral sensor [3].	9
6	AS7265x full 18-channel spectral responsivity [3].	10
7	Spectral response of the three individual sub-sensors in AS7265x [3].	10
8	AS7265x LGA average field of view [3].	11
9	Block diagram for the AS7265x chipset [3].	12
10	Atomic absorption spectrum for the Sun with intensities [4].	13
11	Intensity and absorption spectrum for test recording.	14
12	Mock model set-up.	15
13	Mock model with forced complete atmospheric “absorption.”	15
14	Mock model with variation in element absorption intensities.	16
15	Schematic for the connector for the payload	16
16	Main Panel with payload section (Panel 1).	18
17	Main Panel without payload (Panel 2).	18
18	Cross side Panels.	18
19	Top end cap.	19
20	Bottom end cap.	19
21	Internal Layout	21
22	ADCS assembly.	21
23	PCB assembly.	22
25	Battery assembly.	22
24	Solar panel assembly.	23
26	Payload assembly.	23
27	Sun sensor assembly.	24
28	Antenna assembly	24
29	Deployment mechanism.	25
30	Point of Origin and Coordinate System	27
31	Simplified CAD model used in the FEA.	28
32	The location of the fixed support boundary conditions.	29
33	Location of maximum stress under quasi-static loads	30
34	Location of maximum deformation under quasi-static loads	30
35	Maximum deformation under the 683.05 Hz load	31
36	Location of maximum stress under sinusoidal vibration loads	32
37	Location of maximum deformation under sinusoidal vibration loads	33
38	Location of maximum stress under random vibration loads	34
39	Location of maximum deformation under random vibration loads	34
40	Location of maximum stress under shock loads	35
41	Location of maximum deformation under shock loads	36
42	Location of maximum stress under shock loads	37
43	Testing Setup for the BNO085 IMU	39
44	Euler Angles Obtained from BNO085 IMU Test	39
45	Quaternions Obtained from BNO085 IMU Test	40
46	Calibrated Acceleration Obtained from BNO085 IMU Test	40
47	Calibrated Gyroscope Obtained from BNO085 IMU Test	41
48	Magnetic Field Strength Obtained from BNO085 IMU Test	41
49	VEML7700 Testing	42
50	VEML7700 measured relative sensitivity vs. angular displacement [5].	43
51	True vs Estimated q_0 from EKF	50



52	True vs Estimated q_1 from EKF	50
53	True vs Estimated q_2 from EKF	50
54	True vs Estimated q_3 from EKF	50
55	True vs Estimated w_x from EKF	51
56	True vs Estimated w_y from EKF	51
57	True vs Estimated w_z from EKF	51
58	Error in Estimated Euler Angles Derived from EKF Quaternions	51
59	Magnetorquer Assembly	52
60	Magnetorquer winding setup	53
61	Magnetorquer Testing Procedure and Setup	53
62	Magnetorquer measurement and Z-Axis Results	54
63	Magnetorquer Testing X and Y Axis Results	55
64	IGRF model of Earth's magnetic field dipole along the orbit in ECI frame	56
65	B-Dot detumbling simulation with $k_{bdot} = 5000$, $I_{sat} = 0.5$ and an initial tip-off rate of 60 deg/s	57
66	B-Dot detumbling simulation with $k_{bdot} = 5000$, $I_{sat} = 0.5$ and a large tip-off rate in excess of 100 deg/s	58
67	MATLAB Simulink model of the PID Nadir-Pointing controller	60
68	Interior view of PID controller block in Simulink.	60
69	PID Nadir-pointing controller simulation with parameters from Table 27	62
70	PID Nadir-pointing controller simulation with K_i increased 5-fold	62
71	Block diagram of the EPS	63
72	Solar panel circuitry including current sensing and reverse polarity protection	64
73	Experimentally obtained Power-Voltage and Current-Voltage curves of a single solar panel	65
74	Discharge curve of the INR18650-35 Li-Ion Battery	66
75	EPS Solar panel reverse polarity protection circuit diagram, the P-MOS terminal 1 is connected to the solar panel positive terminal, and P-MOS terminal 4 connected to the load	66
76	Reverse polarity protection circuit simulation in LTSpice	67
77	EPS Solar power charge controller circuit diagram	68
78	EPS Battery protection circuit diagram	68
79	Efficiency versus output current (A) for TPS63060 voltage regulator	69
80	EPS 3.3V voltage regulator circuit diagram	69
81	EPS Current sensing circuit diagram	70
82	Kill switch circuitry for the solar panels and batteries	70
83	Solar power generation by the solar panels over two full orbital periods	71
84	PCB Stack	74
85	PC/104 Outline Dimensions [6]	75
86	PC/104 Stack Dimensions [6]	75
87	PCB Stack Diagram	76
88	PCB Connector Types	78
89	Labelled Connector and Cable Cut-out	78
90	LED Indicators On PCB	79
91	EPS PCB	79
92	ADCS PCB	80
93	OBC PCB	80
94	Main OBC and ADCS Microcontroller selection	81
95	Watchdog Operation [7]	82
96	DS3231 MEMS Precise RTC [8]	82
97	I2C Multiplexer Diagram [9]	83
98	Main OBC and ADCS Microcontroller selection	83



99	ROS Topics - this is how software modules communicate with each other. In this diagram, an arrow leaving a node means it is publishing and an arrow entering a node means it is subscribing.	84
100	Communication Protocols used within LUNATICS-0	85
101	State Machine, showing the modes of operations	85
102	Ground trace showing the visibility of the satellite from the ground station. Green and Red traces are used to represent in view and not in view respectively	90
103	Assembly instructions from Gomspace for the ANT430 Antenna	91
104	Testing the RP02W, communicating using TCP sockets	92
105	Atmospheric Loss as a function of frequency [10]	95
106	Temperature profiles at the central point of each external face are shown for the most extreme conditions over four orbital cycles. The left side illustrates the coldest case scenario, while the right side depicts the hottest case.	98
107	Finite Element Analysis model showing the temperature distribution at the peak of the cyclic thermal test.	99
108	Finite Element Analysis model showing the temperature distribution at the trough of the cyclic thermal test.	100
109	Finite Element Analysis model showing the temperature distribution throughout the cyclic thermal test.	100
110	Finite Element Analysis model showing the temperature distribution at the end of the thermal test.	101
111	Finite Element Analysis model showing the temperature distribution throughout the bake-out thermal test.	102
112	CubeSat reference frame	114
113	B-Dot Detumbling Simulation 1	116
114	B-Dot Detumbling Simulation 2	116
115	B-Dot Detumbling Simulation 3	117
116	B-Dot Detumbling Simulation 4	117
117	Consecutive Times of Visibility	118



List of Tables

1	LUNATICS-0 orbital parameters	2
2	Overview of the OBC Components	4
3	Overview of ADCS Components	5
4	Overview of Structural Components	5
5	Overview of Electrical Components	6
6	Overview of Communications Components	6
7	Overview of Payload Components	7
8	Overview of Thermal Components	7
9	Optical characteristics & wavelength channels for the AS7265x sensor [3].	11
10	Technical specifications of the AS7265x sensor.	12
11	Science Structure	16
12	Material Properties Comparison: Carbon Fibre Nylon (CFN) vs. Aluminium 6061-T6 [11] [12]	17
13	Material Properties of M3 Screws and M3 Bolts (Structural Steel) [13]	20
14	CubeSat Component Mass Breakdown	26
15	Simplified CAD components for FEA and their materials	28
16	Quasi-static acceleration results	29
17	Modal Analysis	31
18	Sinusoidal vibration results	32
19	Random vibration results	33
20	Shock results	35
21	FEA maximum stress and deformation results	36
22	Rotation angles for each sun sensor.	43
23	Validation of NLLS Sun direction estimation with clean and noisy readings.	45
24	Sensor Noise Variances	50
25	Magnetorquer Design Summary	52
26	Magnetorquer Testing Results	55
27	PID Controller Parameters	61
28	EPS Component Summary	64
29	EPS Component Power Usage Across Modes of Operation	71
30	OBC Component Power Usage Across Modes of Operation	72
31	ADCS Component Power Usage Across Modes of Operation	72
32	Comms Component Power Usage Across Modes of Operation	72
33	Comms Component Power Usage Across Modes of Operation	73
34	AX.25 UI-Frame Format [14]	87
35	Heartbeat Data	88
36	Override Data	88
37	Single WOD reading	88
38	Whole Orbit Data Packet structure	89
39	WOD Data for Ax.25 frame	89
40	Science Structure	89
41	Science Data	89
42	Uplink budget parameters for the CubeSat ground-to-spacecraft communication link. .	93
43	Downlink budget parameters for the CubeSat spacecraft-to-ground communication link.	94
44	CubeSat Component Thermal Breakdown	98
45	Structural system requirements.	106
46	Attitude & Orbit Control Subsystem (AOCS) requirements.	107
47	Electrical Power System (EPS) requirements.	108
48	Onboard Computer & Data Handling (OBC/OBDH) requirements.	109
49	Telemetry, Tracking & Command (TT&C) requirements.	110
50	Thermal Control Subsystem Requirements	111



51	General system requirements.	112
52	Science and payload mission requirements.	113
53	External Torque Disturbances	115



Nomenclature

$\alpha(\lambda)$	Absorption Coefficient
α_s	Absorptivity of the satellite
ΔT	Trace temperature rise
ϵ_{IR}	Emissivity of satellite surface
η	Photo diode quantum efficiency
η_P	Panel Efficiency
\hat{I}	Normalised intensity of light
λ	Wavelength
λ_M	Magnetic Latitude
μ	Earth's Gravitational Constant
μ_M	Magnetic Dipole
ϕ	Solar Flux
Φ_e	Incident radiant flux
ϕ_{sun}	Solar Flux at Earth
ρ	Albedo Coefficient
ρ_A	Air Density
σ	Stefan-Boltzmann Constant
$\tau_{applied}$	Applied Torque
τ_{max}	Total External Torque
θ	Angle from Z principal axis and the local vertical
θ_e	Pointing Error
θ_r	Angle between the reflected radiation direction and the normal of the satellite panel
θ_{3dB}	Half power bandwidth
ε	Molar absorption coefficient
ε_0	Vacuum permittivity
ε_r	Relative permittivity
φ	Angle of incidence of the sun
A	Absorbance
A	Detector active area
A_L	Loop Area
A_p	Plate area
A_r	Ram Area
A_T	Total surface area of the satellite
A_t	Trace cross-sectional area
$A_{incident}$	Panel area facing Sun
B	Magnetic Field Strength
C	Concentration of element
c	Speed of light
C_d	Drag Coefficient
D	Antenna Diameter
d	Clock drift rate
d_p	Distance between plates
d_{max}	Maximum clock drift rate
E_b	Energy per Bit
E_g	Band Gap Energy
E_γ	The Energy of a photon
f	Frequency
g	Gain factor
G_r	Receiver Antenna Gain
G_t	Transmitter Antenna Gain
H	Angular moment



h	Planck's Constant
I	Current
$I(\lambda)$	The transmission intensity of light
$I_0(\lambda)$	The initial intensity of light
I_P	Generated photocurrent
I_{SAT}	The reverse saturation current
I_{yy}	Moment of inertia about Y axis
I_{zz}	Moment of inertia about Z axis
k_B	Boltzmann Constant
L	Luminosity
l	Light path length
L_P	Path length of the medium
L_r	Receiver Line Loss
M	Magnetic constant around Earth
N	Number of Coils
N_0	Noise Spectral Density
P	Power
P_l	Incident light power
P_r	Received Signal Power
P_t	Transmitter Power
P_{max}	Maximum Power
P_{panel}	Power Production
q	Elementary Charge
Q_a	Heat Transfer Reflected Radiation
Q_s	Heat Transfer Direct Radiation
q_s	Solar Heat Flux
Q_{IR}	Heat Transfer from Earth's Infrared Radiation
R_λ	Responsiveness of the photo diode at a given wavelength
R_B	Upper bound bit rate
R_D	Data rate
R_E	Radius of Earth
T	Temperature
t	Copper thickness
T_a	Torque from atmospheric drag
T_g	Torque from gravity gradient
T_m	Magnetic Field Torque
T_s	System Noise Temperature
T_∞	Ambient temperature of space
T_{drift}	Clock drift
T_{Earth}	Temperature of Earth's surface
T_{max}	Maximum amount of consecutive time without satellite visibility
T_{min}	Minimum amount of consecutive time with satellite visibility
V_A	Applied bias voltage
V_{in}	Voltage Input
v_{max}	Maximum speed of the satellite
W	Trace width



Acronyms

ADC Analog to Digital. 9, 66

ADCS Attitude Determination and Control System. 5, 57, 76, 79, 81, 83, 106, 113

AIT Assembly, Integration, and Testing. 106–110, 112, 113

AML Antenna Alignment Loss. 95

BPSK Binary Phase-Shift Keying. 90

CDR Critical Design Review. 106, 107, 109–113

COG Centre of Gravity. 106

COM Centre of Mass. 115

COMMS Communications System. 110, 113

COP Centre of Pressure. 115

COTS Commercial-Off-The-Shelf. 63

DoD Depth-of-Discharge. 65

EIRP Equivalent Isotropic Radiated Power. 94

EPS Electronics and Power System. 6, 63, 76

FCS Frame Check Sequence. 87

FSPL Free-Space Path Loss. 94, 95

FWHM Full Width at Half Maximum. 9, 14

GPIO General Purpose Input/Output. 82

HDRM Hold-Down and Release Mechanism. 24

IC Integrated Circuit. 79, 83

IGRF International Geomagnetic Reference Field. 56

IMU Inertial Measurement Unit. 72, 76

ISRU In-Situ Resource Utilisation. 1, 2

LEO Low Earth Orbit. 55, 65, 115

MOSFET Metal-Oxide-Semiconductor-Field-Effect-Transistor. 64, 66, 68

MPP Maximum Power Point. 65

NLLS Non-linear Least Squares. 43–45

OBC On-Board Computer. vii, 3, 4, 66, 70, 72, 74, 82, 109



- PAA** Polarisation Loss and Atmospheric Absorption Loss. 95
- PCB** Printed Circuit Board. 74, 76, 77, 79, 80, 83
- PCHIP** Piecewise Cubic Hermite Interpolating Polynomial. 14
- PD** Proportional Derivative. 58
- PDR** Preliminary Design Review. 106, 110, 112, 113
- PID** Proportional-Integral-Derivative. 58
- PWM** Pulse Width Modulation. 52
- RBF** Remove-Before-Flight. 63, 70
- RP02W** Raspberry Pi Zero 2 W. vi, 16, 76, 81–83, 91, 92
- RPP2W** Raspberry Pi Pico 2 W. 42, 76, 81, 84, 86
- RTC** Real Time Clock. 76, 82
- SPST** Single-Pole Single-Throw. 63, 70
- SRP** Solar Radiation Pressure. 115
- TLE** Two-Line Element. iv, 2
- TRL** Technology Readiness Level. 81
- TT&C** Telemetry, Tracking and Command. 6
- UTC** Coordinated Universal Time. 109
- WOD** Whole Orbit Data. vii, 88, 89, 109, 110, 119



1 Introduction

1.1 Background

Although spacecraft have been orbiting the Moon since the 1960s, the nature of its exosphere is still yet to be completely understood. Unlike the thick atmosphere of Earth, the Moon's exosphere consists of particles that are loosely bound by gravity and only minimally interact with one another. In spite of this, the exosphere holds valuable insights about the processes shaping both the Moon and other thinly-atmosphered bodies in our solar system and beyond.



Figure 1: Render of LUNATICS-0 without solar panels.

There are several key insights that can be gained from studying the concentration and composition of gases in the lunar exosphere. Firstly, the sources and sinks of gases can be observed. This would allow scientists to determine whether they originate from solar wind interactions, micrometeorite impacts, or outgassing from the lunar interior, enabling them to further understand the dynamic processes that continue to shape the Moon's environment. Secondly, understanding the exosphere is a key step for future lunar exploration and potential future long-term habitation. Gasses such as Hydrogen, Helium, and water vapour could be valuable resources used for In-Situ Resource Utilisation (ISRU), a process where local natural resources are used at mission destinations instead of taking all necessary supplies from Earth. Furthermore, characterising the variability and behaviour of these gasses would improve the design of instruments and systems to ensure they can operate reliably on the lunar surface.

1.2 Vision

To demonstrate and validate our sensing capabilities in a controlled and accessible environment our first satellite, LUNATICS-0, will orbit the Earth in LEO at approximately 550 km altitude. The primary goal of this mission is to act as a pathfinder for future lunar missions by developing, testing and refining our sensor technology and data analysis techniques in preparation for deployment in a lunar orbit.

During the Earth phase, the primary gases of interest will be Oxygen (O_2), Helium (He), Hydrogen (H_2) and Nitrogen (N_2) because of their presence in the Earth's upper atmosphere and the partial overlap with the lunar exosphere. In particular, Helium and Hydrogen are common to both environments, making them key targets for instrument calibration and testing. Although Oxygen is not a major component of the moon's exosphere it is the most abundant species at LEO and presents an ideal test case for evaluating the performance of the spectral sensors.

During the Moon phase the gases of interest will be Helium (He), Argon-40 (^{40}Ar), Hydrogen (H_2), Sodium (Na) and Potassium (K) because these elements have previously been detected in missions such as LADEE (Lunar Atmosphere and Dust Environment Explorer) and Apollo 17's Lunar Mass Spectrometer. Furthermore helium and hydrogen can be used to create a calibration bridge between the Earth and Lunar missions as well as to validate the overall performance and accuracy of our payload design.

Our long-term vision is to launch a dedicated lunar orbiter equipped with evolved versions of the LUNATICS-0 payload, capable of mapping the spatial and temporal distribution of gases in the lunar exosphere. This mission would offer new insights into space weathering, atmospheric evolution and the feasibility of lunar ISRU. This would build on the previous work conducted by Chandrayaan-2 and the NASA Artemis program.

1.3 Orbital Parameters

Based on evaluations and trade studies conducted in the PDR, the orbital parameters that LUNATICS-0 will follow whilst in orbit around the Earth are outlined in Table 1. The Two-Line Element (TLE) for LUNATICS-0 is presented in Figure 2.

Table 1: LUNATICS-0 orbital parameters.

Parameter	Value	Units
Apogee	558	km
Perigee	557	km
Inclination	98.4	degrees
Orbital period	95.8	minutes
Eccentricity	5.58×10^{-5}	–
Right ascension	33.7	degrees
Argument of perigee	108.7	degrees

LUNATICS-0
1 40074U 14037F 26183.18100000 .00022035 00000+0 16321-2 0 9999
2 40074 98.3845 33.7289 0000558 108.6906 251.4378 15.03149846579994

Figure 2: LUNATICS-0 TLE



2 System Overview

The system design for LUNATICS-0 is shown in Figure 3. This diagram includes both power connections as well as data connections between the different subsystems. Apart from this high level diagram, each subsystem and connection will be expanded upon in further detail throughout this report.

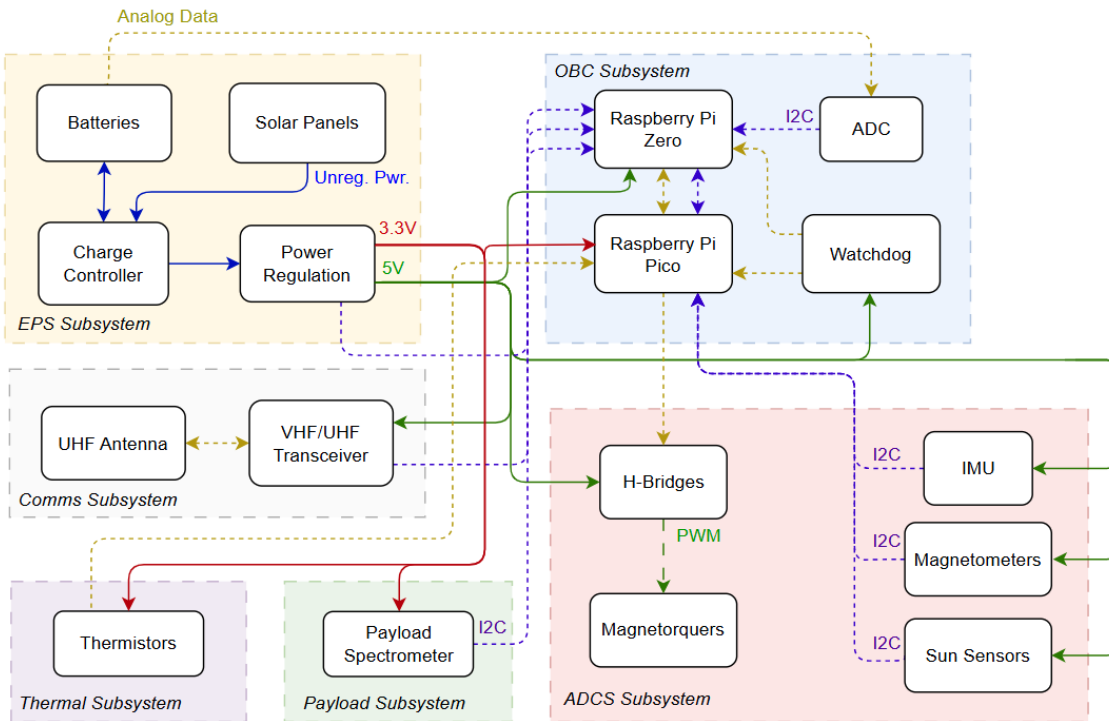


Figure 3: Overall system design

The two power rails (3.3V and 5V) that are generated from the power subsystem disperse to all peripheral components within the system making sure that safe, sufficient power is supplied. Data connections between each component utilise protocols such as I2C, SPI and GPIO in order to pass information throughout the system, which is explored in detail in Section 7.

2.1 Component Overview

LUNATICS-0 is made of the subsystems outlined in Figure 3. For each of these components, the provider, market ID and TRL has been included in the following group of tables. TRL is a measurement of the maturity of a particular technology, with each level 1-9 described in more depth in Appendix B.5.

2.1.1 OBC

The OBC subsystem manages all of the on-board electrical components, receiving data, performing computations and sending commands to each module. It also monitors the health of the main on-board controllers, restarting the system if necessary.

Table 2: Overview of the OBC Components

Name	Description	Provider	Market ID	TRL
On Board Computer	Central computing unit responsible for managing mission operations, data handling, and communication between all subsystems. Executes the main software controlling satellite functions.	Raspberry Pi	Raspberry Pi Zero 2 W	5
Micro Controller	A lightweight, low-power processor dedicated to handling the real-time operations of the \acrshort{adcs} system, interfacing with the required sensors and actuators	Raspberry Pi	Raspberry Pi Pico 2 W	5
PCBs	Custom-designed printed circuit boards that physically and electrically connect all electronic components, ensuring compact integration and reliable data and power distribution.	In-house/ PCBWay	Standard PCB	5
RTC	Provides accurate timekeeping functionality to support scheduled operations and data timestamping, even during power loss, ensuring mission reliability.	DF/Robot	DS3231M MEMS Precise RTC	7
Watchdog	Monitors system activity and automatically resets the microcontroller in the event of software malfunction or freeze, enhancing system robustness.	Maxim Integrated	MAX6369–MAX6374	7



2.1.2 ADCS

The ADCS assists with detumbling after the launch and ensures the spacecraft maintains nadir-pointing attitude throughout the orbit to assist payload operations. It utilises magnetorquers, sun sensors, and an IMU to maintain orientation.

Table 3: Overview of ADCS Components

Name	Description	Provider	Market ID	TRL
IMU	The IMU provides measurements of angular velocity and linear acceleration. High-rate rotational velocity estimates are accurate, but absolute attitude estimates drift over time without external corrections.	Adafruit	9-DOF Orientation IMU Fusion Breakout - BNO085	5
Sun Sensors	Sensors that measure the direction to the Sun, providing absolute attitude references with moderate accuracy. Typically less precise than IMUs in short timescales but essential for drift correction.	Adafruit	VEML7700 Lux Sensor	5
Magnetorquer	A set of electromagnetic coils that generate a magnetic moment, allowing the satellite to control its attitude by interacting with Earth's magnetic field. Passive, low-power actuation method.	In-house	N/A	3
H-Bridge	An electronic circuit that enables voltage to be applied across a load (e.g., magnetorquer coils) in either direction, allowing for full control of current flow for attitude actuation.	Texas Instruments	DRV8835 Dual Motor Driver Carrier	5

2.1.3 Structure

The Structural subsystem ensures the spacecraft's frame provides strength and rigidity while maintaining a lightweight design. It includes material selection, structural integrity assessments, and ensures the spacecraft can withstand environmental stresses.

Table 4: Overview of Structural Components

Name	Description	Provider	Market ID	TRL
Aluminium Frame	The external chassis structure which is used to protect and interface the internal components of the Cube-Sat.	In-house	Aluminium 6061-T6	4
Carbon Fibre Nylon Mounts	The mounts use to mount the payload spectrometer, sun sensors, magnetorquers and PCB stack internally to the aluminium frame.	In-house	Onyx base and carbon fibre composite	
Bolts, screws and stack separators	They are used to integrate all of the mounts, chassis frame and PCB's together.	Bolt & Nut Australia	A4-70 G316 Stainless Steel	



2.1.4 Power

The EPS subsystem is responsible for generating, storing and supplying adequate electrical power for operation of the satellite in all modes. Solar panels will be used to generate power, with batteries to store the excess. Buck and boost converters will be used to regulate power to other components on the board.

Table 5: Overview of Electrical Components

Name	Description	Provider	Market ID	TRL
Battery	Primary energy storage device, supplying power during eclipse periods and supporting peak load demands.	Samsung	INR18650-35E 3500mAh 8A Li-Ion Battery	4
Solar Panel	Photovoltaic module that harvests solar energy and converts it into electrical power to recharge the battery and power onboard systems.	Seeed	1W Solar Panel 80X100	4
Battery Protection	Circuit that safeguards the battery from overcharge, overdischarge, overcurrent, and short-circuit conditions to extend battery life and ensure safety.	ABLIC	S-82A2A/B/C Series	4
Voltage Regulators	Devices that maintain a stable and constant voltage level to various subsystems, protecting sensitive electronics from voltage fluctuations.	Texas Instruments	2.5-12Vin 2.25A Sw C rnt Limit A 595- TPS63060DSCT	4
Current and Power Monitors	Sensors that measure and report current flow and power consumption, enabling real-time monitoring of system health and efficiency.	Texas Instruments	0-Drift Bi- Dir Crnt Pwr Moni- tor A 595- INA219AIDCNT	4
Solar Charge Controller	Manages the charging of the battery from the solar panel, preventing overcharging and optimizing energy transfer.	Texas Instruments	A 595- BQ24650RVAT	4

2.1.5 Communications

The TT&C subsystem ensures reliable communication by downlinking telemetry and payload data to Earth-based ground stations. It also receives commands via uplink systems to establish connection and modify the spacecraft's operational state.

Table 6: Overview of Communications Components

Name	Description	Provider	Market ID	TRL
LoRaWAN Node	A low-power, long-range wireless communication module based on the LoRaWAN protocol. Enables data transmission over large distances with minimal power consumption, using the IoT network.	Waveshare	SX1262	4



2.1.6 Payload

The Payload subsystem includes a multi-channel visible to near-infrared optical spectrometer sensor, aimed at fulfilling the science objective of measuring the global geographic distribution of atmospheric elements.

Table 7: Overview of Payload Components

Name	Description	Provider	Market ID	TRL
Spectroscopy Sensor	A compact optical sensor capable of measuring the intensity of light across multiple wavelengths. Useful for detecting material composition, monitoring environmental conditions, or conducting scientific experiments by analyzing reflected or emitted spectra.	SparkFun	AS7265x	3

2.1.7 Thermal

The Thermal subsystem regulates the spacecraft's temperature through passive control systems, protecting sensitive equipment from extreme conditions while ensuring efficient heat dissipation and retention with minimal mass and power use.

Table 8: Overview of Thermal Components

Name	Description	Provider	Market ID	TRL
Thermistor	Temperature-sensitive resistor used for monitoring system thermal conditions	Vishay/Digikey	NTCLE100 E3103JB0	9
Mylar layers	Multilayer insulation (MLI) for passive thermal protection in spacecraft	DuPont/Thorlabs	MYLAR-MLI-01	9
Kapton Tape	Polyimide film with high thermal resistance, used for electrical and thermal insulation	DuPont / RS Components	KPT-1MIL-33M	9
Titanium Dioxide White	High-reflectivity white coating used for radiative thermal control	AZ Technology	MAP-TiO2-WHT	8



3 Payload Design

The overall goal of the LUNATICS mission is:

To gain a greater understanding of the concentration and distribution of elements within the Moon's atmosphere.

with the science objective of LUNATICS-0:

To validate the experimental method of elemental composition mapping using the Earth's atmosphere at LEO to mimic lunar exospheric density conditions.

To achieve this, LUNATICS-0 will orbit around the Earth and collect data across the entire atmosphere. This data must allow for the local identification of elements and their concentrations, as to then enable the generation of a “map” of element distribution. NASA’s Orbiting Carbon Observatory-2 (OCO-2) mission, which had a principal science objective “to retrieve a global geographic distribution of carbon dioxide sources and sinks,” generated a map of CO₂ concentration in the Earth’s atmosphere [2]. It is the aim of LUNATICS satellites to produce a similar map for all elements on both Earth and the Moon.

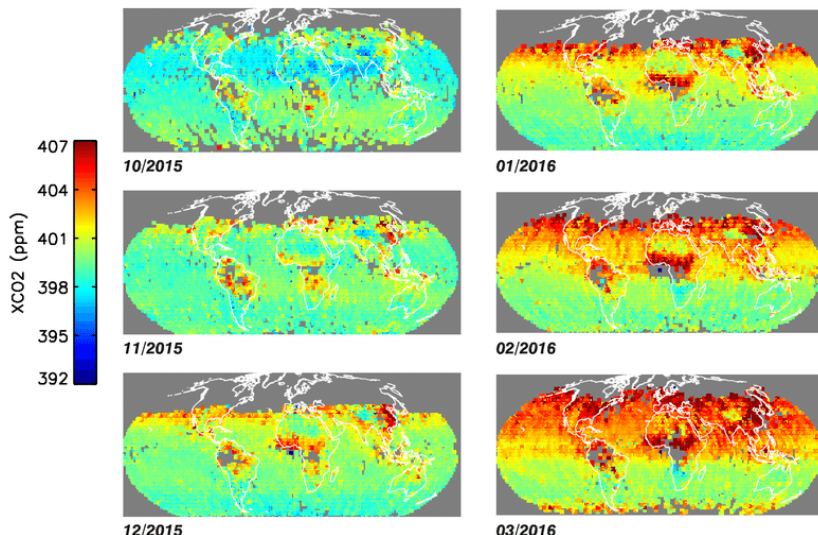


Figure 4: Distribution of XCO₂ measured by OCO-2 from 10/2015 to 03/2016 [2].

Due to the requirement of both elemental identification and concentration measurement, a payload that measures incident light intensity across the visible spectrum was required. From a trade study conducted in the PDR, it was determined that LUNATICS satellites will carry an optical spectrometer that detects light in the visible to near-infrared part of the spectrum. It will utilise the scientific basis/concept of atomic absorption to do this.

3.1 Scientific Justification

Each element is unique in its atomic structure, with the electrons within occupying discrete energy levels. When a photon is incident upon an atom, it may be absorbed if the photon’s energy, which is dependent on its wavelength λ , matches that of a difference between two allowable electron states. This photon energy, E_γ , is defined by the equation:

$$E_\gamma = hf = \frac{hc}{\lambda} \quad (3.1)$$

for frequency $f = c/\lambda$, speed of light $c \approx 3.0 \times 10^8 \text{ m s}^{-1}$, and Planck's constant $h = 6.626 \times 10^{-34} \text{ J s}$. As each element is distinct in its energy level structure, the specific photon wavelengths absorbable by each molecule will be unique, allowing for the characterisation of a "fingerprint" for each element.

The payload of LUNATICS satellites utilises the principle of optical/absorption spectroscopy to identify the presence, concentrations, and local distributions of gaseous elements in the atmosphere of the Earth, and eventually, the Moon. As broad-spectrum light, such as from the Sun (an approximate blackbody emitter), passes through a gaseous medium, such as an atmosphere, photons of wavelengths characteristic of present elements will be absorbed. The resulting spectrum will have certain discrete wavelengths of reduced intensity, allowing not only the identification of present elements, but also the determination of individual element concentrations.

It is upon this principle that LUNATICS-0 and its later iterations will be able to map the distribution of elements throughout the atmosphere of the Earth and the Moon.

3.2 Component Overview

The payload of LUNATICS-0 will consist of the *AS7265x Smart 18-Channel VIS to NIR Spectral-ID 3-Sensor Chipset with Electronic Shutter* (Figure 5). The AS7265x is a highly-integrated multi-spectral sensor, which is able to perform spectral identification in from the visible to near-infrared (NIR) wavelength range. It is comprised of three individual sensors: AS72651, AS72652, and AS72653, each with six photodiode channels. AS72652 and AS72653 utilise AS72651 as a controller [3]. The peak value and range of the wavelengths targeted by the individual sensors are listed in Table 9, and visualised across the spectrum in Figure 6 and Figure 7.

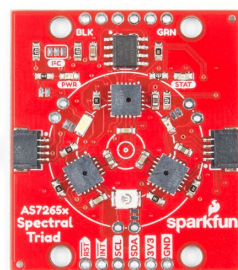


Figure 5: The AS7265x multi-spectral sensor [3].

The chipset operates by analysing light across the 18 distinct spectral channels, with the sensors employing Gaussian interference filters with a Full Width at Half Maximum (FWHM) of 20nm; this Gaussian response is visible in Figures 6 and 7. The data from each sensor is processed using a 16-bit Analog to Digital (ADC), allowing for measurement of light intensity across that channel.

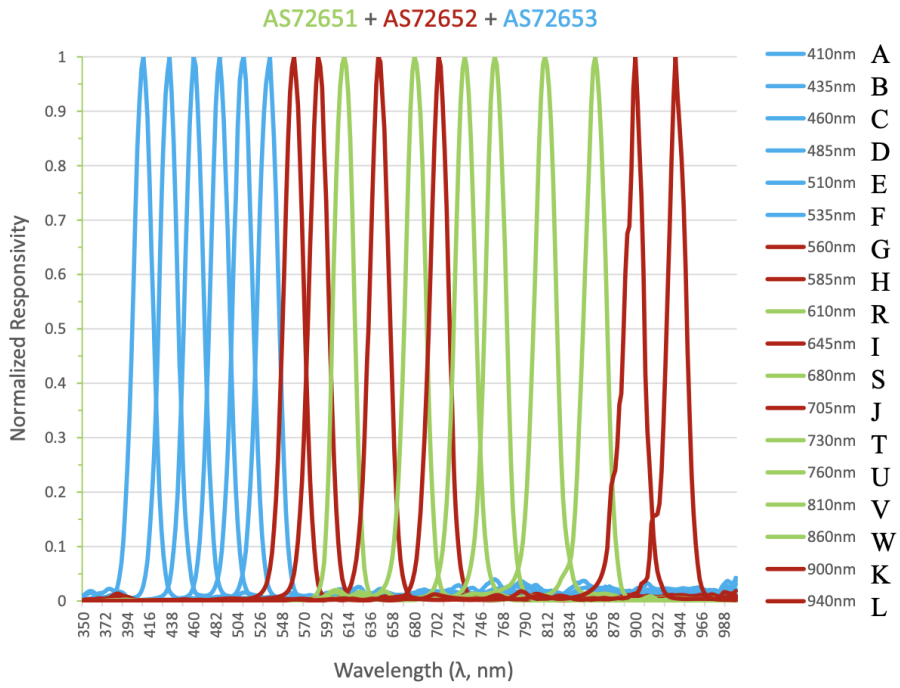


Figure 6: AS7265x full 18-channel spectral responsivity [3].

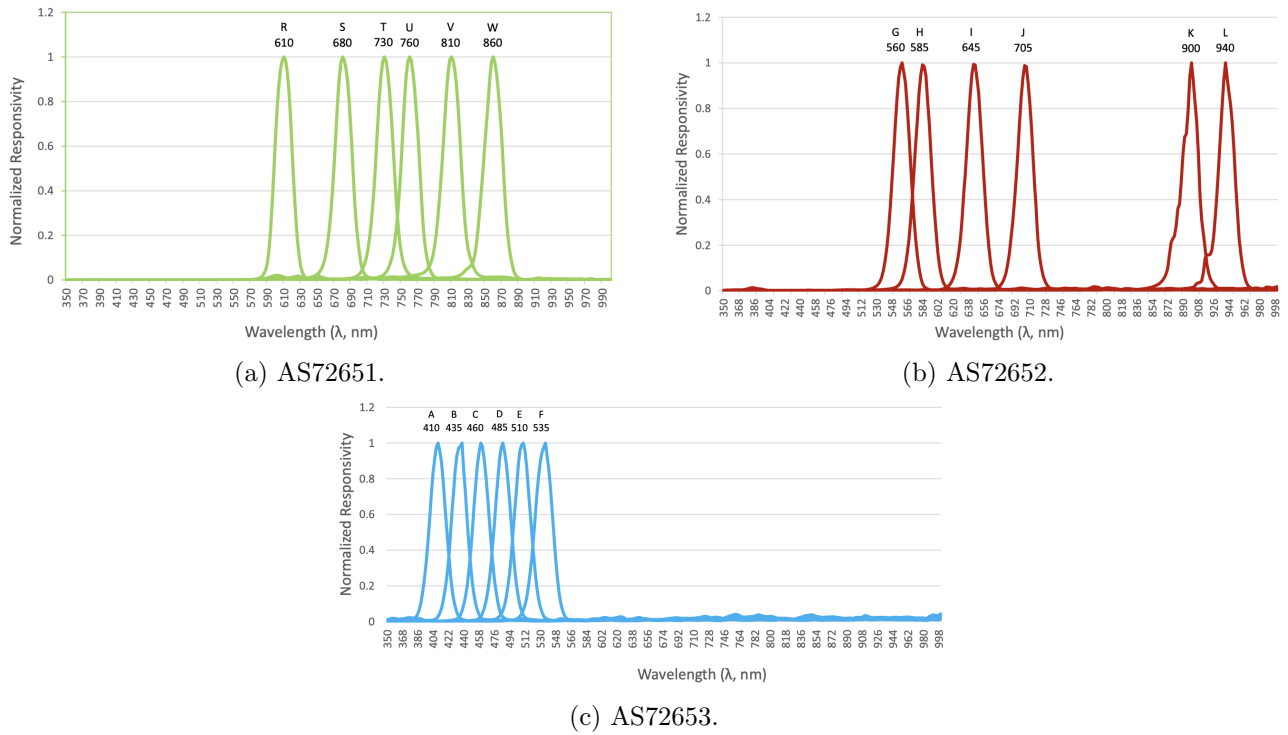


Figure 7: Spectral response of the three individual sub-sensors in AS7265x [3].

The sensors on the AS7265x have been pre-calibrated using specified standard light sources, ensuring reliable spectral measurements. However, as temperature variations can affect optical performance, each sensor has an integrated sensor that automatically compensates for temperature fluctuations in varying environmental conditions.

Data acquisition involves integrating light for a configurable period, a.k.a. *integration time*. The AS7265x supports both a continuous and single-shot data acquisition mode, both of which may and

Table 9: Optical characteristics & wavelength channels for the AS7265x sensor [3].

Sensor	Channel	Wavelength (nm)		
		Peak	Range (± 10)	FWHM
AS72651	R	610	600–620	
	S	680	670–690	
	T	730	720–740	
	U	760	750–770	20
	V	810	800–820	
	W	860	850–870	
AS72652	G	560	550–570	
	H	585	575–595	
	I	645	635–655	
	J	705	695–715	20
	K	900	890–910	
	L	940	930–950	
AS72653	A	410	400–420	
	B	435	425–445	
	C	460	450–470	
	D	485	475–495	20
	E	510	500–520	
	F	535	525–545	

will be utilised in the mission of LUNATICS-0.

The AS7265x has an average field of view of $\pm 20.5^\circ$ (41°), which allows for the light directly in front of the sensor to be monitored (see Figure 8), and a reasonably-sized swath-width to be employed based on the 558 km orbital altitude.

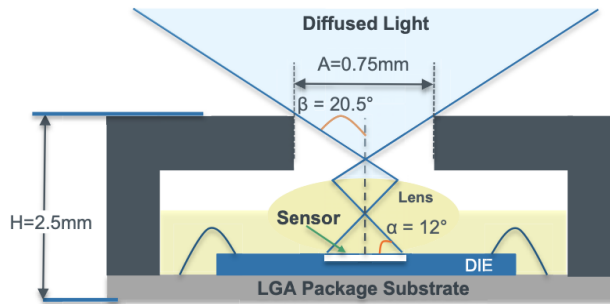


Figure 8: AS7265x LGA average field of view [3].

To achieve the science goal of elemental identification, a multi-spectral sensor with more channels would be required. Although the 18 channels of the AS7265x sensor allow for macro-level spectral identification, finer resolution is required in order to determine the specific values of the discrete wavelengths required for elemental identification. However, these fine-resolution optical spectrometers are costly and fall outside the budget for LUNATICS; therefore, the AS7265x sensor was chosen as a compromise for the LUNATICS-0 proof-of-concept. This concession in sensor resolution requires the testing of the payload system in relation to the science objective to be adapted and become a more conceptual, “mock” model.

3.2.1 Technical Specifications of AS7265x Sensor

The technical specifications of the AS7265x sensor are outlined in Table 10. The block diagram for the chipset is presented in Figure 9.

Table 10: Technical specifications of the AS7265x sensor.

Property	Value
Spectral wavelength range	410–950 (400–960) nm
Channels	18
Voltage	2.7–3.6 V
Current	5 mA
Operating temperature	−40°C–85°C
Field of view	±20.5° (41°)
Data output	16-bit digital via I ² C or UART
Accuracy	±12% of channel counts/μW/cm ²
Integration time	Configurable

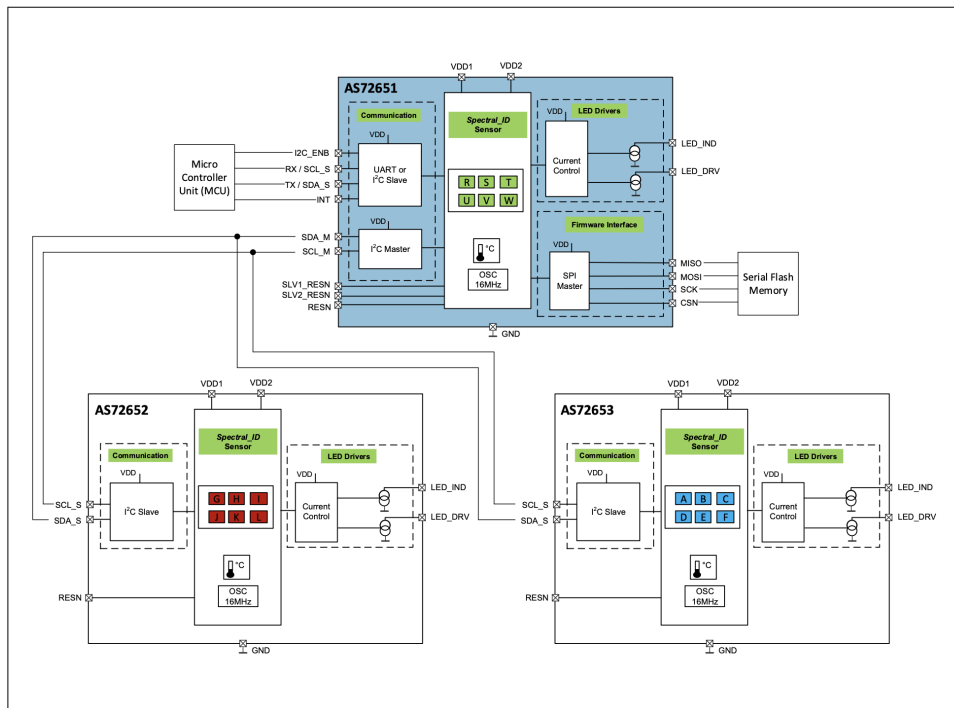


Figure 9: Block diagram for the AS7265x chipset [3].

3.3 Expected Results & Scientific Application

Across a limited “local” region of the atmosphere, the payload sensor will record the intensity of individual wavelengths across the range by measuring the photocurrent induced on multiple photodiodes that each correspond with a specific part of the visible-NIR spectrum. This allows for the creation of an *intensity spectrum*, which displays measured intensity against wavelength. An *absorption spectrum* can also be generated from this reading, which mimics the appearance of the sensor-incident light if it was expanded through a diffraction grating, allowing for the matching of fingerprint atomic absorption spectra.

To determine the concentration of specific elements in the atmosphere, we utilise the fact that diatomic Oxygen O₂ is uniformly distributed throughout the atmosphere with a known and well-documented concentration. To account for variations in incident light intensity at different times/locations throughout the orbits, we normalise the measured light intensities of all wavelengths $I(\lambda)$ about the measured intensity reading of a characteristic absorption wavelength for Oxygen:

$$\hat{I}(\lambda) = \frac{I(\lambda)}{I_{O_2}} \quad (3.2)$$

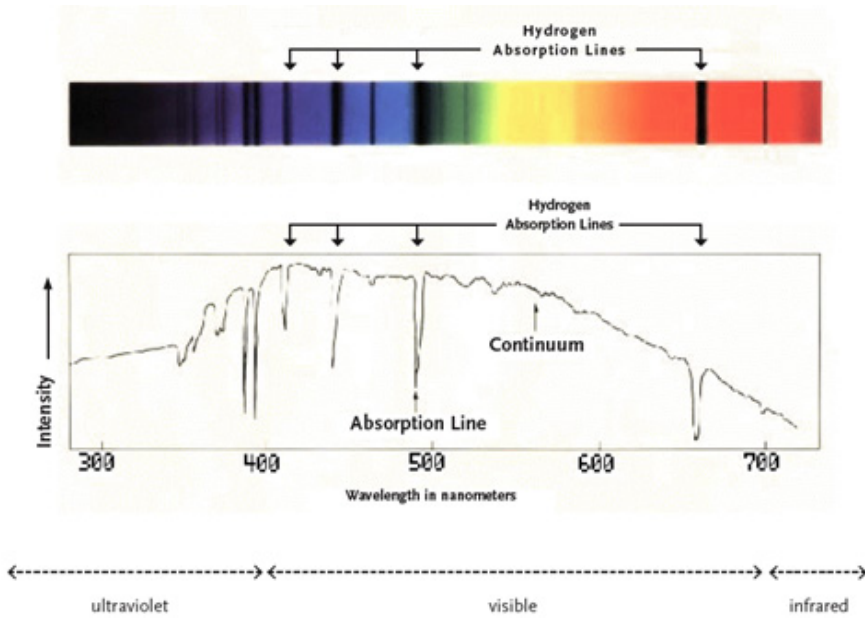


Figure 10: Atomic absorption spectrum for the Sun with intensities [4].

where \hat{I} is the normalised intensity reading. This process ensures that all readings are comparable across different Earth locations and times, as the reflected sunlight intensity varies across latitude due to diffusion, and due to the elliptical nature of Earth's orbit about the Sun.

The measured intensity of light is related to concentration through the absorbance relation and the Beer-Lambert law: The absorbance A is related to intensity of incident light I_0 and the intensity of transmitted light I by:

$$A = -\log_{10} \left(\frac{I}{I_0} \right) \quad (3.3) \qquad A = \epsilon Cl \quad (3.4)$$

where I_0 is the intensity of incident light, I is the intensity of transmitted light, ϵ is the molar absorption coefficient, C is concentration, and l is path length through the medium (i.e., twice the Earth's atmospheric thickness). These equations are then combined to give the equation for transmitted light intensity:

$$I = I_0 \times 10^{-\epsilon Cl} \quad (3.5)$$

From the normalised intensities, we get:

$$\hat{I}(\lambda) = \frac{I_0 \times 10^{-\epsilon_\lambda C(\lambda)l}}{I_0 \times 10^{-\epsilon_{O_2} C_{O_2} l}} \quad (3.6)$$

Taking the logarithms of both sides, we can calculate the concentration of any element based on its relation to the known molar absorptions and Oxygen concentration by:

$$C(\lambda) = \frac{\epsilon_{O_2}}{\epsilon_\lambda} C_{O_2} - \frac{\log_{10}(\hat{I}(\lambda))}{l \epsilon_\lambda} \quad (3.7)$$

Hence, at any location in the Earth's, or Moon's, atmosphere, we are able to identify present elements and determine their concentrations (relative and quantifiable), allowing for the generation of a “map” of elements and their distribution.

3.3.1 AS7265x Sensor Processed Test Output

The AS7265x was tested to check its functionality by measuring the ambient light conditions in a room. The results are presented as both an intensity spectrum and absorption spectrum in Figure 11. The individual readings as Gaussian curves with 20nm FWHM are presented, whilst the complete spectrum is plotted utilising Piecewise Cubic Hermite Interpolating Polynomial (PCHIP) interpolation.

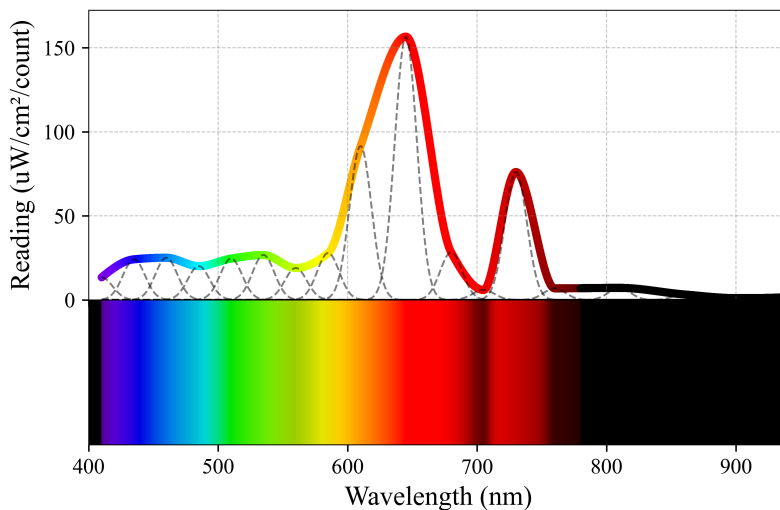


Figure 11: Intensity and absorption spectrum for test recording.

These spectra will be generated from the results back on Earth and analysed. The initial identification of elements in each atmospheric legion will be completed by either a human observer or machine-learning. Once key absorption line wavelengths have been identified, then an algorithm will be employed to determine the concentration distribution of all results.

3.3.2 Mock Atmospheric Composition Determination Model

Due to the low resolution of the AS7265x sensor, it is unable to accurately and precisely sense the absorption lines of gaseous elements. As such, a mock model of the atmospheric elemental composition determination method must be designed. This conceptual model will be used to test the scientific approach to modelling atmospheric composition based on sensor results, as well as to test the general functionality of the AS7265x sensor.

To begin, the resulting spectrum from shining “white” light (or reference light source) on the sensor will be recorded as control. Then, the resulting spectra from this source through different coloured transparent material (like cellophane) will be recorded; the coloured material should act as a filter, only allowing certain wavelengths to pass through, hence, simulating atomic fingerprint emission spectra.

For example, we consider coloured filters red, orange, yellow, green, blue, and purple, and utilise the set-up expressed in Figure 12. The emission spectra for these colours will correspond to the fake elements Redium (Re), Orangen (Or), Yellowine (Ye), Greenium (Gr), Blueogen (Bl), and Purpleum (Pu), respectively.

The absorption lines of a full-resolution spectrometer can be modelled by blocking certain wavelengths of light from passing through by removing certain filters from the array, hence removing those colours from the transmitted light (Figure 13). By analysing the resulting spectrum produced by the sensor, the missing wavelengths can be compared to the previously-determined emission spectra. If those wavelengths are not measured by sensor, then the corresponding elements must



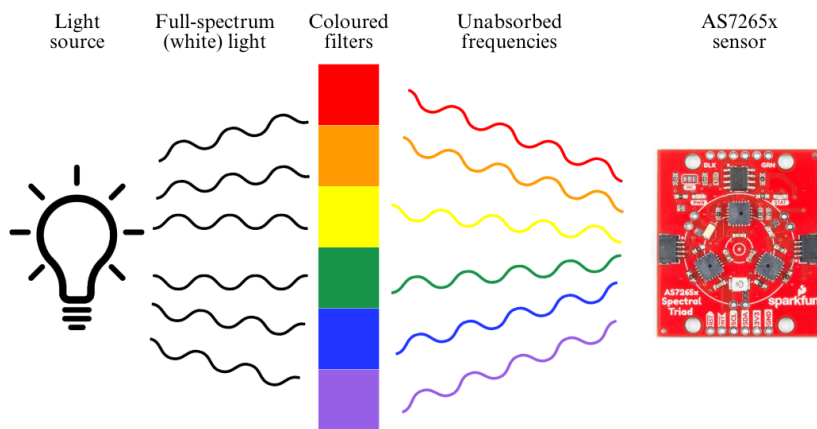


Figure 12: Mock model set-up.

exist in the atmosphere. In the case presented in Figure 13, only red, yellow, green, and blue light is recorded by the sensor, therefore, the atmosphere must consist of Orangen and Purpleium.

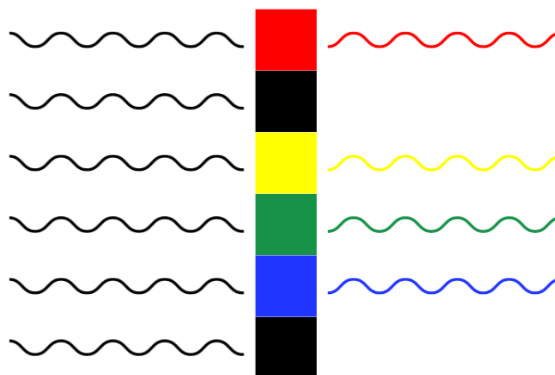


Figure 13: Mock model with forced complete atmospheric “absorption.”

The specific concentration of certain elements can also be modelled by varying the intensity/transparency of the coloured filters, which in turn, affects the intensity of transmitted corresponding wavelengths. We choose one colour/element as our reference element, which we will assume to have a known and constant concentration, acting the part of Oxygen in a real atmosphere. In the case of the mock model, Greenium will have a known concentration of C_{Gr} . The measured light intensities of key fingerprint wavelengths are compared to that of Greenium, to produce a relative intensity value of:

$$I_{\text{rel}}(\lambda) = \frac{I(\lambda)}{I_{\text{Gr}}} \quad (3.8)$$

This process accounts for varying incident light intensities, which is normalised by setting $I_{\text{rel},Gr} = 1.0$. The relative intensity is inversely-proportional to the amount of that particular element; a higher I_{rel} indicates a lower level of absorption by the atom, hence a lower C , whilst a lower I_{rel} indicates more absorption by the atom, and hence a higher C .

By a similar method as outlined previously for comparison-based concentration determination, and noting that Greenium serves the same purpose as Oxygen in the real atmosphere, we find the concentration of the mock elements by the equation:

$$C(\lambda) = \frac{\varepsilon_{\text{Gr}}}{\varepsilon_\lambda} C_{\text{Gr}} - \frac{\log_{10}(I_{\text{rel}}(\lambda))}{l \varepsilon_\lambda} \quad (3.9)$$

where l will be twice the thickness of the atmosphere.

So, for the example case presented in Figure 14, the atmosphere will be primarily composed of Reddium, Blueogen, and Orangen, with less Greenium and Purpleum, and minimal Yellowine.

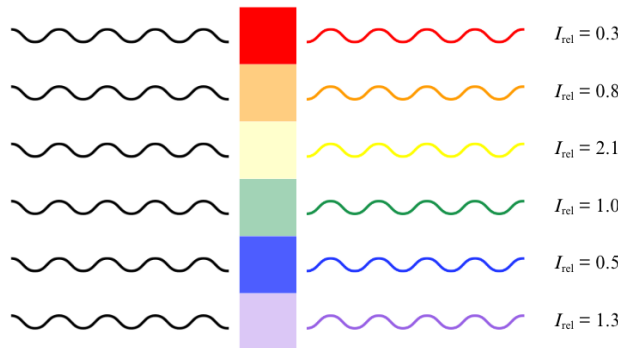


Figure 14: Mock model with variation in element absorption intensities.

3.4 Data Collection

The Payload is connected to the main OBC through a connector on the main PCB seen in Figure 15, which is then wired to the RP02W on the I2C bus at address 0x49.

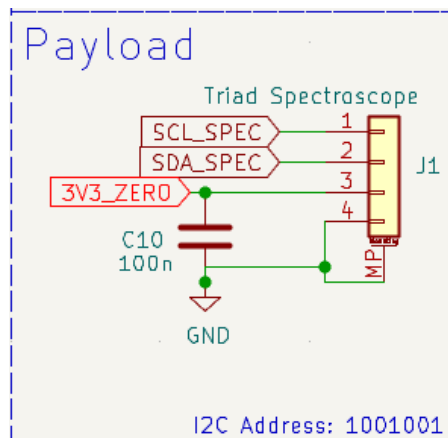


Figure 15: Schematic for the connector for the payload

From the RP02W, we can request data from all 18 channels on the sensor. Combining this with the time that we request it, we get the following payload data packet.

Table 11: Science Structure

Field	Type	Size (Bytes)
Calibrated value x 18	float	72
Timestamp	unsigned long integer	4
<i>Total</i>		76

This structure will be reference in the data down link section of the report which will give us an estimate of how much data we can afford to store over the period of the orbit, and in turn the granularity of our results.

4 Structural Subsystem

The structure of a CubeSat serves as the primary framework that houses and protects all subsystems during operation in space. It must be lightweight yet strong enough to withstand the mechanical stresses of launch, including vibrations, forces, and thermal fluctuations. A well designed structure ensures mechanical integrity, thermal management, and ease of integration, playing an important role in mission success.

4.1 Material Choices

The design of LUNATICS incorporates Aluminium 6061-T6 for the external structural framework and Carbon Fibre Nylon (CFN) for all internal mounts and secondary structural elements. These materials were selected based on a combination of mechanical performance, manufacturability, weight efficiency, and availability.

Table 12: Material Properties Comparison: Carbon Fibre Nylon (CFN) vs. Aluminium 6061-T6 [11] [12]

Property	CFN	Aluminium 6061-T6
Tensile Modulus (GPa)	2.4	68.9
Tensile Strength at Yield (MPa)	40	276
Tensile Strength at Break (MPa)	37	310
Tensile Strain at Break (%)	25	12
Flexural Strength (MPa)	71	276
Flexural Modulus (GPa)	3.0	68.9
Heat Deflection Temperature (°C)	145	170
Density (g/cm³)	1.2	2.7

Aluminium 6061-T6 provides high strength, good corrosion resistance, and excellent precision of manufacturing, making it well suited for the satellite's primary structure. The Aluminium components will be CNC machined by an external supplier (JLC CNC) to ensure precision and consistency. While manufacturing lead times of up to one week are expected for the CNC components, this is manageable within the project schedule.

Internal mounts will be fabricated from Carbon Fibre Nylon (CFN) using a Markforged additive manufacturing service. CFN was selected for its high stiffness, low mass, and suitability for producing complex geometries required within the internal structure. Additionally, additive manufacturing offers rapid production times, allowing for efficient turnaround during development.

A standard wall thickness of 2 millimetres has been selected for the aluminium chassis, informed by preliminary finite element analysis (FEA) results demonstrating sufficient strength under anticipated load conditions. This relatively thin profile maximises internal volume and reduces overall mass, offering a significant advantage over alternative materials such as 3D-printed polymers, which would require substantially thicker sections to achieve comparable structural performance.

4.2 Chassis Design

The structural components have been designed for in-house development, utilising CNC machining of aluminium parts. The structure consists of three unique parts, with two of each required for assembly. These parts include the two main side panels, which integrate the rail features and a flat face, a cross-panel which incorporate a flat face for internal bracing, and the two end caps. Each of these parts are unique in their design to accommodate the internal mounts that attach to them to hold the CubeSats components in place.



The parts have been deliberately designed for simplicity to minimise CNC manufacturing costs while maintaining the structural strength necessary for mission requirements. The design also prioritises ease of assembly: all internal components are mounted directly to the side panels, and final assembly involves securing the sides to the end caps using M3 countersunk screws, ensuring a flush finish on the outer surfaces.

Fillets have been applied throughout the design to minimise stress concentrations and improve the overall durability of the structure. The geometry of the components has also been optimised to reduce unnecessary material, contributing to weight savings without compromising strength. This was done using the preliminary FEA findings to remove excess material and reduce overall mass while maintaining structural integrity. The total estimated mass of the chassis is approximately 380 grams.

Additionally the rails are chamfered at 45° angle to one millimetre and will be anodised to prevent cold welding with the deployer to meet the CubeSat requirements.

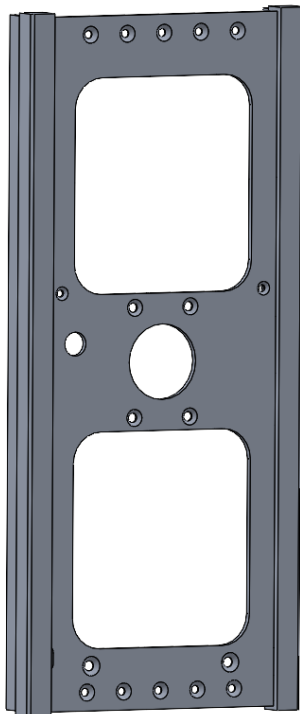


Figure 16: Main Panel with payload section (Panel 1).

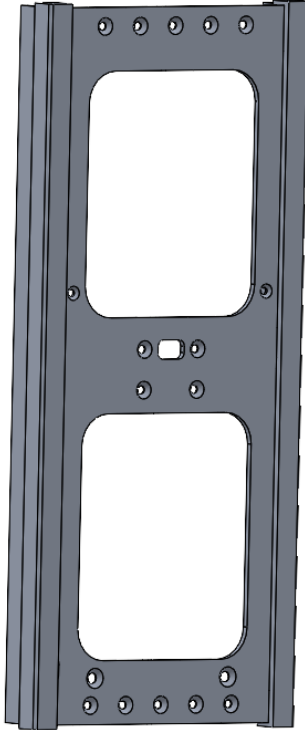


Figure 17: Main Panel without payload (Panel 2).

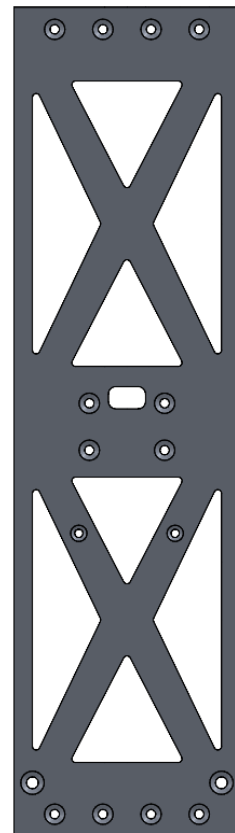


Figure 18: Cross side Panels.

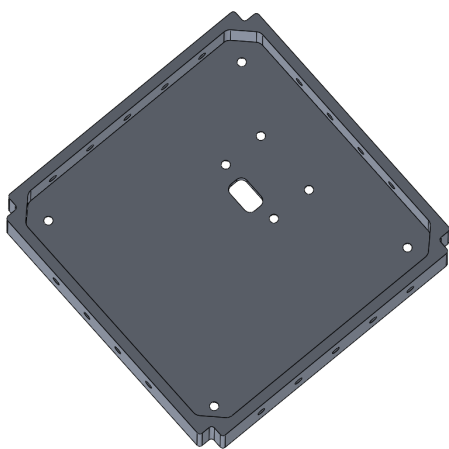


Figure 19: Top end cap.

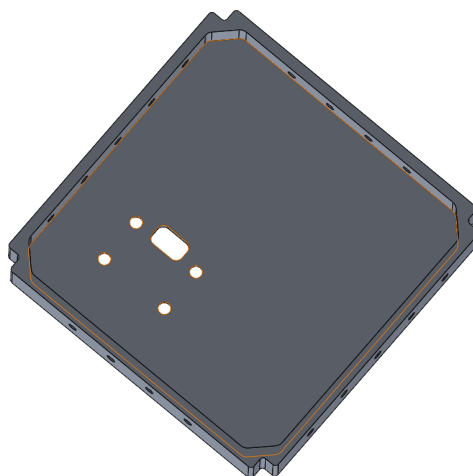


Figure 20: Bottom end cap.

4.2.1 Ease of Manufacture

To facilitate the manufacturing process, several design optimisations have been incorporated:

- All components feature turn radii greater than 1/8 inch, ensuring that no sharp 90-degree angles are present. This design decision aligns with best practices for CNC machining, which requires fillet radii to avoid tool stress and to ensure smoother cutting paths.
- The cross-side panels are designed with a uniform thickness of 2 millimetres, simplifying the machining process and ensuring consistency across all components.
- Only the rails extend beyond the main side panels, with all other features maintaining a 2-millimetre thickness and a 5-millimetre turn radius. This reduces the complexity of machining, as the simpler geometry allows for more efficient tool paths and reduces the potential for machining errors.
- The end caps are designed without any 90-degree turns; all turns are executed with radii exceeding 1/8 inch. This ensures manufacturability and minimises the risk of tool deflection during CNC processing.
- Additionally, the design has been structured to minimise the need for multiple machining setups. This allows for efficient batch production, streamlining both machining and assembly stages.
- Tolerances have been carefully specified to allow for easy fitment of components without the need for additional post-machining adjustments, further improving the efficiency of the manufacturing process.
- Symmetry has been incorporated in the design, enabling components to be flipped and duplicated with ease. This reduces setup time and associated manufacturing costs during CNC operations.
- The material choice, Aluminium 6061-T6, was selected to facilitate ease of machining, as it is widely known for its good machinability and predictable performance under CNC conditions.

These considerations collectively ensure that the manufacturing process is optimised for cost-efficiency, reliability, and rapid turnaround, while maintaining the required structural integrity and performance specifications.

4.2.2 Joints

The chassis is assembled using M3 structural steel screws, which secure the side panels to the end caps, ensuring a robust connection between the components. A total of 10 screws are used to fasten the main side panels, while the smaller cross panels are secured with 8 screws, bringing the total number of screws used for assembly to 36. This design ensures the structural integrity of the chassis, providing a reliable connection between all parts. Internal mounts are attached to the chassis using M3 bolts and nuts, also made from structural steel, ensuring a secure attachment of CubeSat components to the frame.

Blue threadlocker is applied to threaded fasteners to prevent loosening due to vibration while allowing for disassembly with standard tools.

The material properties of the M3 screws and bolts are below in Table 13:

Table 13: Material Properties of M3 Screws and M3 Bolts (Structural Steel) [13]

Property	M3 Screws and M3 Bolts (Structural Steel)
Tensile Strength (MPa)	600
Yield Strength (MPa)	500
Modulus of Elasticity (GPa)	200
Density (g/cm ³)	7.85
Shear Strength (MPa)	300
Ultimate Shear Strength (MPa)	350

The material used for the screws and bolts is high-strength structural steel, chosen for its mechanical properties and durability, ensuring the reliability of the chassis structure.

4.2.3 Ease of Assembly

The design has been optimised to streamline the assembly process, minimising the time and complexity involved in final construction. All internal components are mounted directly onto the side panels, allowing for efficient integration during assembly. The sides are then securely attached to the end caps using M3 countersunk screws, ensuring a flush finish on the outer surfaces. The use of standardised M3 bolts and screws across the entire structure ensures uniformity and ease of handling during assembly, reducing the likelihood of errors. Additionally, the symmetric design of the panels allows for simplified alignment, and the modular nature of the components facilitates rapid assembly with minimal tools.

4.3 Structural Design (Internal Components)

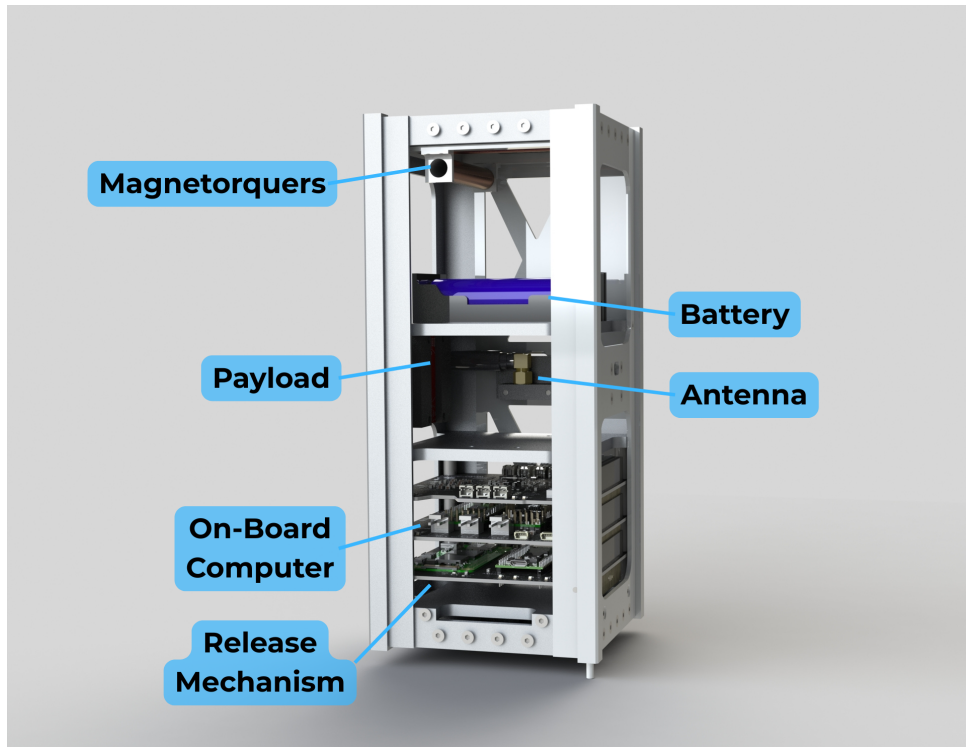
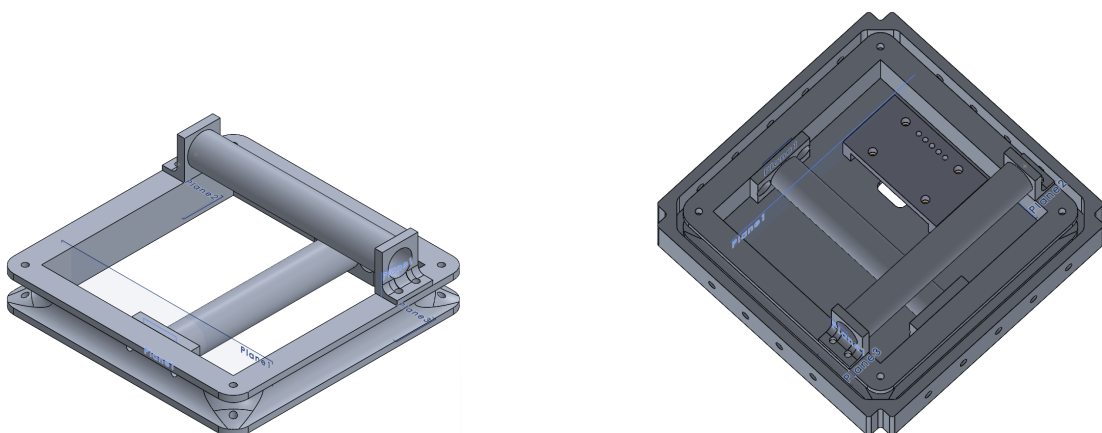


Figure 21: Internal Layout

4.3.1 ADCS Magnetorquer Assembly

The ADCS magnetorquer assembly is secured using M3 screws, which attach the components together. This assembly is composed of a mounting system made from Carbon Fibre Nylon (CFN). The CFN mounting system holds the copper coils in place along the three orthogonal axes: X, Y, and Z, which is critical for the system's function in controlling the satellite's orientation. The mount design uses two rod mount for the Y and Z axes and a square mount for the Z axis as depicted in 22a. By using this design the volume of the satellite occupied by the magnetorquer was minimised while still providing sufficient torque. The magnetorquer assembly is then fastened to the external structure of the CubeSat via the end plate using four M3 screws and bolts, ensuring a robust connection between the internal components and the external frame.



(a) Magnetorquers assembly.

(b) Location in main assembly.

Figure 22: ADCS assembly.

4.3.2 PCB Assembly

The PCBs are stacked on top of each other using steel stack separators, which ensure the proper alignment and spacing between each layer. Each PCB has an area of 80mm x 80mm, while the internal structure of the CubeSat provides a clearance of 5.5mm on each side, with an internal area of 91mm x 91mm. This gap facilitates the routing of wires between the PCB layers and ensures sufficient space for thermal management. The PCBs are surrounded by thermal mylar layers, which provide passive thermal control by protecting the wiring from temperature fluctuations. The bottom PCB is securely attached to a main plate, which is then fastened to the side panels of the CubeSat using M3 screws. This mounting system locks the PCBs in place, preventing movement during operation.

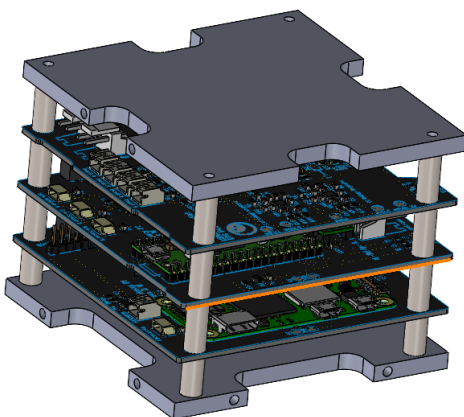


Figure 23: PCB assembly.

4.3.3 EPS Assembly

The solar panels, which are a key part of the EPS, are mounted on the outside of the CubeSat's chassis, positioned between the rails on each side panel. There are two solar panels on each side, each measuring 100mm by 80mm. To ensure the solar panels are securely attached and sit flush against the side panels, countersunk screws and bolts are used. These screws allow for a smooth surface, reducing aerodynamic drag. The solar panels are assembled as the last step, after the CubeSat structure is complete. They are affixed using COTS epoxy, ensuring a secure bond to the panels.

The batteries are attached to a plate above the sensors in the centre of the satellite. This plate is secured to the CubeSat using a main plate that is attached to the side panels with M2 screws. This configuration locks the battery components in place, ensuring a stable internal structure. The batteries themselves are housed in battery holders, which are mounted to the top plate using M3 bolts and nuts. This assembly ensures both the stability and accessibility of the battery system.

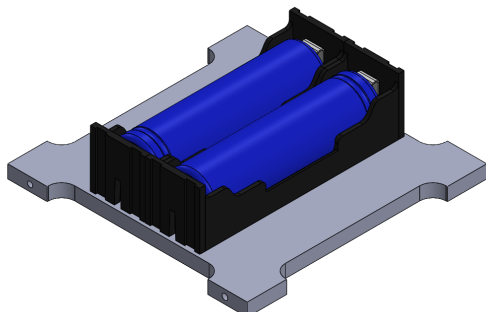


Figure 25: Battery assembly.

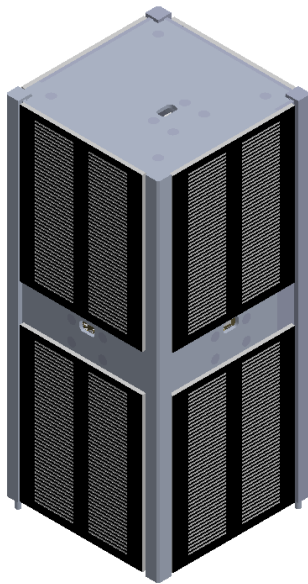
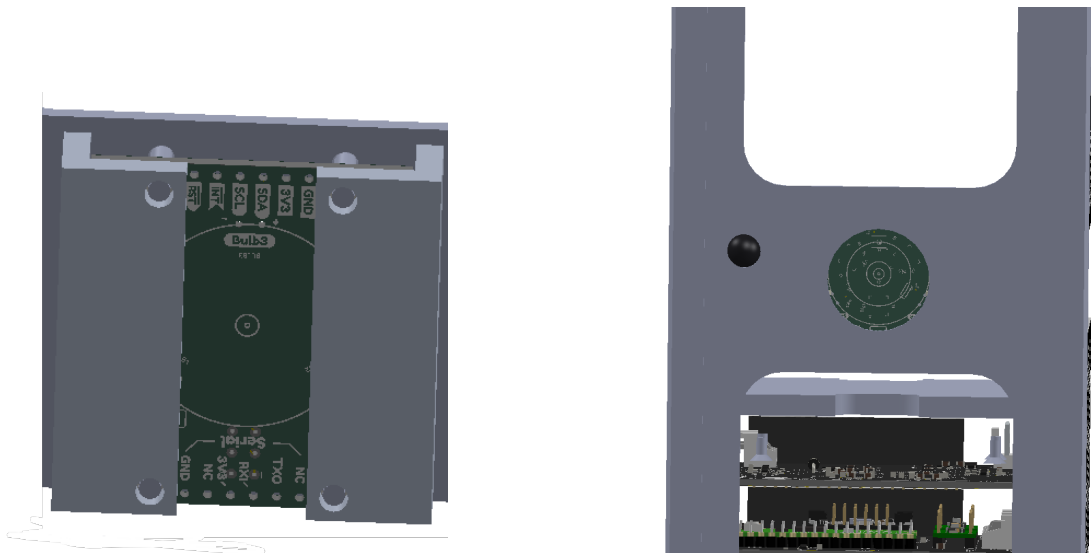


Figure 24: Solar panel assembly.

4.3.4 Payload Assembly

The payload sensor is positioned with a 24.4mm diameter hole in one of the main panels to allow its field of view out of the CubeSat. To enable the sensor to perform its mission, it must have a clear line of sight to Earth, necessitating constant adjustments in orientation. The sensor is placed at the center of the CubeSat to minimise torque on the ADCS magnetorquers, reducing the system's energy requirements. The payload sensor is securely mounted using four M3 nuts and bolts, and the mount is constructed from CFN, chosen for its ease of manufacture and assembly.



(a) Payload mounting.

(b) Assembly location allowing earth pointing view.

Figure 26: Payload assembly.

4.3.5 Sun Sensor Assembly

The sun sensors are placed on the other five faces of the CubeSat to the payload sensor. Each has a small hole to allow a clear field of view for attitude determination. These sensors provide crucial data to the ADCS system for accurate attitude control. The sun sensors use the same CFN material

for their mounts and are similarly attached using M3 bolts and nuts. This design ensures consistency and ease of manufacturing across the CubeSat's various components.

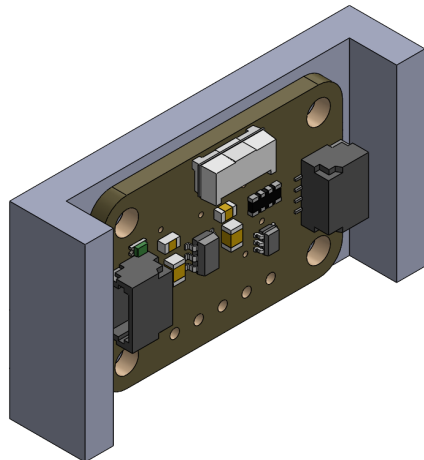


Figure 27: Sun sensor assembly.

4.3.6 Communications Assembly

The communications system includes an antenna that must also be Earth-pointing, aligning with the requirement to ensure proper communication with ground stations. This antenna is placed on the same side of the CubeSat as the payload sensor to maintain the Earth-facing orientation. A hole is incorporated into the CubeSat's structure to allow the antenna's field of view towards Earth. The antenna is mounted to the same top plate as the battery assembly, and its rotational movement is constrained by a hexagonal mount. The antenna is securely bolted to the top plate using M3 bolts, ensuring stability and precise alignment for communication purposes.

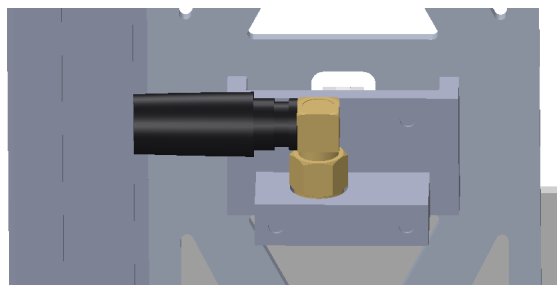


Figure 28: Antenna assembly

4.3.7 Deployment Switch Mechanism

The deployment switch is essential for detecting when the CubeSat has been released from the deployer and for initiating the deployment sequence. It is mounted directly to the CubeSat structure using threaded M3 fasteners. A non-conductive rod, which runs down one of the CubeSat's legs, actuates the switch upon release from the deployer, ensuring reliable operation with minimal parts.

The deployment switch triggers subsequent operations like system activation. Meanwhile, the Hold-Down and Release Mechanism (HDRM) is responsible for physically securing the antennas, only releasing them once the CubeSat is deployed and the switch signals it is safe to proceed.

4.3.8 Nichrome Release Mechanism

A nichrome burn wire system is employed in conjunction with nylon tie-down material to restrain the folded antennas prior to deployment. The nylon is wrapped around the antennas near the

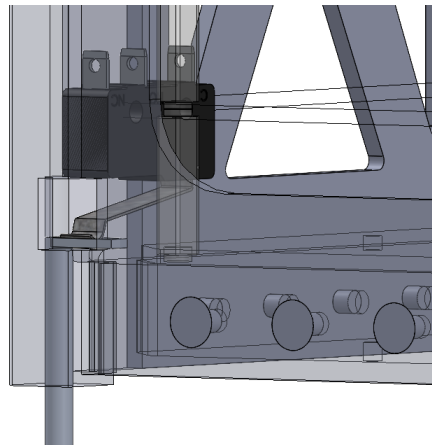


Figure 29: Deployment mechanism.

midsection of the CubeSat, rather than anchored to the structural feet. Anchoring to the feet was considered but ultimately rejected due to the excessive distance it would introduce between the antennas and the anchor points.

Such a configuration would make it difficult to maintain adequate tension in the tie-downs, increasing the risk of slack developing during launch vibrations and potentially compromising deployment reliability. By securing the nylon closer to the antennas, the design minimises tie-down length, ensures consistent tension, and enhances the effectiveness of the burn wire cutting process. This approach improves deployment reliability and reduces the likelihood of mechanical interference with other CubeSat subsystems.

4.3.9 Mass Budget

Below is the mass breakdown of a CubeSat's components across various subsystems. The total mass of all listed components is 2043.588 g, which is well within the target mass limit of 2660 g, leaving a remaining margin of 616.412 g. Major contributors include the structural subsystem, notably the CubeSat chassis at 815.568 g, and the electrical power system, particularly the solar panels and battery assemblies. Each subsystem is itemised with quantity, unit mass, and total mass to facilitate mass budgeting and ensure compliance with launch vehicle constraints. The more comprehensive spreadsheet can be found in Appendix G.

Table 14: CubeSat Component Mass Breakdown

Subsystem	Qty	Mass (g/unit)	Total (g)
Structural Subsystem			
CubeSat Chassis (includes screws)	1	815.568	815.568
Deployment Switch	2	4.84	9.68
Attitude Determination and Control Subsystem			
Magnetorquer Assembly (Y-axis)	1	65.428	65.428
Magnetorquer Wire	1	56.70	56.70
Microprocessor	3	36.00	108
VFMI-7700 lux Sensor	6	1.10	6.60
ArdPilot BN0055	1	2.75	2.75
Electrical Power System			
OBC	1	60.00	60.00
Battery Assembly	2	60.159	120.318
1W Solar Panel 80x100mm	8	36.30	290.40
Sony 18650 VTC6 Battery	2	50.60	101.20
Boost Converter	1	0.66	0.66
Buck Converter	1	0.44	0.44
Current Sensor	3	0.55	1.65
OBC & Handling Subsystem			
PCB	1	208.344	208.344
Communication Subsystem			
Antenna	1	33.00	33.00
Modem	1	26.95	26.95
Thermal Subsystem			
Mylar Layers	1	53.30	53.30
Kapton Tape	1	52.00	52.00
White Paint	1	24.00	24.00
Payload			
Spectroscopy Sensor AS726x	1	6.60	6.60
Total			2043.588
Target Mass			2660.00
Remaining Margin			616.412

4.3.10 Centre of Gravity

The CubeSat centre of gravity shall be located within a sphere of 20 mm diameter, centred on the CubeSat geometric centre. Centre of mass is currently at X = 49.61 mm, Y = 114.32 mm and Z = 49.73 mm.

The geometric centre is at X = 50 mm, Y = 100 mm and Z = 50 mm. The CubeSat's centre of gravity is currently located 14.33 mm from its geometric centre which is within the requirements.

The moments of inertia, expressed in grams*square millimetres, were calculated at the centre of mass and are aligned with the output coordinate system using positive tensor notation. The components are as follows in mm:

$$\mathbf{I} = \begin{bmatrix} 7143503.66 & -34487.02 & -4093.1 \\ -34487.02 & 2527096.23 & 9858.3 \\ -4093.1 & 9858.3 & 7104962.82 \end{bmatrix}$$

For the moments of inertia taken at the output coordinate system in mm:



$$\mathbf{I} = \begin{bmatrix} 24214987.18 & 6194450.23 & 2705793.23 \\ 6194450.23 & 7946886.75 & 6254810.49 \\ 2705793.23 & 6254810.49 & 24162529.67 \end{bmatrix}$$

The coordinate system is shown below.



Figure 30: Point of Origin and Coordinate System

4.4 Finite Element Analysis

To meet the structural requirements for CubeSat launch, the LUNATICS must satisfy all relevant qualification and acceptance testing criteria. To evaluate this, finite element analysis (FEA) will be performed using a preliminary, simplified CAD model of the satellite's structure. This model includes the primary structural components and will be analysed in ANSYS.

The analysis will cover key launch related load cases, including quasi-static acceleration, natural frequency response, sinusoidal vibration, random vibration, and shock loading. These simulations will help assess whether the current design is likely to meet launch requirements and identify areas for structural improvement. A mesh size of 0.002 m was used throughout the model. For each load case, only the maximum deformation and maximum stress results are presented here, although all results have been tabulated.

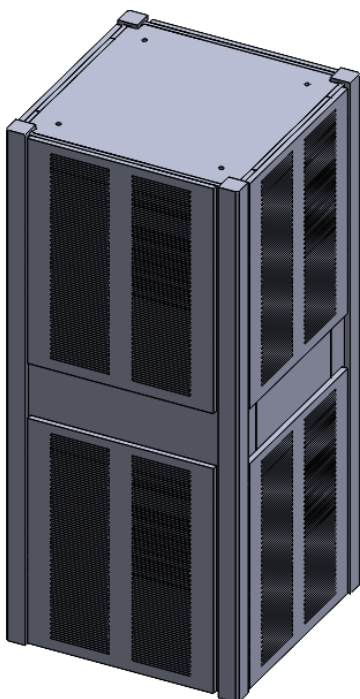
It is important to note that this FEA serves as a reference and cannot substitute for actual structural testing. Physical tests must be conducted prior to launch to verify the structural integrity and validate simulation results.

The simplified CAD model includes the primary structural components: the chassis, PCB stack, solar panels, magnetorquer mounts, and bolts. A simplified geometry was chosen to reduce computational time, enabling the use of a finer mesh to improve result accuracy. This trade off prioritises mesh quality over geometric complexity to better capture stress and deformation behaviour. The implemented CAD model is shown in Figure 31.

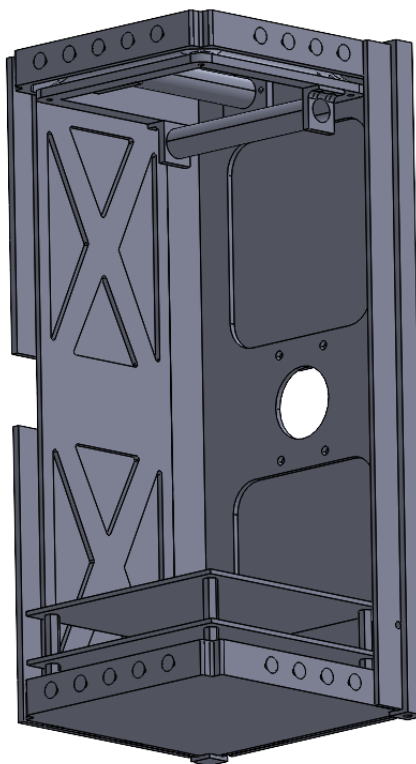
The boundary conditions for the FEA were defined to reflect the CubeSat's physical constraints during launch. Fixed supports were applied to the small protrusions at the top and bottom of the chassis, representing the points where the deployer mechanism would secure the satellite seen in

Table 15: Simplified CAD components for FEA and their materials

Component	Material
Chassis	Aluminium 6061-T6 wrought
PCB	PCB laminate, Glass-reinforced Epoxy FR-4
Solar panels	Resin Epoxy
Magnetorquer mounts	CF Nylon
Bolts and stack separators	Structural steel



(a) External view of simplified CAD model.



(b) Internal components in the simplified CAD model.

Figure 31: Simplified CAD model used in the FEA.

Figure 32. This assumption realistically simulates how loads are transferred into the structure during launch. Contact conditions across the model were categorised as either bounded or frictional. Frictional contacts were used at critical interfaces, specifically the bolts and PCB stack separators, where sliding or slippage may occur under vibration or shock. All other connections were modelled as bounded to reduce simulation complexity while maintaining structural fidelity. A coefficient of friction of 0.4 was chosen for all frictional surfaces, providing a conservative estimate based on the lower end of typical aluminium-on-steel contact values.

These boundary conditions were selected to strike a balance between model realism and computational efficiency. By accurately modelling the support conditions and key frictional interactions, the analysis reveals how load paths develop through the structure and where stress concentrations may occur under dynamic loading. This approach allows engineers to identify potential failure points, such as around bolt connections or interface regions, early in the design process, enabling targeted improvements to increase the structural resilience of the CubeSat prior to physical testing.

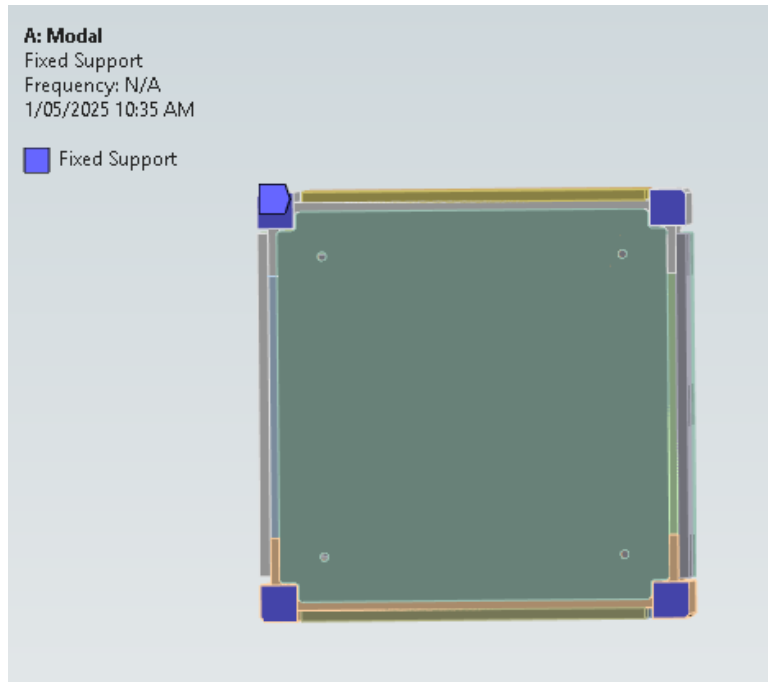


Figure 32: The location of the fixed support boundary conditions.

4.4.1 Quasi-static Acceleration

Quasi-static acceleration analysis is critical for assessing the CubeSat's structural integrity under the intense, steady accelerations experienced during launch, particularly from rocket thrust and gravity induced inertial forces. This analysis was conducted using ANSYS's Transient Structural solver to simulate a constant 13g acceleration applied independently along each of the principal axes (X, Y, and Z), as per S-2.1.1. The results, shown in Table 16, indicate the maximum stress and deformation values for each orientation. The highest stress occurred in the Y-axis loading at 10.7 MPa, while the largest deformation of 1.04×10^{-5} m was observed under Z-axis loading.

Figure 33 shows that the location of maximum stress was concentrated in the steel PCB stack separator. This could be attributed to localised mesh coarseness in this area, although the resulting stress remains far below the typical tensile strength of steel. The separator is modelled similarly to an M3 bolt with a tensile strength of 600Mpa (Table 13) and is thus expected to be structurally sound. As shown in Figure 34, the maximum deformation occurred in the solar panel. However, the deformation magnitude is minimal and unlikely to cause structural or functional issues.

Table 16: Quasi-static acceleration results

Load Case	Max Stress (MPa)	Max Deformation (m)
13g X axis	10.4	5.93e-6
13g Y axis	10.7	6.66e-6
13g Z axis	9.63	1.04e-5

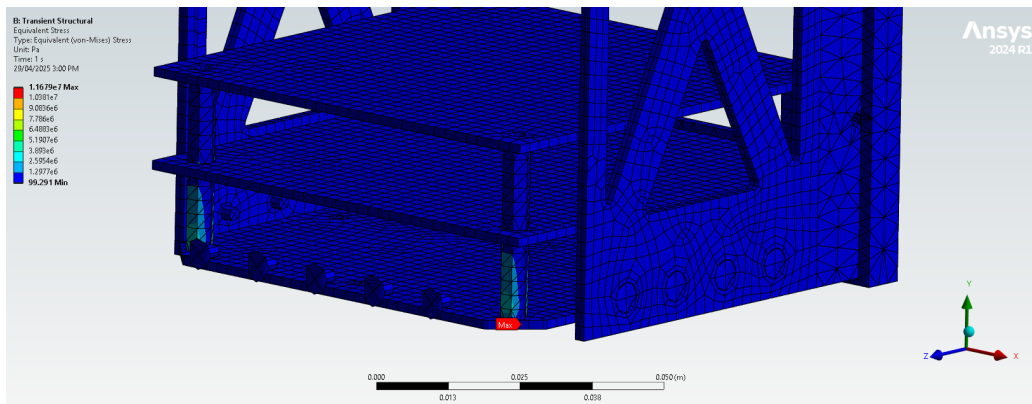


Figure 33: Location of maximum stress under quasi-static loads

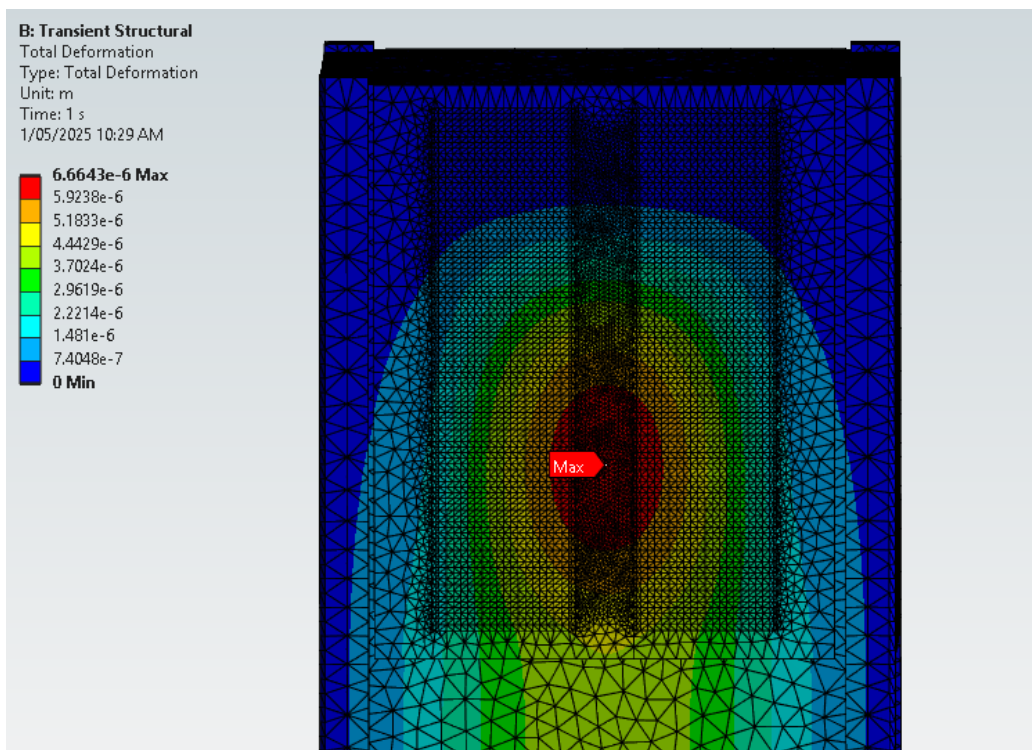


Figure 34: Location of maximum deformation under quasi-static loads

4.4.2 Natural Resonance Frequency

Modal analysis was performed in ANSYS to determine the CubeSat's natural frequencies, which are essential for ensuring the structure does not resonate with the vibrational frequencies encountered during launch. Resonance can amplify deformation and stress, leading to failure even at relatively low loads. Table 17 lists the first six natural frequencies, with the lowest mode at 683.05 Hz.

All modes are well above the 90 Hz threshold required for CubeSat compliance with launch standards S-2.2.2, indicating that the structure is stiff and unlikely to resonate with launcher-induced vibrations. Figure 35 illustrates the mode shape corresponding to the first natural frequency, where deformation is exaggerated for visualisation. These results confirm the structure's dynamic robustness.

Table 17: Modal Analysis

Mode	Frequency (Hz)
1	683.05
2	703.9
3	769.02
4	874.26
5	879.17
6	941.48

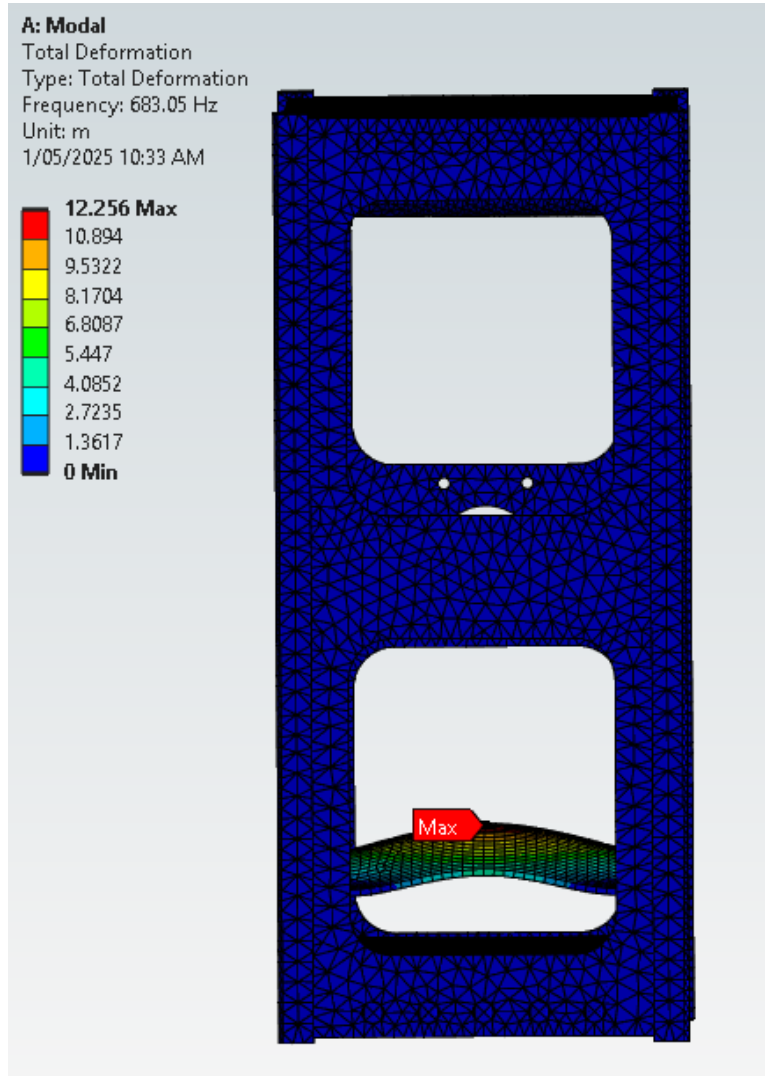


Figure 35: Maximum deformation under the 683.05 Hz load

4.4.3 Sinusoidal Vibration

Sinusoidal vibration testing simulates the periodic oscillations experienced during the rocket's ascent phase, particularly during stage separation and engine burns. In ANSYS, this was conducted using harmonic response analysis, coupled with prior modal analysis to capture how the structure responds over a frequency sweep. The loads were applied in the 5–120 Hz range across all three axes as specified in S-2.3.1.

As shown in Table 18, the maximum stress of 2.27 MPa occurred in the X-axis sweep from 5–100 Hz, while the greatest deformation was 2.14×10^{-6} m in the Z-axis. Figures 36 and 37 indicate that the



highest stress again occurred at the PCB stack separator and the greatest deformation occurred in the PCB itself. However, both values remain negligible in the context of the CubeSat's material limits and component tolerances, indicating excellent resistance to sinusoidal loads.

Table 18: Sinusoidal vibration results

Load Case	Max Stress (MPa)	Max Deformation (m)
X 5-100Hz at 2.5g	2.27	1.89e-6
X 100-120Hz at 1.25g	1.67	1.02e-6
Y 5-100Hz at 2.5g	2.22	1.68e-6
Y 100-120Hz at 1.25g	1.84	9.67e-7
Z 5-100Hz at 2.5g	1.77	2.14e-6
Z 100-120Hz at 1.25g	1.12	8.45e-7

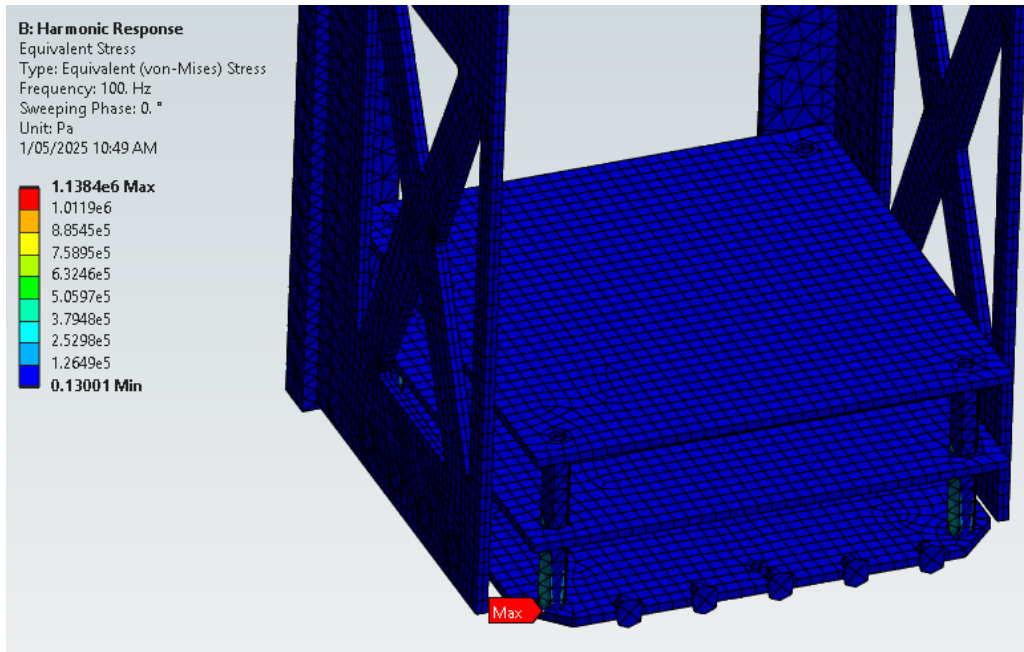


Figure 36: Location of maximum stress under sinusoidal vibration loads

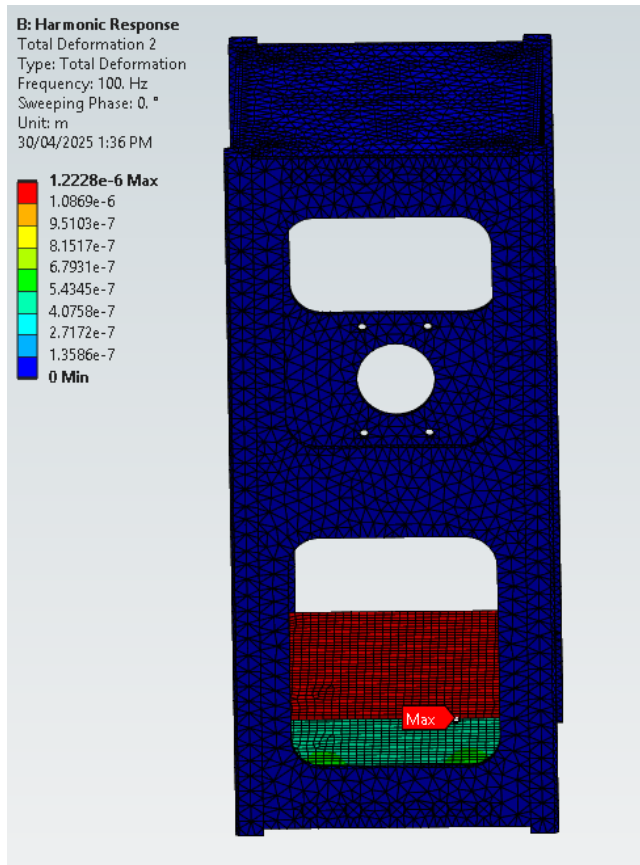


Figure 37: Location of maximum deformation under sinusoidal vibration loads

4.4.4 Random Vibration

Random vibration analysis is essential for simulating the broadband, stochastic vibrational environment of a rocket launch, especially due to turbulent aerodynamic flow and engine noise. ANSYS's random vibration module, based on modal superposition methods, was used to apply statistically representative loadings in each axis.

The results in Table 19 for the tests as per S-2.4.1 show that the highest stress of 61.1 MPa occurred in the Y-axis loading case, while the maximum deformation of 4.64×10^{-5} m was seen under Z-axis loading. As depicted in Figure 38 and 39, the stress again concentrates near the steel PCB stack separator, and the deformation is mostly localised to the PCB. Despite slightly higher values than in previous cases, the stresses are still well within material limits and pose no risk to structural integrity.

Table 19: Random vibration results

Load Case	Max Stress (MPa)	Max Deformation (m)
X axis	60.7	3.11e-5
Y axis	61.1	4.62e-5
Z axis	37.2	4.64e-5

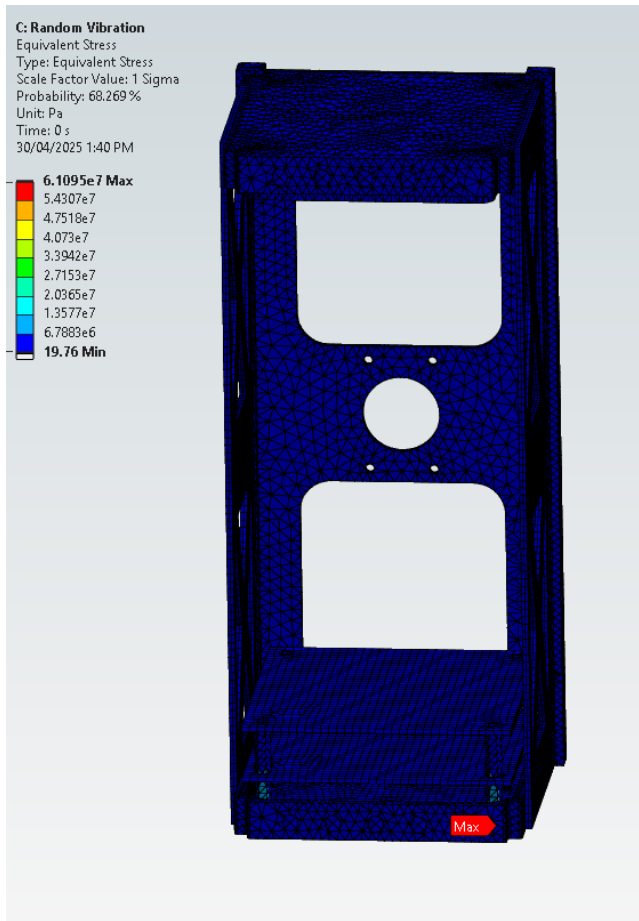


Figure 38: Location of maximum stress under random vibration loads

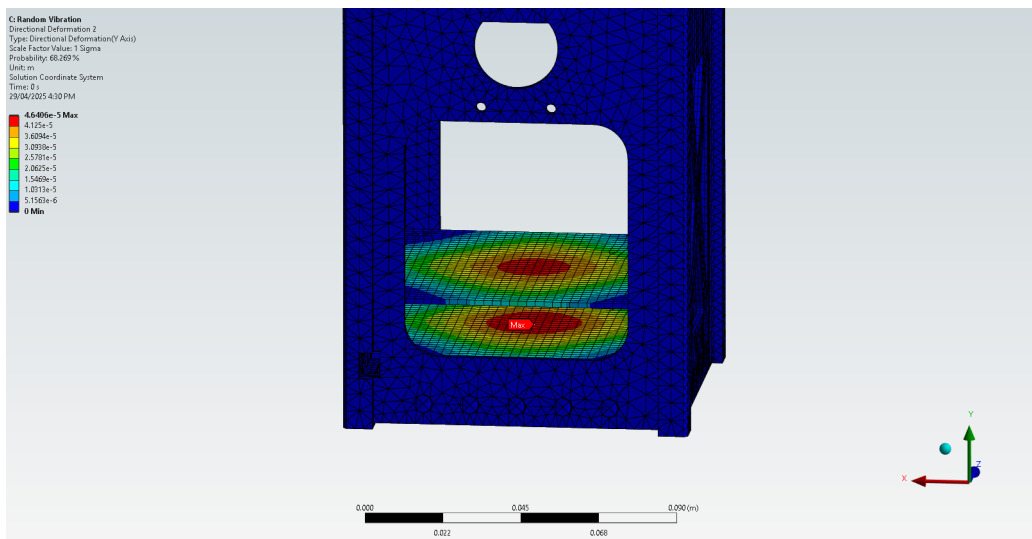


Figure 39: Location of maximum deformation under random vibration loads

4.4.5 Shock Loads

Shock load analysis captures the CubeSat's response to high-frequency, high-magnitude transient events such as stage separation or deployment mechanisms. ANSYS's response spectrum solver was used in conjunction with modal analysis to simulate these brief but intense dynamic loads.

As summarised in Table 20 for the loads specified in S-2.5.1, the most severe stress (180.1 MPa) occurred along the X-axis, while the largest deformation (1.79×10^{-3} m) was observed in the Z-axis. These values are higher than those seen in other loading scenarios, as expected for shock conditions. Figure 42 confirms that the maximum stress once again arises in the steel PCB stack separator, while Figure 41 shows that the greatest deformation occurs at the corner of the PCB. While a deformation of 1.7 mm is notable, it remains within acceptable limits and is not expected to damage internal components or interfere with functionality.

Table 20: Shock results

Load Case	Max Stress (MPa)	Max Deformation (m)
X axis	180.1	1.11e-3
Y axis	178.2	1.05e-3
Z axis	132.4	1.79e-3

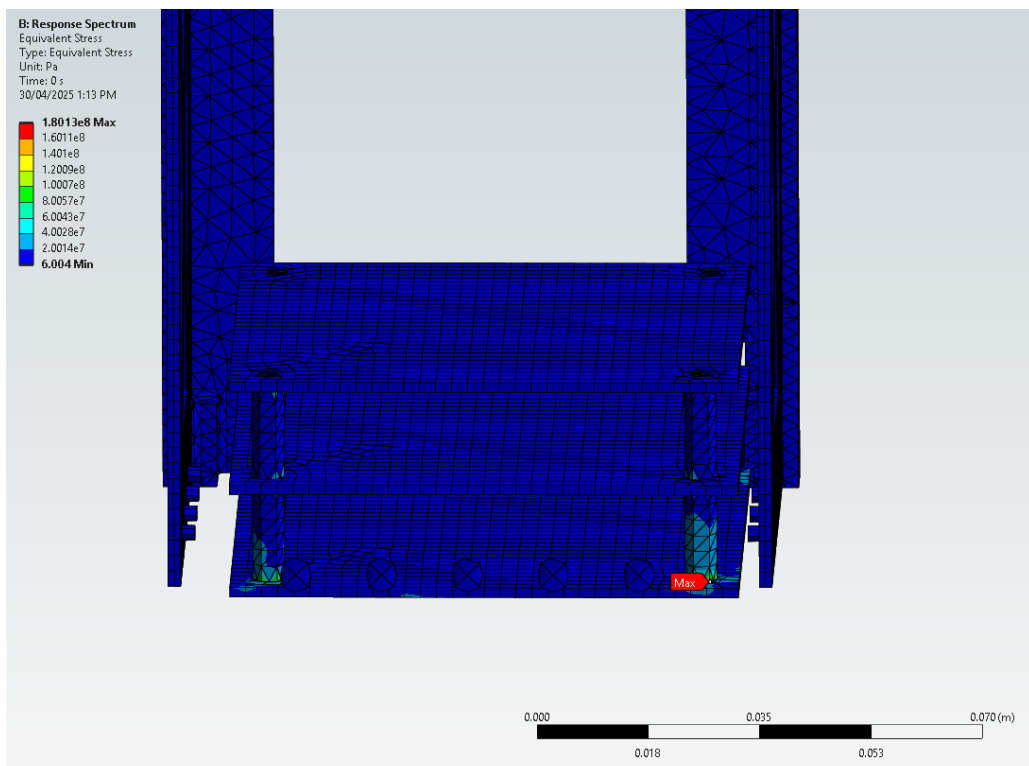


Figure 40: Location of maximum stress under shock loads

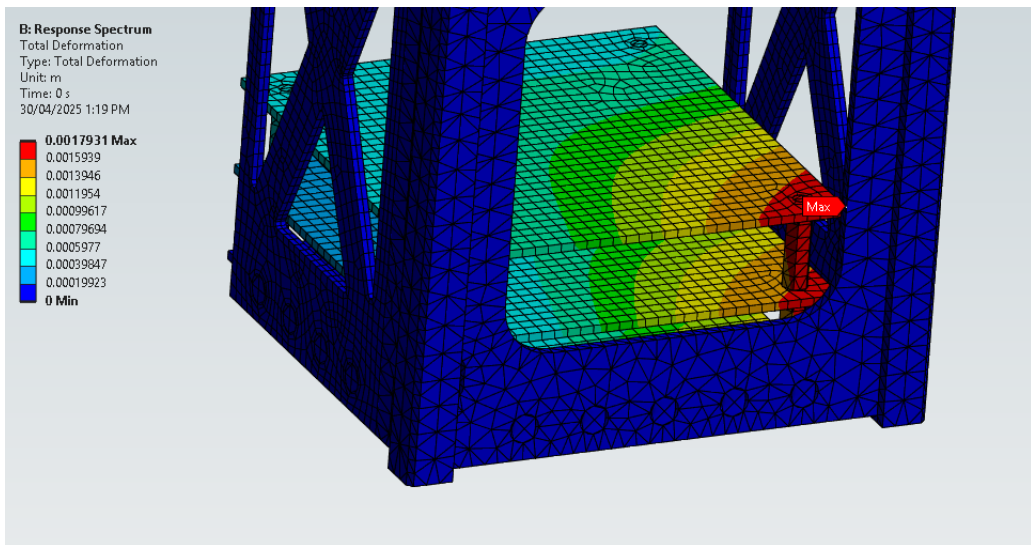


Figure 41: Location of maximum deformation under shock loads

4.4.6 Conclusion of Structural FEA Results

The structural finite element analysis of the LUNATIC CubeSat provides valuable insight into the performance of the preliminary design under a range of launch-induced loading scenarios. Across all simulated cases; including quasi-static acceleration, natural frequency analysis, sinusoidal vibration, random vibration, and shock loads the structure demonstrated compliance with the expected requirements for launch.

Critical regions, particularly around the steel PCB stack separators, consistently exhibited the highest stress concentrations. However, the stress values remained well below the material yield strength of steel, suggesting a robust structural design. The observed deformations, even under extreme conditions such as shock loading, were minor and unlikely to affect the performance or integrity of sensitive onboard components. This will be mitigated by being attached by bolts to a top plate and bottom plate as seen in the full structural design which weren't in the simplified CAD model.

It is important to note that while the current simulations were performed on a simplified CAD model to enable finer meshing and computational efficiency, the trends identified are reliable for design validation. These results support the structural feasibility of the Lunatic's design but must be complemented by physical testing on the final flight hardware to ensure full qualification for launch. Overall, the CubeSat simplified model passed the tests run by simulations, surviving the mechanical loads encountered during its deployment into orbit. This could be further improved by running these same simulations with the final design at a finer mesh size and by physically testing the model.

Table 21: FEA maximum stress and deformation results

Load Case	Max Stress (MPa)	Max Deformation (m)
Quasi-static acceleration	10.7	1.04e-5
Sinusoidal vibration	2.27	2.14e-6
Random vibration	61.1	4.64e-5
Shock loads	180.1	1.79e-3

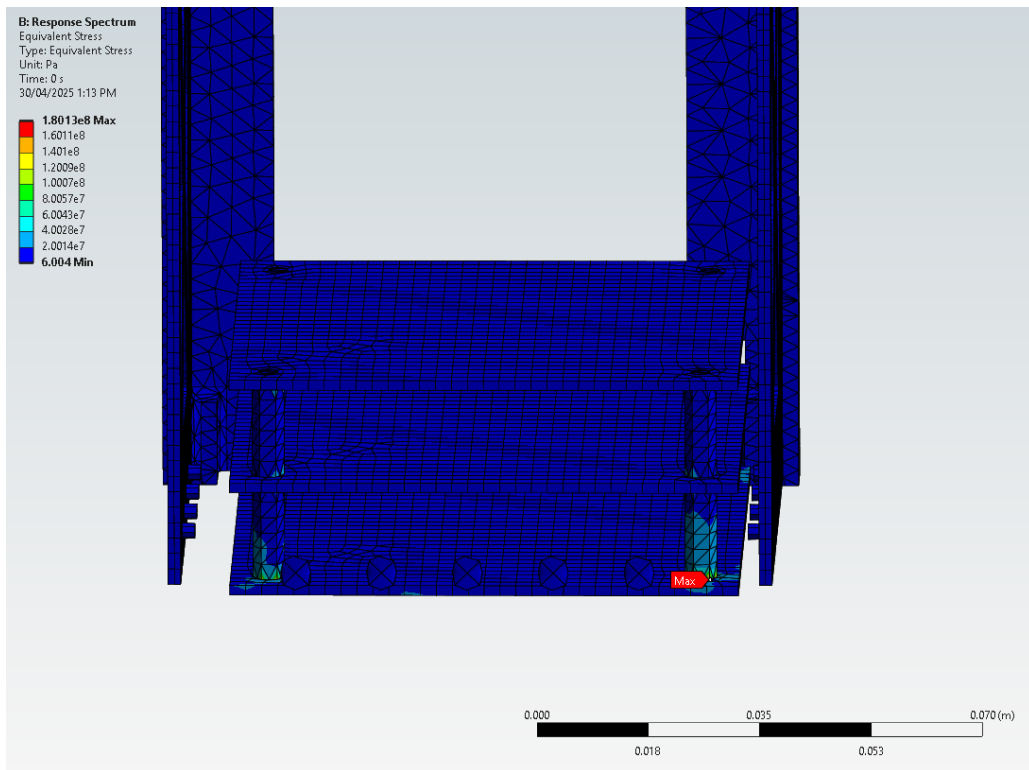


Figure 42: Location of maximum stress under shock loads

5 Attitude Determination and Control

5.1 Overview

The Attitude Determination and Control System (ADCS) is responsible for ensuring the CubeSat is pointing in the correct direction for the science payload and communication with Earth. The specific requirements for this subsystem are listed in Table 46 in the Appendix. Failure to meet these requirements will result in invalid science results and potentially the termination of the mission.

The ADCS is comprised of the Attitude Determination System (ADS) and the Attitude Control System (ACS). ADS is responsible for taking measurements to observe and estimate the attitude of the satellite. It consists of an IMU and 5 sun sensors to provide measurements, and a combination of a Quaternion Estimator (QUEST) and an Extended Kalman Filter (EKF) for attitude estimations.

5.1.1 Modes of Operation: ADCS

The ADCS will activate after the satellite has been deployed and has entered the Initialisation mode. During the Detumbling phase, the magnetorquers will use the Bdot algorithm to reduce the slew rate to an acceptable range. This only requires the readings from the Inertial Measurement Unit (IMU) to be on, thus reducing the power and computation required. Once the slew rate is within the acceptable range, the system will enter Nominal mode, where only the sensors will be active. If the attitude error exceeds the acceptable $\pm 5^\circ$ from S-AOC-02, then Nadir Pointing mode will be entered. Here a PID controller will be used to control the magnetorquers to correct any external disturbances or drift. In all the modes mentioned above, the sensors will be continuously taking measurements and feeding that into the determination algorithms, Quaternion Estimator (QUEST) and Extended Kalman Filter (EKF). In the event of low power or other emergency conditions, the CubeSat will enter Safe mode where all components of the ADCS will be shut down.

5.2 Attitude Determination System

The ADS sensors and algorithms have been tested and simulated to ensure each component functions as expected.

5.2.1 IMU

The BNO085 IMU is used for the CubeSat, it includes a 3 axis accelerometer, 3 axis gyroscope, 3 axis magnetometer and sensor fusion capabilities. The main purpose of the IMU will be providing raw data from the 3 sensors, which will be used in the ADS algorithms. Its secondary purpose is to act as a backup system in the event that the developed algorithms don't function as expected during testing. In this case the sensor fusion on the IMU will be used to provide attitude estimates.

The IMU was tested to ensure it could fulfill both its aims, the testing setup is shown in Figure 43. The provided Adafruit code examples were used to obtain the quaternions (Rotation Vector), Euler angles, the calibrated raw sensor measurements.

The IMU board was rotated 360° in the roll, pitch and yaw direction by hand. Figure 44 displays the corresponding Euler angles outputted by the IMU. It behaved as expected for the rotations in the roll and yaw direction, where the non rotated axes would remain relatively steady. However for the pitch direction, the non-rotating directions had large jumps in discontinuity. This occurred when the pitch angle neared $\pm 90^\circ$ and 0° . This is a consequence of gimbal lock, as pitch angle, θ , reaches its limits at $\pm 90^\circ$. The discontinuities around the $\theta = 0^\circ$ mark is a result of the angle wrapping between $\pm 180^\circ$ for the roll and yaw angles.



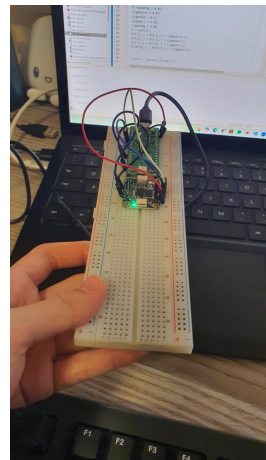


Figure 43: Testing Setup for the BNO085 IMU

The quaternions in Figure 45 don't reflect any of these discontinuities, which was expected. There are steep gradients which reflect the points of faster movement. Overall, the sensor fusion on the BNO085 has been demonstrated to function, however the accuracy of the IMU has not been measured. The smoothness of the quaternions was limited by the steadiness of the hands when physically rotating the IMU.

In order to obtain the quaternions in the correct format, quaternion sign flipping was required. This may be a result of a setting in the IMU.

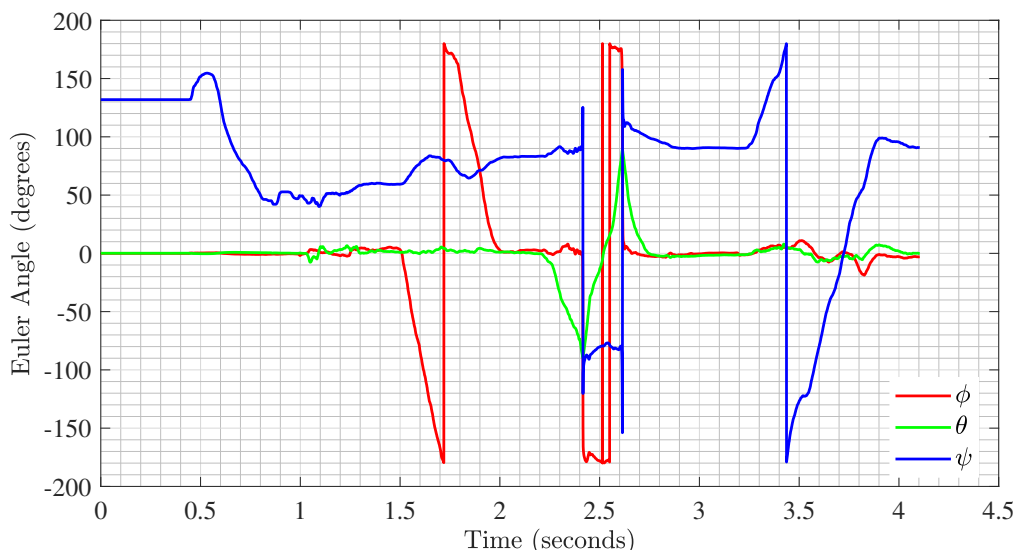


Figure 44: Euler Angles Obtained from BNO085 IMU Test

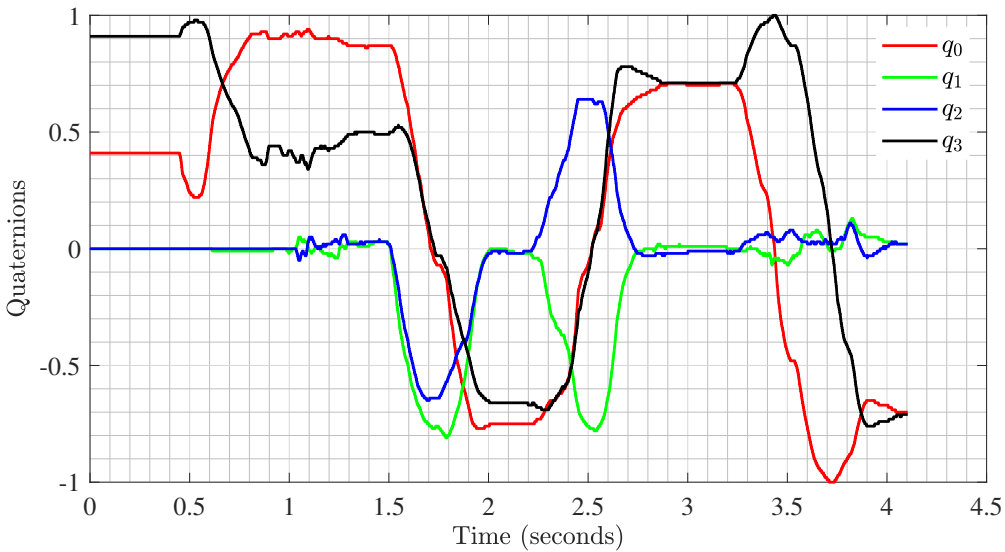


Figure 45: Quaternions Obtained from BNO085 IMU Test

The IMU's ability to output calibrated raw sensor measurements was tested by doing 360° rotations by hand. The calibrated accelerometer measurements include gravity and can be seen in Figure 46. The IMU outputted approximately $9.75m/s^2$ in the z axis, whilst the other axes were approximately $0m/s^2$, which was expected as no forces were applied. During the roll portion of the test, the z component produced a cosine-like behaviour where a minimum of $-9.97m/s^2$ was reached. The y component exhibited a sine-like behaviour where it reached approximately $\pm 9.81m/s^2$ when the z component was $0m/s^2$. During the entire roll manoeuvre, the x component remained at $0m/s^2$. This was expected as the x axis is the axis the rotation occurs around, since it does not change locations and hence acceleration. This verifies that the accelerometer vector always has a magnitude of $9.81m/s^2$, meaning the accelerometer works as expected. A similar pattern occurs for the pitch manoeuvre. For the yaw manoeuvre, all the components remain constant as the x any y axis always remains parallel to the floor and no height changes.

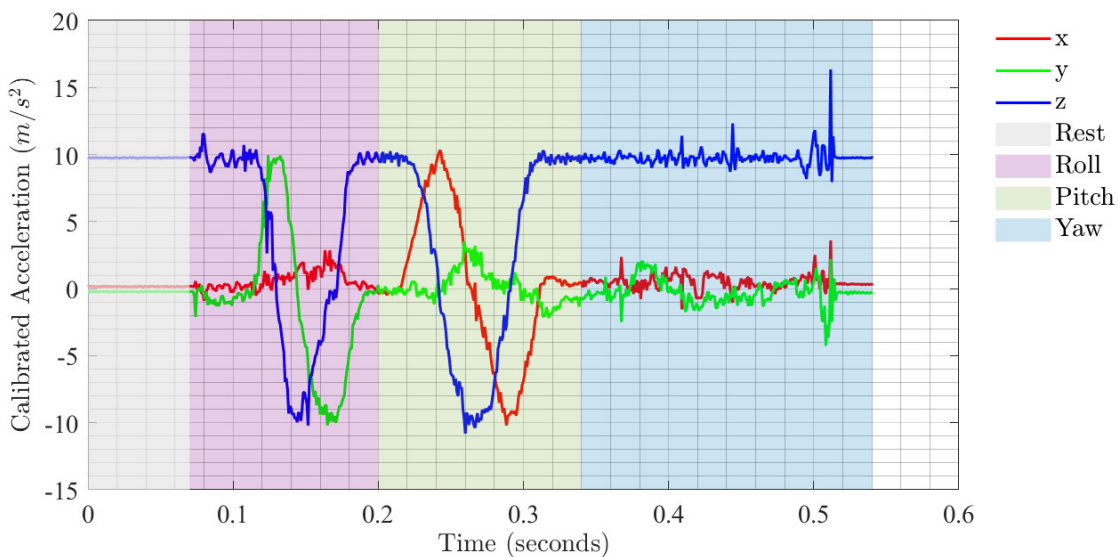


Figure 46: Calibrated Acceleration Obtained from BNO085 IMU Test

The gyroscope calibration removes the zero offset error, meaning when the IMU is at rest all axes should be equal to zero. This behaviour is shown in the Rest portion of Figure 47. The angular velocity only changes for the rotation axis, and the direction of the rotation is indicated by the signage of the angular velocity. For example, only the x axis moves during the roll manoeuvre.

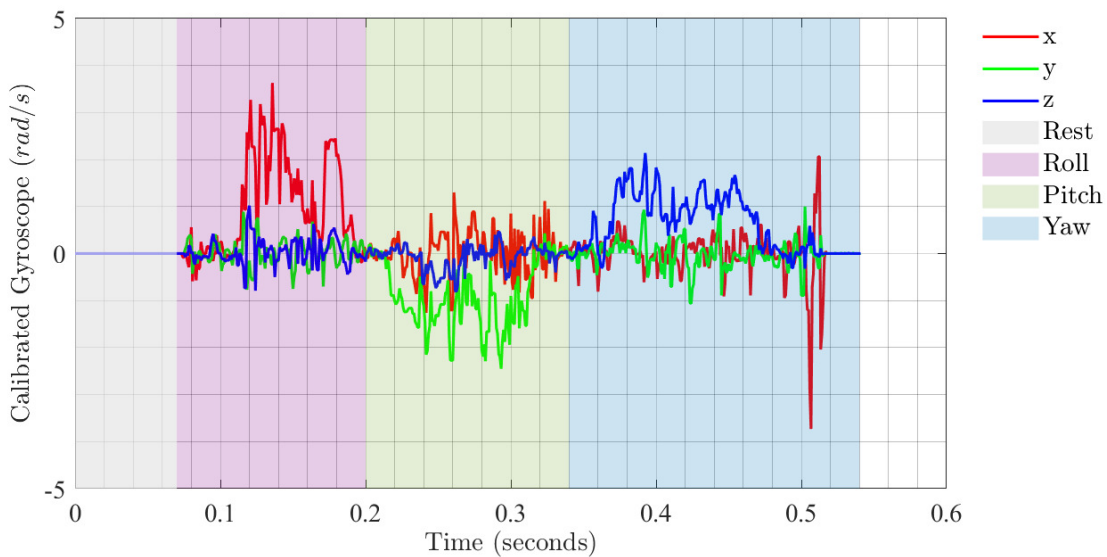


Figure 47: Calibrated Gyroscope Obtained from BNO085 IMU Test

The magnetometer calibration accounts for any external magnetic fields or ferromagnetic materials. In Figure 48, the axis being rotated about remains constant whilst the other two axes exhibit cosine and sine-like behaviour. Similar to the accelerometer, the magnetometer complies with the expectation that the magnitude of the magnetic field vector will equal the local magnetic field strength.

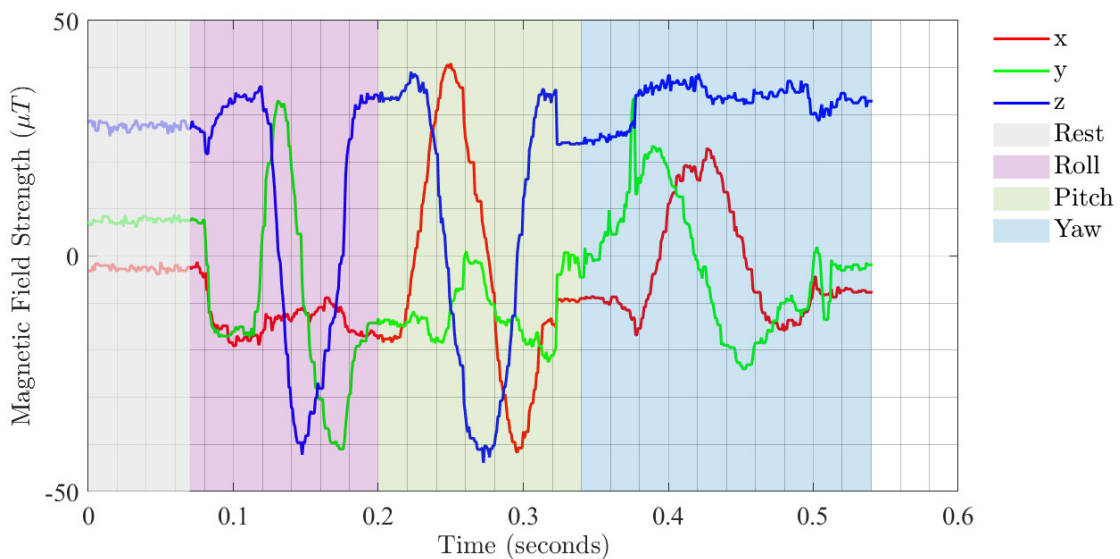


Figure 48: Magnetic Field Strength Obtained from BNO085 IMU Test

For all the data collected from the three sensors, there is evident noise from the hand held manoeuvres which was expected. However during this testing process, the sensor status provided by the IMU indicated that the sensors were calibrated to medium accuracy. This calibration error has



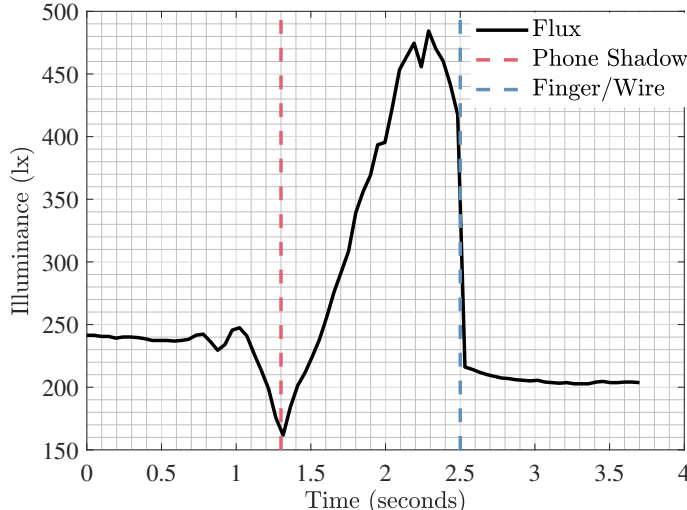
had a relatively larger impact on the gyroscope compared to the other two sensors. This likely exaggerated the gyroscopes susceptibility to drift and noise. Further improvements on the calibration will be needed.

5.2.2 Sun Sensor System

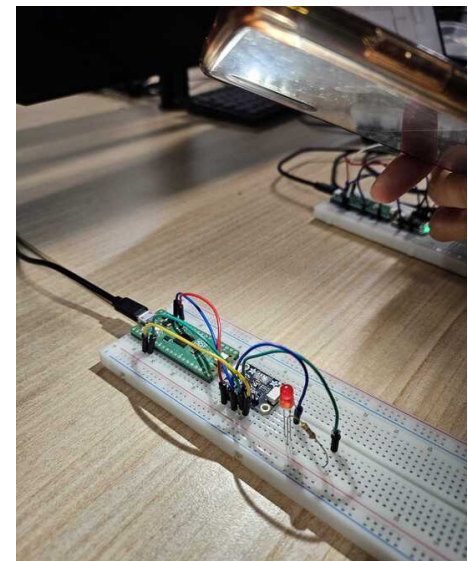
In order to get an absolute vector reading to combine with the IMU results, we will be using five sun sensors placed on each face of LUNATICS-0 (not including the face with the payload), which will each take readings of illuminance which we can use to calculate the direction of the sun.

LUNATICS-0 will be equipped with VEML7700 Ambient Light Sensors [5], provided by Adafruit, which will interface using I2C with the RPP2W.

Testing was performed on the VEML7700's with the configuration shown in Figure 49b and code examples provided by Adafruit. A phone torch was passed over the sensor, with the increase of light shown in Figure 49a. Both the red and blue vertical lines show where the illuminance dipped due to external factors - the shadow of the phone from external lights and when the wiring got in the way. These drops are likely what we will expect when the sensor is on a face looking away from the sun.



(a) Results from the sun sensor testing with a phone light passover



(b) Testing configuration for the VEML7700

Figure 49: VEML7700 Testing

The Sun Sensor system aboard the CubeSat will consist of five photodiode arrays that each sit on one face of the satellite. In the body coordinate frame of the CubeSat, denoted B , the sensors have the position vectors \mathbf{p} (in metres):

$$\mathbf{p}_1 = \begin{bmatrix} 0.05 \\ 0.05 \\ 0.2 \end{bmatrix} \quad \mathbf{p}_2 = \begin{bmatrix} 0.05 \\ 0.05 \\ 0 \end{bmatrix} \quad \mathbf{p}_3 = \begin{bmatrix} 0 \\ 0.05 \\ 0.1 \end{bmatrix} \quad \mathbf{p}_4 = \begin{bmatrix} 0.1 \\ 0.05 \\ 0.1 \end{bmatrix} \quad \mathbf{p}_5 = \begin{bmatrix} 0.05 \\ 0 \\ 0.1 \end{bmatrix}$$

Each sensor will each have a local reference frame, denoted S_i (for sensor i). The local sensor frame is related to the CubeSat body reference frame by the transformation matrix:

$$R_B^S = \begin{bmatrix} \cos \theta \cos \psi & -\cos \phi \sin \psi + \sin \phi \sin \theta \cos \psi & \sin \phi \sin \psi + \cos \phi \sin \theta \cos \psi \\ \cos \theta \sin \psi & \cos \phi \cos \psi + \sin \phi \sin \theta \sin \psi & -\sin \phi \cos \psi + \cos \phi \sin \theta \sin \psi \\ -\sin \theta & \sin \phi \cos \theta & \cos \phi \cos \theta \end{bmatrix} \quad (5.1)$$

where for each sun sensor:



Table 22: Rotation angles for each sun sensor.

Sensor	Rotation (deg)		
	ϕ	θ	ψ
1	0	0	0
2	180	0	0
3	0	-90	0
4	0	90	0
5	-90	0	0

The VEML7700 sensors will produce a measurement of relative intensity, S_{rel} , between the range $0 \leq S_{\text{rel}} \leq 1$ (Figure 50). This reading is related to the angular displacement φ of incident light on sensor i by the relation:

$$S_{\text{rel},i} = \cos \varphi_i = \hat{\mathbf{n}}_i \cdot \hat{\mathbf{u}}_{\text{sun}} \quad (5.2)$$

where φ is the angle between the sensor normal $\hat{\mathbf{n}}$ (i.e., the z -axis of the local sensor frame, in the CubeSat body frame), and the unit direction vector of the Sun $\hat{\mathbf{u}}_{\text{sun}}$ (also in body frame).

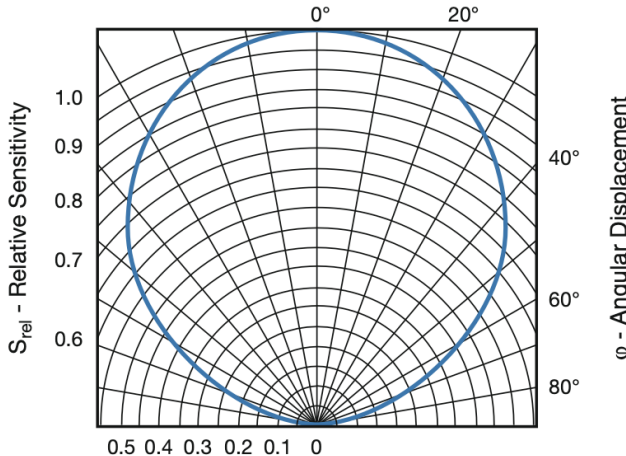


Figure 50: VEML7700 measured relative sensitivity vs. angular displacement [5].

The local sensor normal in the body frame is computed as:

$$\hat{\mathbf{n}}_i = R_{S,i}^B \begin{bmatrix} 0 \\ 0 \\ 1 \end{bmatrix} = (R_B^{S,i})^{-1} \begin{bmatrix} 0 \\ 0 \\ 1 \end{bmatrix} \quad (5.3)$$

To account for sensor noise and other imperfections affecting the sensor readings, weighted Non-linear Least Squares (NLLS) will be implemented for the Sun Sensor system to compute an approximation of the Sun's direction vector, $\hat{\mathbf{u}}_{\text{sun}}$ (assuming the Sun is a point-source of light); this will then be implemented later in to the attitude determination algorithm.

At a particular time, the three sensors with the highest S_{rel} values will be selected; this approach is preferred due to:

1. it simplifies the calculation and reduces the necessary computation power/time; and
2. geometrically, only a maximum of three CubeSat faces should be physically able to see the Sun at a time. This cancels out the noise in the other *shadow-facing* sensors.

For the remainder of the NLLS algorithm explanation, the three selected sensors will be referred to by subscripts $[A, B, C] \in i$.

The NLLS process will minimise the weighted square of the residual:

$$r_i = S_{\text{rel},i} - \hat{\mathbf{n}}_i \cdot \hat{\mathbf{u}}_{\text{sun}} = \cos \varphi_i - \cos \hat{\varphi}_i \quad (5.4)$$

i.e., the difference between the actual measured angle φ_i by sensor i , and the angle between the estimated Sun direction vector $\hat{\mathbf{u}}_{\text{sun}}$ and the normal of the sensor $\hat{\mathbf{n}}_i$, $\hat{\varphi}_i$.

In vector form, letting $\hat{\mathbf{u}}_{\text{sun}} = \hat{X}$, this becomes:

$$R = Y - H\hat{X} \quad (5.5)$$

for residual vector R (3×1), where the observation vector Y is given by Equation 5.6, and the design matrix H is given by Equation 5.7.

$$Y = \begin{bmatrix} S_{\text{rel},A} \\ S_{\text{rel},B} \\ S_{\text{rel},C} \end{bmatrix} = \begin{bmatrix} \cos \varphi_A \\ \cos \varphi_B \\ \cos \varphi_C \end{bmatrix} \quad (5.6)$$

$$H = \begin{bmatrix} \hat{\mathbf{n}}_A^T \\ \hat{\mathbf{n}}_B^T \\ \hat{\mathbf{n}}_C^T \end{bmatrix} = \begin{bmatrix} n_{x,A} & n_{y,A} & n_{z,A} \\ n_{x,B} & n_{y,B} & n_{z,B} \\ n_{x,C} & n_{y,C} & n_{z,C} \end{bmatrix} \quad (5.7)$$

The design matrix H represents the relationship between the observed measurements, Y , which are the S_{rel} values from each sensor, and the unknown direction vector $\hat{X} = \hat{\mathbf{u}}_{\text{sun}}$, determined from the residual calculation in Equation 5.4.

The weight matrix W of the system is defined based on the value of S_{rel} , such that the diagonal entries w_i in W are given as:

$$w_i = S_{\text{rel},i}^2 \quad (5.8)$$

$$W = \begin{bmatrix} w_A & 0 & 0 \\ 0 & w_B & 0 \\ 0 & 0 & w_C \end{bmatrix} = \begin{bmatrix} S_{\text{rel},A}^2 & 0 & 0 \\ 0 & S_{\text{rel},B}^2 & 0 \\ 0 & 0 & S_{\text{rel},C}^2 \end{bmatrix} \quad (5.9)$$

where W is normalised by dividing by its trace, $W \rightarrow W/\text{tr}(W)$. with larger S_{rel} values were to be prioritised due to the higher angular resolution at small φ (see Figure 50), and hence, the minimal impact of noise on S_{rel} on smaller φ .

To find the optimal estimated Sun direction vector, the NLLS minimises the objective function:

$$J(\hat{X}) = R^T W R = (Y - H\hat{X})^T W (Y - H\hat{X}) \quad (5.10)$$

The gradient of the objective function with respect to \hat{X} , $\nabla_{\hat{X}} J(\hat{X})$, gives the direction in which to adjust the current estimate of the Sun direction vector:

$$\nabla_{\hat{X}} J(\hat{X}) = -2H^T W R = -2H^T W (Y - H\hat{X}) \quad (5.11)$$

which defines the non-linear nature of the estimation system.

The Sun direction vector $\hat{X} = \hat{\mathbf{u}}_{\text{sun}}$ is then updated iteratively using gradient descent, where the update rule is:

$$\hat{X}^{(k+1)} = \hat{X}^{(k)} - \alpha \nabla_{\hat{X}} J(\hat{X}) \quad (5.12)$$

where α is the “learning rate” or *step size*. After each update, \hat{X} is normalised to ensure the correct residual calculation (Equation 5.4) which requires unit vectors such that $\|\hat{X}\| = \|\hat{\mathbf{u}}_{\text{sun}}\| = 1$.

Hence, we are able to determine the direction vector of the Sun in the body frame $\hat{X} = \hat{\mathbf{u}}_{\text{sun}}$ that best satisfies the measured direction to the Sun by the individual sensors. This estimation is then fed into the attitude determination algorithm, forming a part of the satellite’s ADC system.



To test the robustness of the Sun Sensor NLLS algorithm, the expected readings on each sensor based on the “true” Sun direction vector were determined using geometry. These readings were then fed into the NLLS algorithm, and the resulting estimated sun direction vector calculated. The NLLS was performed for a tolerance of $\epsilon = 10^{-6}$, maximum iteration number of 1000. Noise on the sensor S_{rel} readings was simulated for a Gaussian distribution about 0 for magnitude 0.001. These validation results can be seen in Table 23.

Table 23: Validation of NLLS Sun direction estimation with clean and noisy readings.

True Sun direction vector $\hat{\mathbf{u}}_{\text{sun}}$ Integer form	Unit	Estimated Sun direction vector $\hat{\mathbf{X}}$	
		Clean	Noisy
[1, 1, 1]	[0.57735, 0.57735, 0.57735]	[0.57736, 0.57735, 0.57735]	[0.57726, 0.57795, 0.57684]
[2, 1, 1]	[0.81650, 0.40825, 0.40825]	[0.81650, 0.40824, 0.40824]	[0.81640, 0.40691, 0.40978]
[2, 1, -1]	[0.81650, 0.40825, -0.40825]	[0.81650, 0.40824, -0.40824]	[0.81606, 0.40887, -0.40850]
[-2, 3, 1]	[-0.53452, 0.80178, 0.26726]	[-0.53453, 0.80179, 0.26724]	[-0.53425, 0.80210, 0.26687]

As seen above, the Sun Sensor system is able to accurately estimate the direction vector of the Sun to within an accuracy of order 10^{-3} . When combined with other attitude determination processes, it will serve to effectively orient the CubeSat.

5.2.3 Attitude Determination Algorithm

The attitude determination software will consist of a Quaternion Estimator (QUEST) and a Extended Kalman Filter (EKF). They will be used in combination, as the EKF operates best when the initial quaternion is as accurate as possible. QUEST is able to provide a static attitude estimation.

5.2.4 Quaternion Estimator

QUEST provides a static estimation of the attitude which will be feed into the EKF, since EKF functions best when the initial quaternion is as accurate as possible. This combination improves the convergence time and robustness. The QUEST algorithm involves solving Wahba’s problem where the loss function is minimised (Equation (5.13)). W is the observer vector and V is the reference vector where they must not be parallel. n is the number of observer vectors and a is the weighting of each observer vector.

$$L(\mathbf{A}) = \frac{1}{2} \sum_{i=1}^n a_i |\hat{\mathbf{b}}_i - \mathbf{A}\hat{\mathbf{r}}_i|^2 \quad (5.13)$$

When the loss function is at a minimum the gain function will be at a maximum. This is defined in Equation (5.14).

$$g(\mathbf{A}) = \text{tr}(\mathbf{AB}^T) \quad (5.14)$$

Here B , the attitude profile matrix is:

$$\mathbf{B} = \sum_{i=1}^n a_i \hat{\mathbf{W}}_i \hat{\mathbf{V}}_i^T \quad (5.15)$$

In this application, only one observer vector was used ($n = 1$) this being the accelerometer measurements, and the magnetometer acted as the reference vector. Following the notation in [15], the quaternions are represented by:



$$\bar{q} = \begin{bmatrix} \cos \frac{\theta}{2} & \hat{\mathbf{X}} \sin \frac{\theta}{2} \end{bmatrix} = [q \quad \mathbf{Q}] \quad (5.16)$$

This means the gain function can also be expressed as:

$$g(\bar{q}) = \bar{q}^T \mathbf{K} \bar{q} \quad (5.17)$$

\mathbf{K} is defined below. Note, all additional variables used are defined in Appendix B.2.

$$\mathbf{K} = \begin{bmatrix} \mathbf{S} - \sigma \mathbf{I}_{3 \times 3} & \mathbf{Z} \\ \mathbf{Z}^T & \sigma \end{bmatrix} \quad (5.18)$$

The gain is optimised if eigenvalue of \mathbf{K} is the maximum.

$$K\bar{q}_{opt} = \lambda_{max}\bar{q}_{opt} \quad (5.19)$$

Hence to obtain the eigenvalue, the Newton Raphson's method is used with the characteristic equation (Equation (5.20)) and its derivative (Equation (5.21)).

$$f(\lambda) = \lambda^4 - (a + b)\lambda^2 - c\lambda + (ab + c\sigma - d) = 0 \quad (5.20)$$

$$f'(\lambda) = 4\lambda^3 - 2(a + b)\lambda - c \quad (5.21)$$

$$\lambda_{t+1} = \lambda - \frac{f(\lambda)}{f'(\lambda)} \quad (5.22)$$

From this calculated eigenvalue the optimised quaternion can be described by:

$$\bar{\mathbf{q}}_{opt} = \frac{1}{\sqrt{\gamma^2 + |\mathbf{X}|^2}} \begin{bmatrix} \mathbf{X} \\ \gamma \end{bmatrix} \quad (5.23)$$

$$\mathbf{X} = (\alpha \mathbf{I}_{3 \times 3} + \beta \mathbf{S} + \mathbf{S}^2) \mathbf{Z}^2 \quad (5.24)$$

$$\gamma = (\lambda + \sigma)\alpha - \Delta \quad (5.25)$$

This algorithm was implemented with the accelerometer and magnetometer measurements as observer and reference vectors. To ensure the QUEST algorithm was functioning correctly, tester values indicated below were used.

$$\mathbf{b} = \begin{bmatrix} 0 & 1 \\ 0 & 0 \\ 1 & 0 \end{bmatrix} \quad (5.26) \qquad \mathbf{r} = \begin{bmatrix} -1 & 0 \\ 0 & 0 \\ 0 & 1 \end{bmatrix} \quad (5.27)$$

These unit vectors represent a -90° rotation about the Y axis. Consequently by converting direction cosine matrix of this rotation, the expected quaternions was $[0.7071 \ 0 \ -0.7071 \ 0]$. This was matched by the QUEST algorithm. To further test the robustness of the algorithm, white Gaussian noise with the order of magnitude of 10^{-1} was added to the reference vectors. This produced



$[0.6973 \ -0.0394 \ -0.7156 \ -0.0145]$. To observe the accuracy of the quaternions, the expected value was multiplied by the transpose of the estimated. For a perfect match, the result would be 1 following the unit magnitude property of quaternions. The value for this scenario was 0.9975, which is well within what is necessary for the EKF.

5.2.5 Extended Kalman Filter

The EKF is used to continually track and update the attitude of the CubeSat in quaternions. This method accounts for any noise the sensors may have and avoids gimbal lock prone in Euler angle representations.

Algorithm Logic [16]

The model is defined by the following, where \mathbf{x}_k is the state vector, \mathbf{f} is the dynamic model describing the state vector and \mathbf{w} is the noise in the model. Whilst \mathbf{z}_k is the measurement vector containing the measured values from sensors and \mathbf{h} is the observation model that has the corresponding true known reference vectors converted into the body frame. Since the orbit of the CubeSat is predetermined, the true value of these reference vectors can be calculated. \mathbf{v} is the measurement noise.

$$\mathbf{x}_k = \mathbf{f}(\mathbf{x}_{k-1}) + \mathbf{w}_{k-1} \quad (5.28)$$

$$\mathbf{z}_k = \mathbf{h}(\mathbf{x}_k) + \mathbf{v}_k \quad (5.29)$$

\mathbf{f} consists of the derivatives of the state vector.

$$\mathbf{f} = \begin{bmatrix} \dot{\mathbf{q}} \\ \dot{\boldsymbol{\omega}} \end{bmatrix} \quad (5.30)$$

$$\dot{\mathbf{q}} = \frac{1}{2} \boldsymbol{\Xi} \boldsymbol{\omega} = \frac{1}{2} \begin{bmatrix} -q_1 & -q_2 & -q_3 \\ q_0 & -q_3 & q_2 \\ q_3 & q_0 & -q_1 \\ -q_2 & q_1 & q_0 \end{bmatrix} \begin{bmatrix} \omega_x \\ \omega_y \\ \omega_z \end{bmatrix} \quad (5.31)$$

$$\dot{\boldsymbol{\omega}} = \mathbf{J}^{-1}(\boldsymbol{\tau} - \boldsymbol{\omega} \times (\mathbf{J}\boldsymbol{\omega})) \quad (5.32)$$

Here \mathbf{J} is the inertia matrix of the satellite. The EKF process begins with predicting the current state vector and covariance matrix ($\hat{\mathbf{P}}_k$) using the previous values. This is calculated through Equations (5.33) and (5.34).

$$\hat{\mathbf{x}}_k = \mathbf{f}(\hat{\mathbf{x}}_{k-1})\Delta t + \mathbf{w}_k + \hat{\mathbf{x}}_{k-1} \quad (5.33)$$

$$\hat{\mathbf{P}}_k = \mathbf{F}_{k-1} \mathbf{P}_{k-1} \mathbf{F}_{k-1}^T + \mathbf{Q} \quad (5.34)$$

Here \mathbf{F} is the Jacobian of \mathbf{f} and \mathbf{Q} is the model error matrix.

$$\mathbf{F} = \frac{\partial \mathbf{f}(\mathbf{x})}{\partial \mathbf{x}} = \begin{bmatrix} \frac{1}{2} \boldsymbol{\Omega} & \frac{1}{2} \boldsymbol{\Xi} \boldsymbol{\omega} \\ \mathbf{0}_{3 \times 4} & \boldsymbol{\Pi} \end{bmatrix} \quad (5.35)$$

$$\boldsymbol{\Pi} = \frac{\partial \dot{\boldsymbol{\omega}}}{\partial \boldsymbol{\omega}} = \begin{bmatrix} 0 & \frac{J_y - J_z}{J_x} \omega_z & \frac{J_y - J_z}{J_x} \omega_y \\ \frac{J_z - J_x}{J_y} \omega_z & 0 & \frac{J_z - J_x}{J_y} \omega_x \\ \frac{J_x - J_y}{J_z} \omega_y & \frac{J_x - J_y}{J_z} \omega_x & 0 \end{bmatrix} \quad (5.36)$$



$$\boldsymbol{\Omega} = \begin{bmatrix} 0 & -\omega_x & -\omega_y & -\omega_z \\ \omega_x & 0 & \omega_z & -\omega_y \\ \omega_y & -\omega_z & 0 & \omega_x \\ \omega_z & \omega_y & -\omega_x & 0 \end{bmatrix} \quad (5.37)$$

where $\omega_{[\times]}$ is the skew-symmetric matrix of $\boldsymbol{\omega}$. The predictions are then updated with measurements and corresponding reference vectors. The Kalman gain, \mathbf{K} is defined by Equation (5.38), where \mathbf{R} is the measurement noise matrix and \mathbf{H} is the Jacobian of \mathbf{h} .

$$\mathbf{K}_k = \mathbf{P}_k \mathbf{H}_k^T (\mathbf{H}_k \mathbf{P}_k \mathbf{H}_k^T + \mathbf{R})^{-1} \quad (5.38)$$

The Kalman gain is then used to update the state vector and covariance matrix estimates.

$$\hat{\mathbf{x}}_k = \hat{\mathbf{x}}_k + \mathbf{K}_k (\mathbf{z}_k - \mathbf{h}_k) \quad (5.39)$$

$$\hat{\mathbf{P}}_k = (\mathbf{I} - \mathbf{K}_k \mathbf{H}_k) \hat{\mathbf{P}}_k \quad (5.40)$$

Implementation For the CubeSat, the EKF was applied to the gyroscope with the sun sensors, accelerometer and magnetometer as external reference vectors. The state vector was comprised of 4 quaternions and 3 angular velocities was chosen to describe the attitude and rotation rate, $\mathbf{x} = [q_0 \ q_1 \ q_2 \ q_3 \ \omega_x \ \omega_y \ \omega_z]$. The measurement vector contains the angular velocity measured from the gyroscope, the direction vector of the sun from the sun sensors, the gravity vector from the accelerometer, the magnetic field vector from the magnetometer.

$$\mathbf{z} = [g_x \ g_y \ g_z \ s_x \ s_y \ s_z \ a_x \ a_y \ a_z \ m_x \ m_y \ m_z] \quad (5.41)$$

Reference Vectors To obtain the true sun vector, the ecliptic angle of the sun to the Vernal Equinox is required. This can be calculated by:

$$\sigma = \sigma_{J2000} + \omega_{orbit} t \quad (5.42)$$

σ_{J2000} is the ecliptic longitude at J2000, ω_{orbit} is the rotation rate of the Earth's orbit and t is time since J2000. Since the sun vector lies on the ecliptic plane, the sun vector in the ecliptic frame (EF) is:

$$\mathbf{s}_{EF} = \begin{bmatrix} \cos \sigma \\ \sin \sigma \\ 0 \end{bmatrix} \quad (5.43)$$

This can be converted to Earth Centred Inertial (ECI) by an orthogonal rotation matrix, where ε is the angle between the ecliptic plane and the equatorial plane.

$$\mathbf{s}_{ECI} = \begin{bmatrix} 1 & 0 & 0 \\ 0 & \cos \varepsilon & -\sin \varepsilon \\ 0 & \sin \varepsilon & \cos \varepsilon \end{bmatrix} \mathbf{s}_{EF} \quad (5.44)$$

For the accelerometer, it is known the value of gravity vector will always be $[0 \ 0 \ 1]$ in the North East Down (NED) frame. Thus a known gravity vector in ECI can be obtained by rotating the NED gravity vector to ECI frame with geocentric longitude (ϕ') and latitude (λ'). This will require a rotation from NED to Earth Centred Earth Frame (ECEF) to ECI as shown below.



$$\begin{bmatrix} a_X \\ a_Y \\ a_Z \end{bmatrix} = R_{ECEF2ECI} R_{NED2ECEF} \begin{bmatrix} 0 \\ 0 \\ 1 \end{bmatrix} \quad (5.45)$$

The magnetic field in ECI can be described by the International Geomagnetic Reference Field (IGRF) 13th generation mode [17]. This required the geocentric longitude and latitude, height and decimal year of the CubeSat.

These reference vectors in ECI frame are then converted to the body frame of the CubeSat via the substitution of the estimated quaternions in the rotation matrix below.

$$R_{ECI2BODY} = \begin{bmatrix} q_0^2 + q_1^2 - q_2^2 - q_3^2 & 2(q_1 q_2 - q_0 q_3) & 2(q_1 q_3 + q_0 q_2) \\ 2(q_1 q_2 + q_0 q_3) & q_0^2 - q_1^2 + q_2^2 - q_3^2 & 2(q_2 q_3 - q_0 q_1) \\ 2(q_0 q_2 + q_1 q_3) & 2(q_2 q_3 + q_0 q_1) & q_0^2 - q_1^2 - q_2^2 + q_3^2 \end{bmatrix} \quad (5.46)$$

Observation Matrix The observation matrix is comprised of the Jacobian of each sensor with respect to the state vector. These are stacked as shown below, where the gyroscope only has influence for the angular velocity components. Whilst the other sensors have a 3×3 matrix of zeros, as they only have influence over the attitude.

$$\mathbf{H} = \frac{\partial \mathbf{h}(\mathbf{x})}{\partial \mathbf{x}} = \begin{bmatrix} \mathbf{H}_{gyro} \\ \mathbf{H}_{sun} & \mathbf{0}_{3 \times 3} \\ \mathbf{H}_{acc} & \mathbf{0}_{3 \times 3} \\ \mathbf{H}_{mag} & \mathbf{0}_{3 \times 3} \end{bmatrix} \quad (5.47)$$

$$\mathbf{H}_{gyro} = \begin{bmatrix} 0 & 0 & 0 & 0 & 1 & 0 & 0 \\ 0 & 0 & 0 & 0 & 0 & 1 & 0 \\ 0 & 0 & 0 & 0 & 0 & 0 & 1 \end{bmatrix} \quad (5.48)$$

The format for \mathbf{H} , will be the same for the sun sensors, accelerometer and magnetometer, as they are not influenced by angular velocity. Here x , y and z represent the components a sensors as found in \mathbf{h} .

$$\mathbf{H}_{sensor} = \begin{bmatrix} 2q_0x + 2q_3y - 2q_2z & 2q_1x + 2q_2y + 2q_3z & -2q_2x + 2q_1y + 2q_0z & -2q_3x - 2q_0y + 2q_1z \\ -2q_3x + 2q_0y + 2q_1z & 2q_2x - 2q_1y + 2q_0z & 2q_1x + 2q_2y + 2q_3z & -2q_0x - 2q_3y + 2q_2z \\ 2q_2x - 2q_1y + 2q_0z & 2q_3x + 2q_0y - 2q_1z & 2q_0x - 2q_3y - 2q_2z & 2q_1x + 2q_2y + 2q_3z \end{bmatrix} \quad (5.49)$$

Testing Method

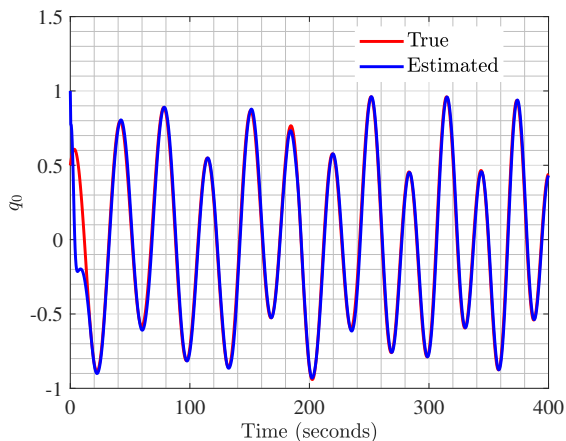
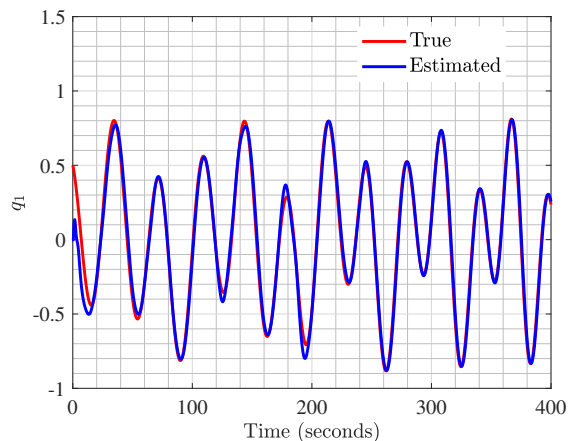
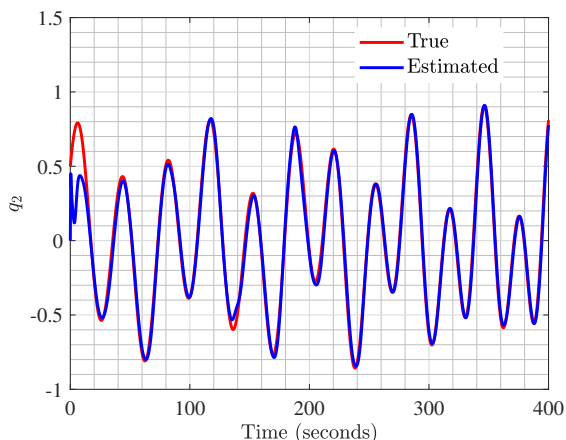
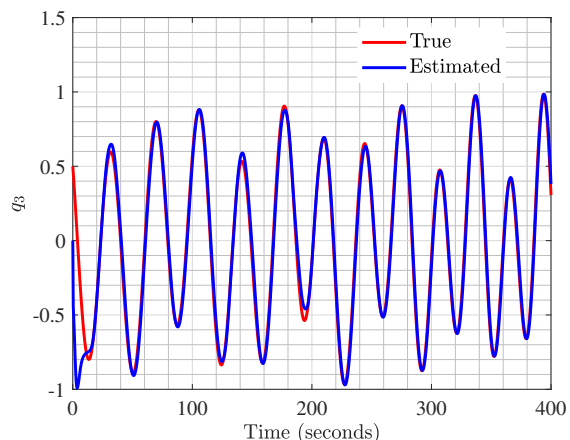
To test the EKF algorithm, it was simulated for 400 seconds with the initial quaternions being $\mathbf{q} = [1 \ 0 \ 0 \ 0]$ and an initial rotational velocity $\omega = [0.01 \ 0 \ 0]$. Whilst a proxy true state vector was propagated, where $\mathbf{q}_{true} = [0.5 \ 0.5 \ 0.5 \ 0.5]$ and $\omega_{true} = [0.1 \ -0.05 \ -0.3]$, mimicking if the satellite was at the equator facing Earth. In order to simulate the measurements from the sensors, white Gaussian noise was added to the known reference vectors.

For sensor measurement noise covariance (σ), the gyroscope had the least confidence due to its susceptibility to drift and noise. The accelerometer and magnetometer had medium confidence as they are not affected by drift, however are subject to changing gravity and magnetic field strengths. Whilst the sun sensor has the highest confidence since it is not affected by any of these factors. In special cases such as solar eclipses, the sun sensor noise covariance will be null.

Table 24: Sensor Noise Variances

Noise variance	Value
σ_{gyro}	0.01
σ_{sun}	0.1
σ_{acc}	0.05
σ_{mag}	0.05

The σ_{model} was estimated to be 0.01, due to errors from the linearisation in the model and the effects of that a bad initial quaternion estimate.

Figure 51: True vs Estimated q_0 from EKFFigure 52: True vs Estimated q_1 from EKFFigure 53: True vs Estimated q_2 from EKFFigure 54: True vs Estimated q_3 from EKF

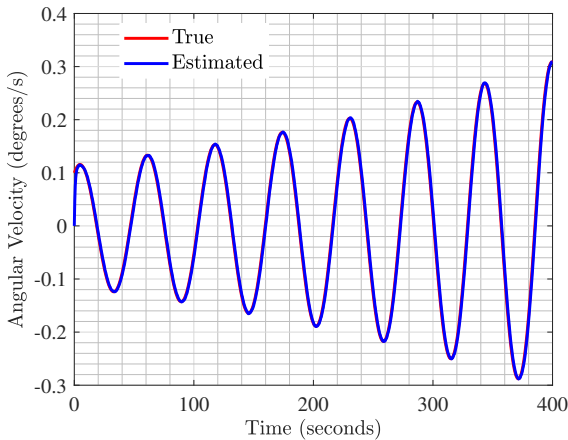
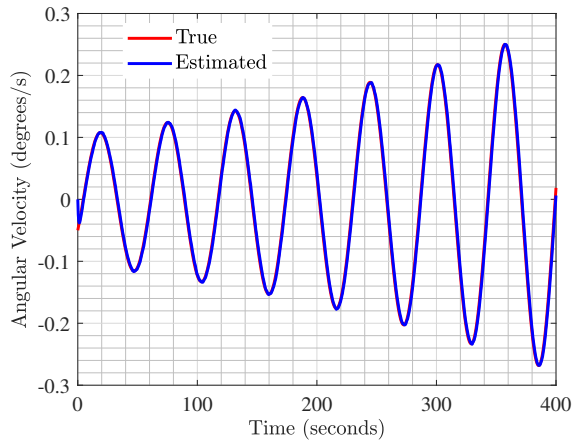
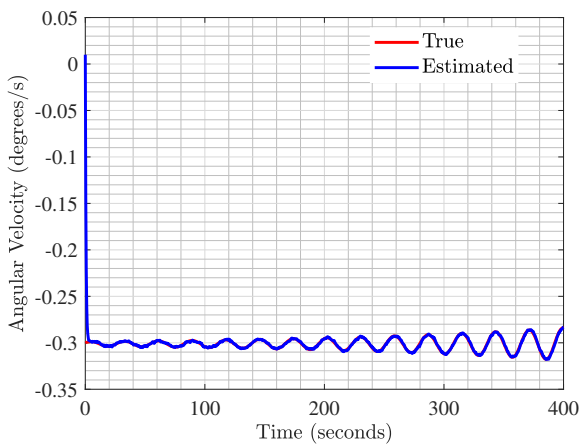
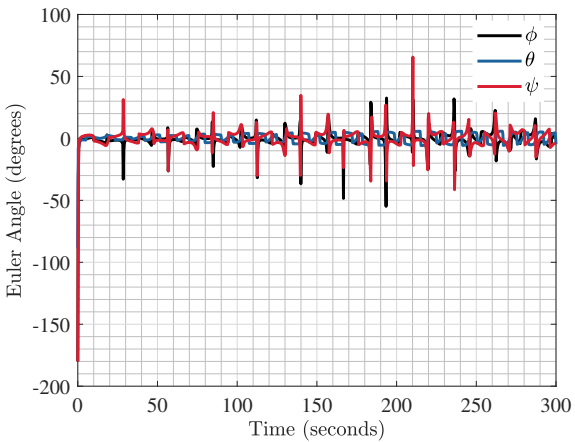
Figure 55: True vs Estimated w_x from EKFFigure 56: True vs Estimated w_y from EKFFigure 57: True vs Estimated w_z from EKF

Figure 58: Error in Estimated Euler Angles Derived from EKF Quaternions

All the states approximately converge to the true attitude within 50 seconds. This is evident in Figures 51, 52, 53, 54, 55, 56, 57. q_1 and q_2 take longer to converge compared to q_3 and q_4 , this is a result of the initial guess. It is predicted when the EKF is paired with the QUEST algorithm this convergence time will reduce. The accuracy of the EKF is visualised in Figure 58. The error in estimation in for yaw is larger than in the roll and pitch direction, which is likely a result of the drift from the gyroscope. Spikes in Figure 58 angle correspond to the peaks and troughs in the quaternion values. At these points the linearisation of the model, introduces increased model errors and produces less accurate results. The average Euler angle error from the EKF is approximately 9.8° , not including outliers. The performance is poorer than expected and what is required in S-AOC-02 46. This could be due to the standard deviation values for each sensor. There is likely to be inconsistencies between the specified noise variance on the data sheet and its performance in reality. For future applications of the EKF, the initial guess of the state vector will be taken from the estimated quaternions given by QUEST to improve the convergence time and robustness. Further simulation for the entire orbit using EKF will also be conducted to test the variation in accuracy over the course of the orbit.

5.3 Attitude Control System

5.3.1 Magnetorquers

In order to counteract the total external torques, the CubeSat will have three magnetorquers, one on each axis. The X and Y axes will utilise a rod design as seen in Figure 59 while the Z-axis will use a flat square coil. This design allows the magnetorquer to provide 3-axis control while utilising less volume than a three rod or three plate design. Air coils were selected to decrease the mass of the structure and to prevent the added complexity associated with core saturation. While this does increase the required number of coils, as seen in the calculations that follow the torque requirements can still be achieved using the air core.

Each coil acts as a solenoid and is driven by an H-Bridge, allowing control of both the direction and magnitude of the current through Pulse Width Modulation (Pulse Width Modulation (PWM)). Pulse Width Modulation (PWM) is a digital technique where analog signals are controlled by varying the width of pulses while maintaining a consistent frequency. This allows the controller to control the average current flowing through the wire of each of the three magnetorquers and hence the magnetic torque produced. Attitude control will be done using a different algorithm for each of the two applications. B-Dot control will be used for detumbling purposes and PD control will be utilised for Nadir Pointing.

The total external torque, (τ_{max}) of $4.14 \times 10^{-7} Nm$ is calculated as the sum of torque due to Gravity Gradient, Solar Radiation Pressure and Atmospheric Darg. Details for these values can be found in

Table 25: Magnetorquer Design Summary

Axis	Solenoid Area (mm ²)	Number of Coils
X	78.54	170 turns
Y	78.54	170 turns
Z	4096	4 turns

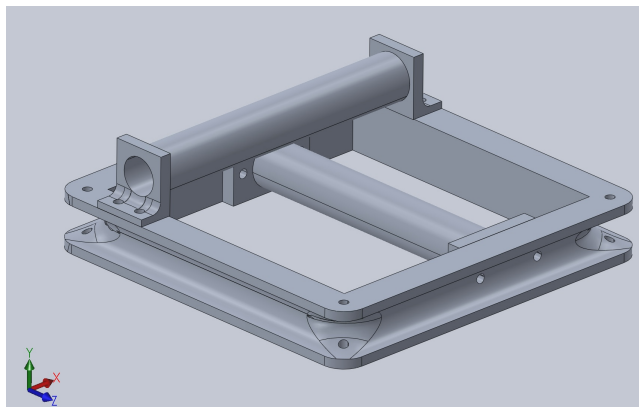
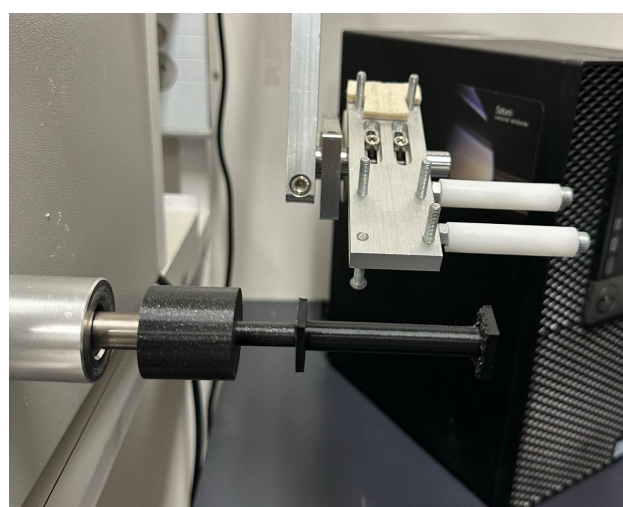


Figure 59: Magnetorquer Assembly

A 0.5 mm Enamel Copper Wire is used for winding as it allows an optimal balance between winding effectiveness and current transfer [18]. A Computer Numerical Conntrol (CNC) Automatic Winding machine was used to precisely control the position, speed and number of turns during the winding process as seen in Figure 60 [19].



(a) Z-Axis Magnetorquer



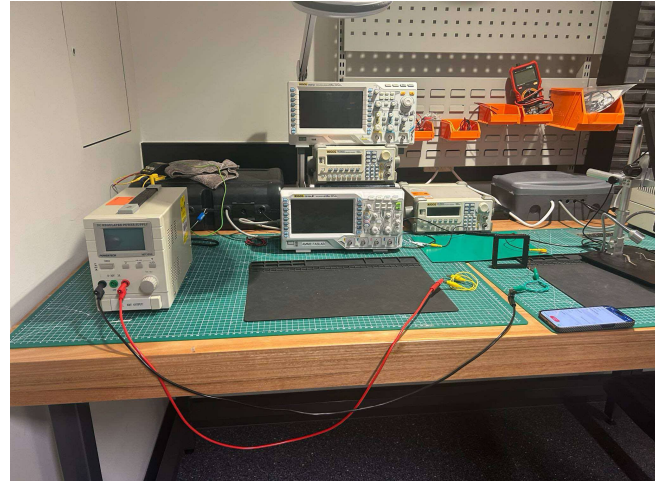
(b) X and Y Axis magnetorquer

Figure 60: Magnetorquer winding setup

To test the magnetic dipole moment produced by each of the three magnetotorquers they were each tested separately using the following procedure. Firstly the enamel on the ends of the wire was scrapped off using a utility knife. The exposed wire on each side of the coil was then connected to a multimeter to test the resistance in the wire. This was done to ensure there was sufficient resistance to avoid a short circuit when the power source is connected. Furthermore knowing the resistance allowed us to calculate the appropriate voltage with the maximum current that will flow through the coils. As seen in Figure 62a there was 2.1 Ohms of resistance in the coil. Using $V = IR$ and the maximum current of 1.2 Amps the testing voltage of 2.5 V was obtained.



(a) Resistance Measured in coil



(b) Magnetotorquer testing setup

Figure 61: Magnetotorquer Testing Procedure and Setup

The magnetotorquer was then connected to a power source with the voltage set to 2.5 V. In order to measure the magnetic dipole produced by the magnetotorquer the MATLAB Mobile Application was used. The mobile app utilises the magnetometer of the iPhone 14 Pro to record the magnetic flux density of the surrounding environment. The magnetotorquer was connected to the power source with long wires so that the magnetotorquer and phone could be placed as far away as possible from the power source to reduce any interference caused by the power source as seen in Figure 61b. The phone was placed 0.30 meters away from the magnetotorquer in line with the centre of the coil. The magnetic flux density sensing was then started taking samples at a frequency of 10 Hz. After

roughly 30 seconds the power source was turned on and the magnetic flux density was measured for another 30 seconds. The results of this for the flat square magnetorquer are shown in Figure 62b.

To quantify the overall change in magnetic flux density due to the magnetorquer the mean magnetic flux density in each of the three directions over the first 30 seconds was calculated. A buffer of 3 seconds was then used to avoid any interference and then the mean magnetic flux density in each of the three directions from 33 seconds to the final sample time was calculated. This essentially provided us with the magnetic flux density without and with the magnetorquer. The difference in each of the three directions was then calculated and these three components were normalised to obtain the overall change in magnetic flux density (ΔB) as $1.373 \mu T$ for the flat square magnetorquer. This was used with the following expression to calculate the magnetic dipole produced by the magnetorquer [20].

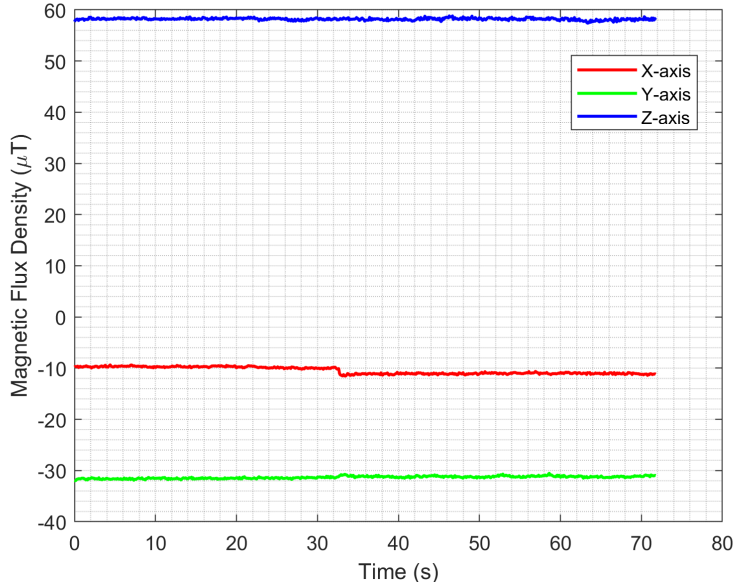
$$\vec{M}_{\text{dipole}} = \frac{4\pi}{\mu_0} \left[\frac{\frac{R_x}{L} - \frac{1}{2}}{\left(R_x^2 - R_x L + \frac{L^2}{4} \right)^{3/2}} - \frac{\frac{R_x}{L} + \frac{1}{2}}{\left(R_x^2 + R_x L + \frac{L^2}{4} \right)^{3/2}} \right]^{-1} \Delta B \quad (5.50)$$

Where R_x represents the distance between the magnetorquer and magnetometer (0.3 m), L represents the total width of all the coil (10×10^{-3} m for the flat magnetorquer) and μ_0 represents the permittivity of free space which is $4\pi \times 10^{-7}$ [20]. For testing purposes 50 coils were used for the Z-axis magnetorquer and this resulted in a final magnetic dipole produced of $0.1852 A \cdot m^2$. This aligns with theory as 8% of 0.1852 (i.e 4/50 coils) is $0.0148 A \cdot m^2$. This shows that the physical magnetorquers preform at 92% of their theoretical capacity.

This process was repeated for the X and Y axis magnetorquers, resulting in the following magnetic flux densities show in Figure 63. Using the same equation the dipole moments were recorded in Table 26.



(a) Mobile Magnetometer Setup



(b) Magnetorquer Z-Axis Results

Figure 62: Magnetorquer measurement and Z-Axis Results

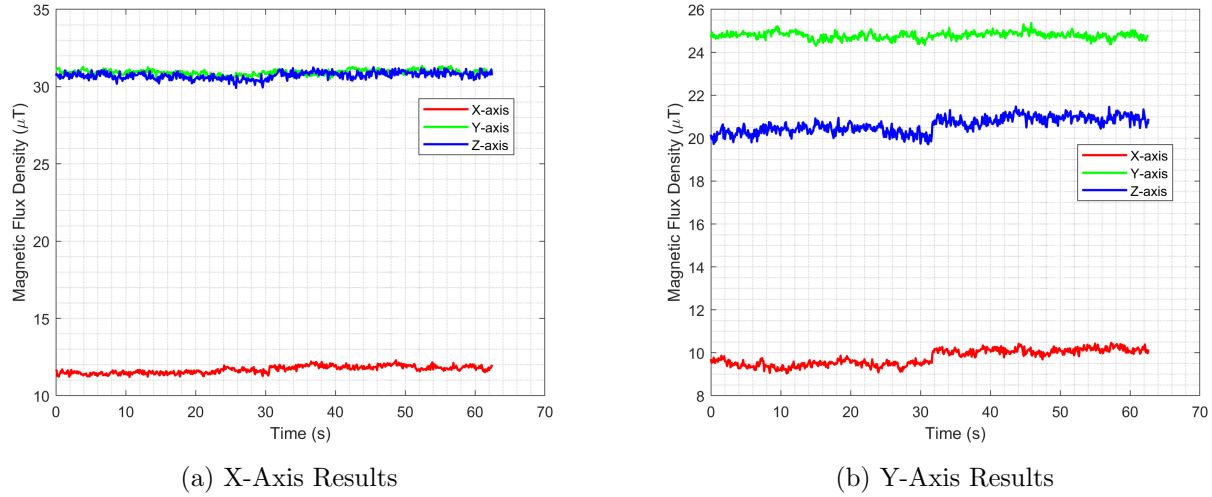


Figure 63: Magnetorquer Testing X and Y Axis Results

Table 26: Magnetorquer Testing Results

Axis	ΔB (μT)	$\mu_{produced}$ ($A \cdot m^2$)	Number of Coils (turns)
X	0.429	0.057	300
Y	0.839	0.111	270
Z	1.373	0.185	50

This validates that all three magnetorquers are able to produce enough magnetic dipole moment to counteract the total external torques.

5.3.2 Detumbling Algorithm (B-Dot)

After deployment, the satellite may have an undesired angular velocity which we term as the initial tip-off rate. A process known as "detumbling" is where the attitude actuators (magnetorquers) work to reduce this initial tip-off to a close to zero angular velocity. The B-Dot algorithm is a simple and effective implementation of detumbling for LEO satellites, using magnetorquers and measurements of the magnetic field via magnetometers to perform effective and efficient detumbling. The mathematical basis of the B-Dot algorithm is the fact that the angular velocity is encoded in the rate of change of the magnetic field. This knowledge is utilized to damp the angular velocity by applying a proportional torque in the direction opposite the angular velocity, without any direct measurements of angular velocity required.

The magnetic dipole moment μ created by a solenoid is defined in Equation B.16, and the torque generated by such a μ is given by

$$\tau = \mu \times \mathbf{B} \quad (5.51)$$

where \mathbf{B} is the magnetic field

We also create a coil matrix which defines the physical properties of the solenoid actuators in each axis as

$$K_{coil} = \begin{bmatrix} N_x A_x & 0 & 0 \\ 0 & N_y A_y & 0 \\ 0 & 0 & N_z A_z \end{bmatrix}$$

Our control moment input \mathbf{u} is then defined as the current I through each coil multiplied by our coil matrix

$$\begin{aligned}\mathbf{u}(t) &= K_{\text{coil}} \cdot [I_x(t) \quad I_y(t) \quad I_z(t)]^\top \\ \mathbf{u}(t) &= K_{\text{coil}} \cdot \mathbf{I}(t)\end{aligned}$$

The required control moment is given by [21] as

$$\mathbf{u}(t) = \boldsymbol{\mu} = -k_{\text{bdot}} \dot{\mathbf{B}} \quad (5.52)$$

where k_{bdot} is a positive scalar gain

Combining 5.52 with B.16, we can calculate the required input current as

$$\mathbf{I}(t) = -k_{\text{bdot}} K_{\text{coil}}^{-1} \dot{\mathbf{B}} \quad (5.53)$$

With a maximum current of I_{sat} , we add saturation to the controller by defining the control current as

$$\mathbf{I}(t) = \begin{cases} -k_{\text{bdot}} K_{\text{coil}}^{-1} \dot{\mathbf{B}} & \text{for } \sum |\mathbf{I}(t)| < I_{\text{sat}} \\ -k_{\text{bdot}} K_{\text{coil}}^{-1} \dot{\mathbf{B}} \cdot \frac{I_{\text{sat}}}{\sum |\mathbf{I}(t)|} & \text{otherwise} \end{cases} \quad (5.54)$$

For simulating our controller, we require a model of the magnetic field in order to calculate \mathbf{B} at each point in our orbit. Using the International Geomagnetic Reference Field (IGRF) 13th generation model [17], we can produce a suitable model of \mathbf{B} which is shown in Figure 64 across two orbital periods.

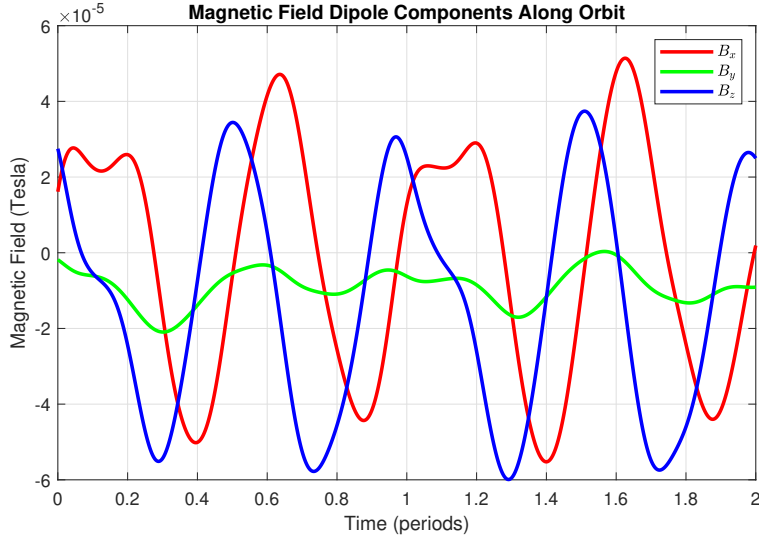


Figure 64: IGRF model of Earth's magnetic field dipole along the orbit in ECI frame

Our model state $\mathbf{X} \in \mathbb{R}^7$ will consist of the angular velocity $\omega \in \mathbb{R}^3$ in rad/s and the attitude quaternion $q \in \mathbb{R}^4$

$$\begin{aligned}\mathbf{X} &= [\omega \quad q]^\top \\ \text{And an initial state } \mathbf{X}_0 &= [\omega_0 \quad q_0]^\top\end{aligned}$$

with $q_0 = [1 \quad 0 \quad 0 \quad 0]^\top$ and ω_0 selected to be from 60 to 100 deg/s in a random direction depending on the experiment.



The Euler rotational dynamics are defined in Equation (5.37). From [22], the derivative of our quaternion \dot{q} is defined below, where Ω is defined in Equation (5.37)

$$\dot{q} = \frac{1}{2}\Omega q \quad (5.55)$$

Recall that $\omega_{[X]}$ is the skew-symmetric matrix of ω .

With $\dot{\mathbf{X}}$ fully defined, along with our control current and initial state, simulations were performed in MATLAB using `ode45` to numerically integrate the system and determine a suitable gain k_{bdot} and saturation current I_{sat} . A successful detumbling was defined as when the angular velocity of the satellite was less than 4 revolutions per orbit, or around 0.2 deg/s.

The results of several simulations can be found in Appendix B.4 with initial tip-off rates of 60 deg/s. The chosen gain and saturation current were $k_{bdot} = 5000$ and $I_{sat} = 0.5$ A which led to a detumbling time of 12.8 hours as shown in Figure 65, successfully fulfilling the requirements of S-AOC-01.

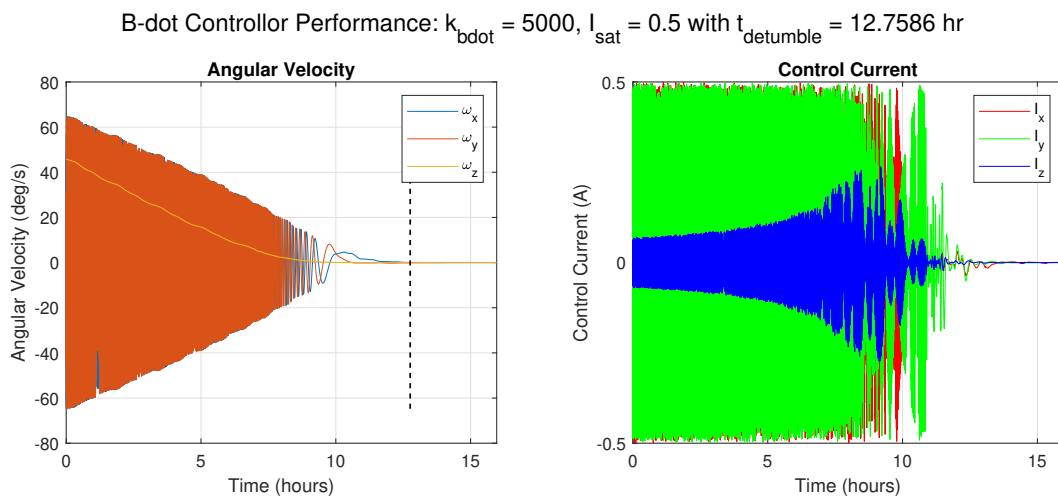


Figure 65: B-Dot detumbling simulation with $k_{bdot} = 5000$, $I_{sat} = 0.5$ and an initial tip-off rate of 60 deg/s

Requirement S-AOC-01 of the ADCS also requires that detumbling can occur even with very large tip-off rates of 90 deg/s or more. It can be observed in Figure 66 that the controller is capable of detumbling such large initial tip-off rates, albeit the time to detumble is longer at 19.3 hours for a 100 deg/s initial angular rate.

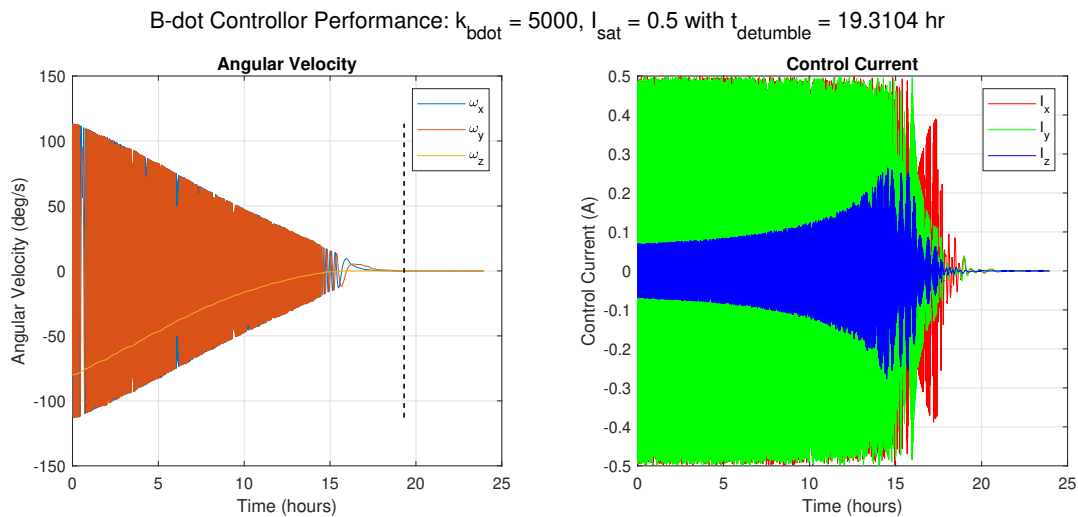


Figure 66: B-Dot detumbling simulation with $k_{\text{bdot}} = 5000$, $I_{\text{sat}} = 0.5$ and a large tip-off rate in excess of 100 deg/s

5.3.3 Nadir Pointing Algorithm (PID)

Proportional-Derivative Controller

Our nadir-pointing control algorithm will be used during the payload mode to ensure that the spectrometer has a consistent view of the Earth's surface. Given that extreme pointing accuracy is not required for the spectrometer, a Proportional Derivative (PD) was chosen to be implemented. However, during simulation testing it was found there was a large steady-state error of up to 15 degrees, therefore the choice to use PD was reconsidered.

Proportional-Integral-Derivative Controller

To fix the problems of the PD controller, an integrating term was added to erase steady state error, making the chosen controller a Proportional-Integral-Derivative (PID) controller. A PID controller takes the form of

$$\begin{aligned} \mathbf{u}(t) &= K_p \mathbf{X}_e - K_d \dot{\mathbf{X}} + K_i \int_0^{\infty} \mathbf{X}_e dt \\ \mathbf{u}(t) &= K_p (\mathbf{X} - \mathbf{X}_{\text{ref}}) - K_d \dot{\mathbf{X}} + K_i \int_0^{\infty} (\mathbf{X} - \mathbf{X}_{\text{ref}}) dt \end{aligned} \quad (5.56)$$

(5.57)

where K_p , K_d and K_i are scalar gains.

In our case, our full state remains as $\mathbf{X} = [q \ \omega]^T$ and the term \mathbf{X}_e will be the quaternion error and is given by

$$\tilde{q} = q_d^{-1} \otimes q$$

where \otimes represents the quaternion multiplicative function

Since the scalar part of the quaternion q_0 is not relevant to the error term, we exclude it from the controller i.e. $\tilde{q} = [\tilde{q}_1 \ \tilde{q}_2 \ \tilde{q}_3]^T$. We can then form our full controller equation

$$\tau(t) = K_p \tilde{q} - K_d \omega + K_i \int_0^t \tilde{q} dt \quad (5.58)$$

where the quaternion q_e is the nadir-pointing quaternion. Since quaternions are symmetric, the shortest rotation is chosen. Algorithm 1 demonstrates the pseudocode for calculating the error quaternion at a given point in the orbit.



Algorithm 1 Compute Nadir-Pointing Reference Quaternion and Attitude Error

Require: ECI position vector r_{eci} , ECI velocity vector v_{eci} , current quaternion q

Ensure: Reference quaternion q_{ref} , quaternion error q_{err} , Euler angle error, pointing error

```

1:  $r_{unit} \leftarrow r_{eci}/\|r_{eci}\|$ 
2:  $z_{nadir} \leftarrow -r_{unit}$ 
3:  $h_{orbit} \leftarrow r_{eci} \times v_{eci}$ 
4:  $y_{orbit} \leftarrow h_{orbit}/\|h_{orbit}\|$ 
5:  $x_{orbit} \leftarrow y_{orbit} \times z_{nadir}$ 
6:  $x_{orbit} \leftarrow x_{orbit}/\|x_{orbit}\|$ 
7:  $y_{orbit} \leftarrow z_{nadir} \times x_{orbit}$ 
8:  $y_{orbit} \leftarrow y_{orbit}/\|y_{orbit}\|$ 
9:  $R_{desired} \leftarrow [x_{orbit}, y_{orbit}, z_{nadir}]$ 
10:  $q_{ref} \leftarrow \text{dcm2quat}(R_{desired})$ 
11:  $q_{ref\_conj} \leftarrow \text{quatconj}(q_{ref})$ 
12:  $q_{err} \leftarrow \text{quatmultiply}(q_{ref\_conj}, q)$ 
13:  $q_{err} \leftarrow q_{err}/\|q_{err}\|$ 
14: if  $q_{err}[1] < 0$  then
15:    $q_{err} \leftarrow -q_{err}$ 
16: end if
17:  $euler\_angle\_error \leftarrow \text{rad2deg}(\text{quat2eul}(q_{err}))$ 
18:  $pointing\_error \leftarrow 2 \cdot \text{rad2deg}(\arccos(|q_{err}[1]|))$ 
19: return  $q_{ref}, q_{err}, euler\_angle\_error, pointing\_error$ 

```

Under-actuation in the Magnetorquer Control Problem

There is a crucial problem with using only magnetorquers for an attitude pointing controller. While Equation 5.58 reveals the adequate torque which needs to be enacted on the satellite body, this torque isn't always able to be produced by the magnetorquers alone. This is because magnetorquers can only generate torque perpendicular to the magnetic field $\perp \mathbf{B}$, and thus, at all times the magnetorquer is inherently under-actuated and cannot generate any torque parallel to the magnetic field $\parallel \mathbf{B}$.

When using a PID controller, this can lead to what is known as "integral wind-up" where the integral term accumulates significant error in the periods where the goal attitude is unreachable, then when the magnetic field has changed over time s.t. the attitude is now reachable, the controller will overshoot due to the large buildup of error. To avoid this, the integral term will be saturated to prevent accumulation of error.

PID Controller Setup

The controller in Equation 5.58 was then simulated in MATLAB with the Simulink model shown in Figure 67.

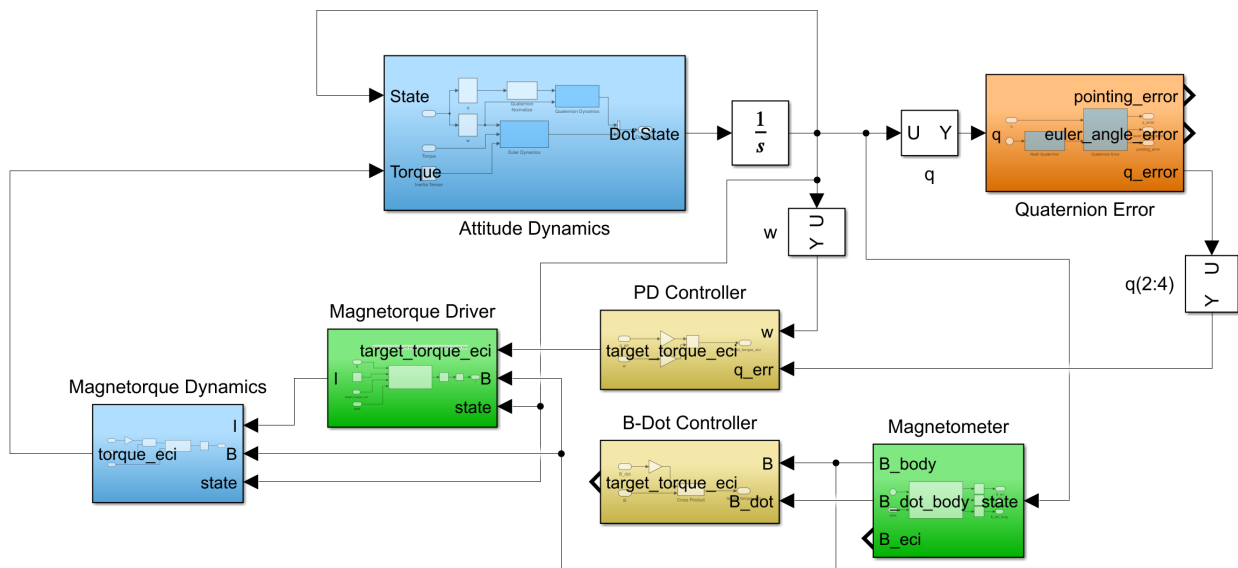


Figure 67: MATLAB Simulink model of the PID Nadir-Pointing controller

The interior view of the PID Controller Block in Figure 67 is shown in Figure 68.

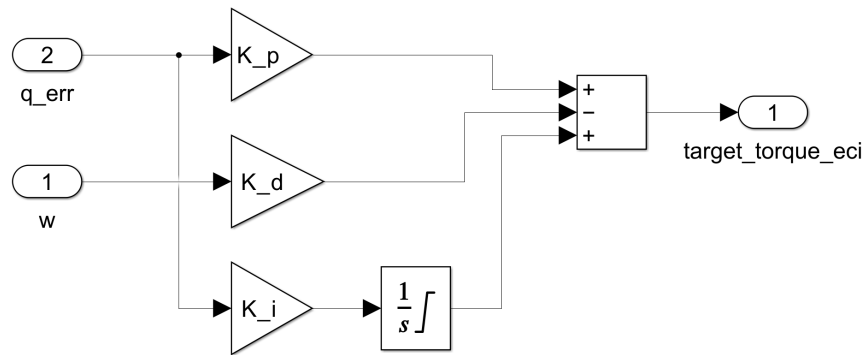


Figure 68: Interior view of PID controller block in Simulink.



In order to tune our controller, we can use auxiliary parameters to find approximate gains which can be further tuned by trial and error to achieve the desired behaviour. Coefficient matching with a standard second-order system [23] yields the following design equations for our controller.

$$\begin{aligned} K_p &\approx \omega_n^2 \cdot \mathbf{J} \\ K_d &\approx 2 \cdot \zeta \cdot \omega_n \cdot \mathbf{J} \\ K_i &\approx 1 \times 10^{-3} K_p \end{aligned}$$

where ω_n is the desired natural frequency of the system in rad/s, chosen to be 0.01, and ζ is the damping coefficient, chosen to be 0.7 for a slightly under-damped system. The coefficients used are set out in Table

Table 27: PID Controller Parameters

Parameter	Value
K_p	2.01e-6
K_d	2.94e-4
K_i	2.01e-9
K_i (saturation)	$\pm 1\text{e-}6$

PID Controller Results

The simulation was run for two orbital periods, with an initial state of $x_0 = [1 \ 0 \ 0 \ 0 \ 0 \ 0.01 \ 0, \ 0.01]^\top$, that is, the satellite is assumed to have already been detumbled and thus has a very small angular rate but has a large pointing error. Shown in Figure 69 are the results of the simulation for the quaternion components, command current supplied to the magnetorquers, absolute Euler angle error and the component Euler angles over time.

It can be seen that the controller achieves a steady-state pointing error of approximately 1.24° , satisfying the mission requirement S-AOC-02. However, there are instances where the pointing error jumps as high as 4.2° , as seen around the 100 minute mark in Figure 69. This is likely due to a quaternion component switching sign, and the integral component needs time to erase the error it had built up, which could speak to the suitability of a PD controller over a PID if it can be tuned correctly.

The integral gain K_i was increased by a factor of 5 and the simulation was rerun. The results are seen in Figure 70. It is clear that by increasing the integral gain, the overshoot occurrences due to sign-switching become more pronounced, in this case the pointing error exceeds 8.8° .

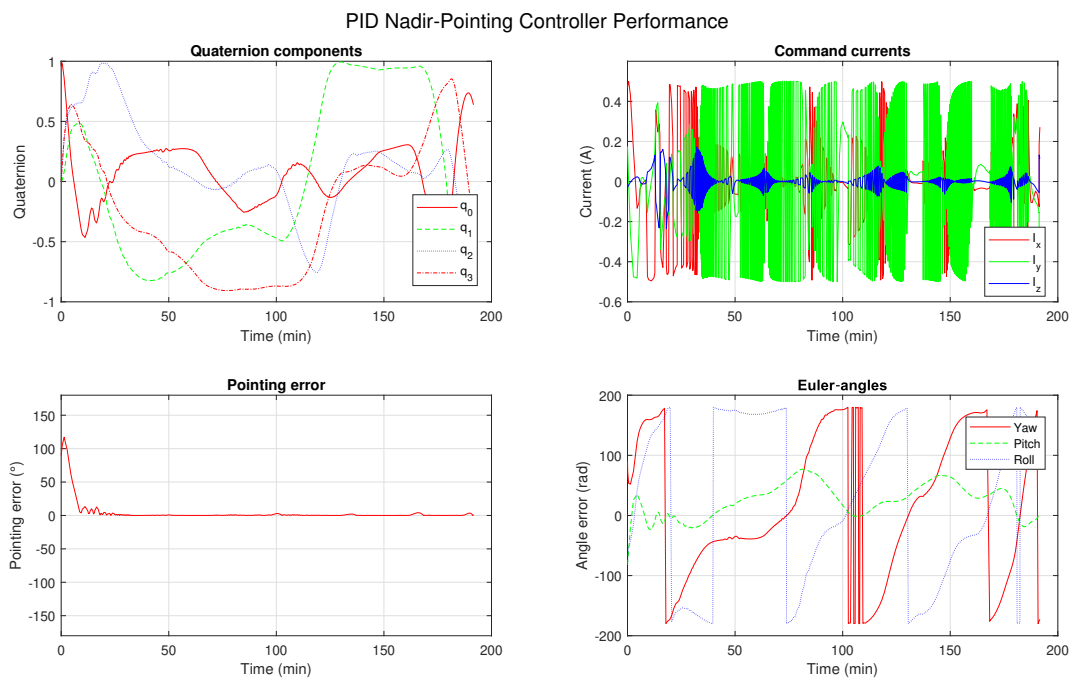


Figure 69: PID Nadir-pointing controller simulation with parameters from Table 27

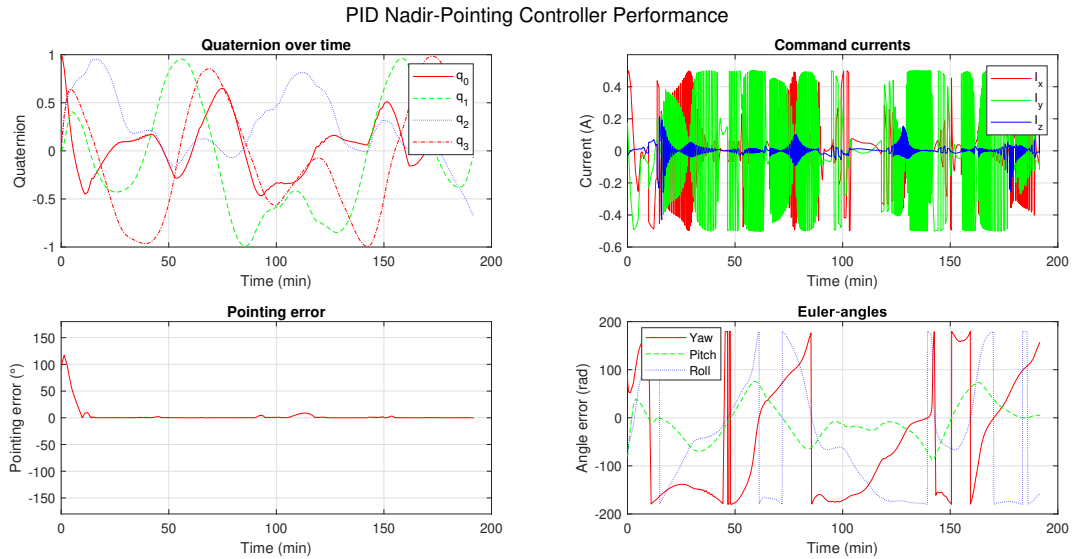


Figure 70: PID Nadir-pointing controller simulation with K_i increased 5-fold

6 Electrical Power Subsystem

6.1 Overview

The Electronics and Power Subsystem (EPS) is responsible for providing stable and reliable power to the CubeSat system throughout all modes of operation. The main components of this subsystem are solar panels for power generation, batteries for energy storage to provide stable power during eclipses and low-power scenarios and voltage regulators to regulate the power buses on the CubeSat. Other components include solar charging and protection circuitry, as well as battery protection circuitry and current sensors.

6.2 Block Diagram

A block diagram of the EPS is shown in Figure 71. The diagram includes blocks for complicated circuits which have their own detailed diagrams in later sections of this report. The solar panels are connected in a 1s7p fashion, where the three pairs of panels and the one individual panel each have a current sensor for measuring power production. There are two Single-Pole Single-Throw (SPST) switches as part of our RBF system. Two spring action mechanical switches located on the bottom of our CubeSat will ensure that these SPST switches are open while inside the deployer and will only be closed, allowing power to flow from the solar panels and batteries, once deployed.

The power from the solar panels is passed through a reverse polarity protection circuit, which prevents back-current to the panels. The solar charger controller converts the solar power to a suitable voltage to charge the batteries in a CCCV manner (constant-current then constant voltage). A battery protection IC is used between the batteries and the rest of the circuit to maintain battery health and safety. Voltage regulators use either the solar power, battery power or a combination to provide stable 3.3 and 5 volt power for the rest of the system.

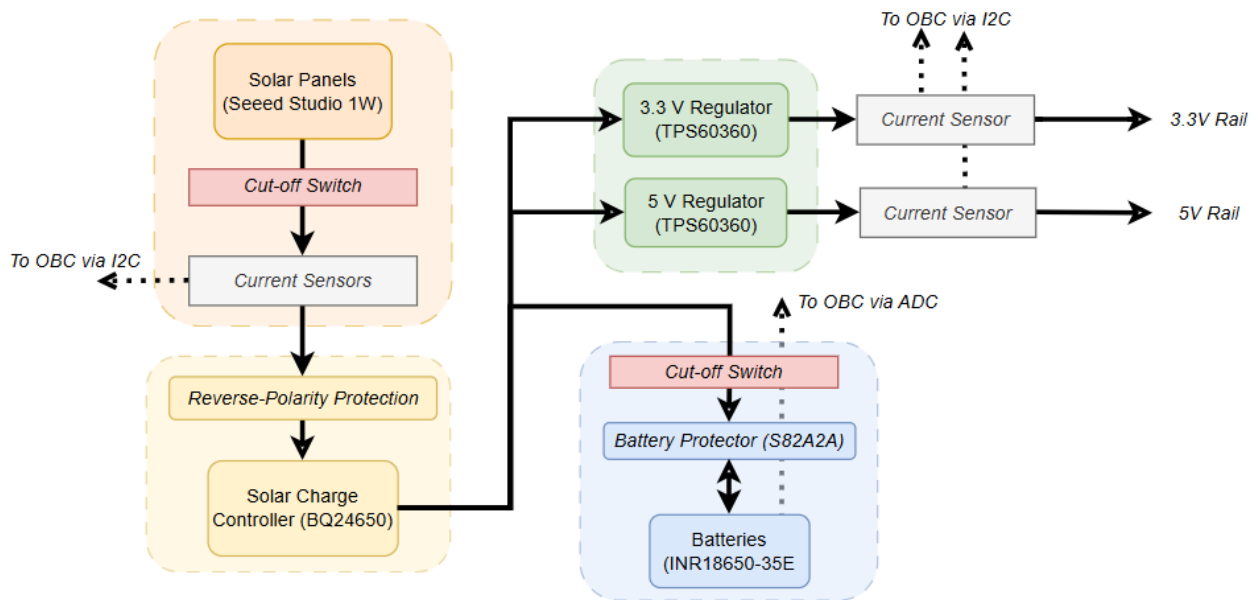


Figure 71: Block diagram of the EPS

6.3 Components

The major components used in the EPS are laid out in Table 28. Some components will be used as Commercial-Off-The-Shelf (COTS), which are the solar panels and batteries, however in-house designs will be used for the solar charge controller, battery protection, voltage regulators and current

sensing circuits. In-house designs allow us to save on up-front costs, better manage our PCB layout and make any modifications to better suit our particular needs. "Various components" in Table 28 refers to simple electrical components including resistors, capacitors, inductors and MOSFETs.

Table 28: EPS Component Summary

Component	Sub-components	#	Type	TRL
Solar Panels	Seeed Studio 1W 80x100mm	7	COTS	4
Batteries	Samsung INR18650-35E 3500mAh Li-Ion Battery	2	COTS	4
Solar Charge Controller	TI BQ24650, various components	1	In-house	4
Battery Protection	S-82A2A, various components	1	In-house	4
Voltage Regulator	TI TPS63060, various components	2	In-house	4
Current Sensors	TI INA219A, various components	6	In-house	4

6.3.1 Solar Panels

The chosen solar panels were the Seeed Studio 1W 80x100 Solar Panels, with 7 of these panels connected in a 1s7p arrangement. Each side has its own current sensors to monitor the performance of the panels, as well as a reverse-polarity protection circuit to protect the panels from back current.

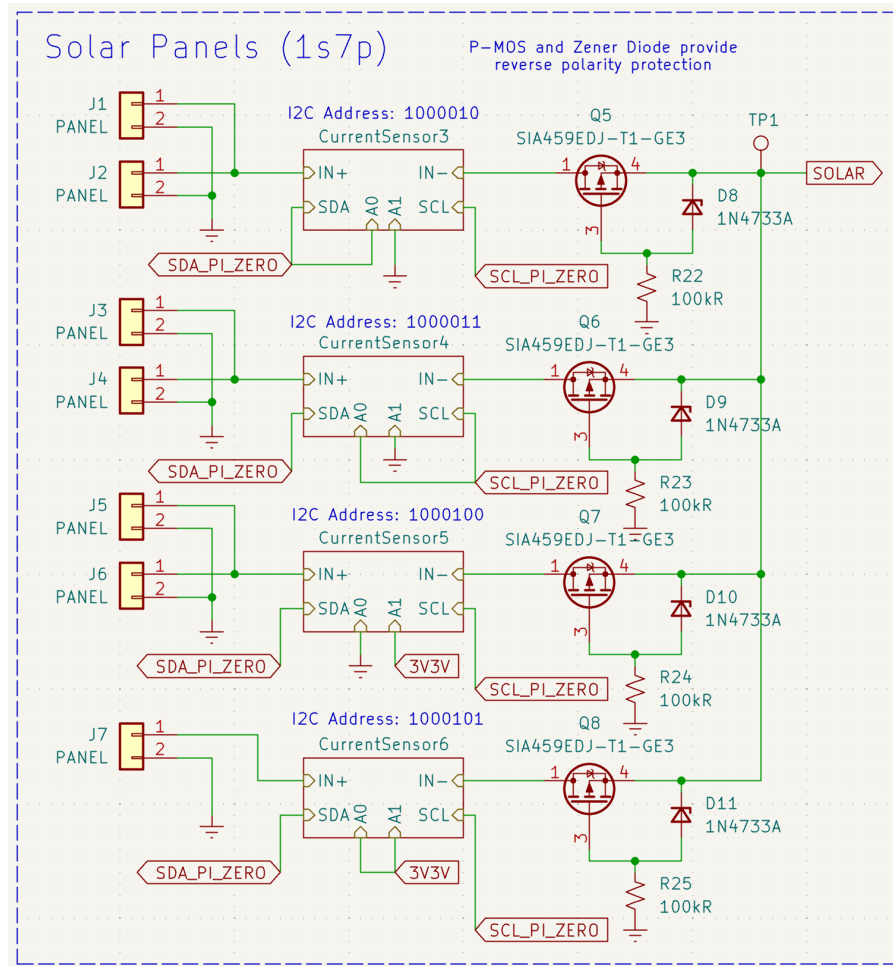


Figure 72: Solar panel circuitry including current sensing and reverse polarity protection

The solar panels are advertised to typically produce 5.5V at 170mA yielding a typical power production of

$$P = 5.5 \text{ V} \times 0.170 \text{ mA} = 0.935 \text{ W}$$



However, experimental testing was performed and determined that the maximum power production was around 0.75W, 20% less than expected. The experimental PV and IV curves shown in Figure 73 plot power versus current and power versus voltage and are useful for determining under what conditions the panel produces maximum power. These curves were determined by varying a load resistance across the panel and measuring the voltage drop. The Maximum Power Point (MPP) is the voltage at which maximum power is extracted from the solar panel, and was determined to occur at a load voltage of approximately 4.75V.

Due to thermal cycling in and out of eclipses, the solar panel efficiency will degrade over its lifetime. For a silicon solar array in LEO over a 12 month mission, its lifetime degradation [10] can be given by

$$L_d = (1 - 0.0375/\text{yr})^{\text{mission yrs}} \quad (6.1)$$

$$L_d = 96.25\% \quad (6.2)$$

Thus, as a worst case we will assume that the maximum power production of any panel is then

$$\begin{aligned} P_{\max} &= 0.9625 \times 0.75 \\ &= 0.70 \text{ W} \end{aligned}$$

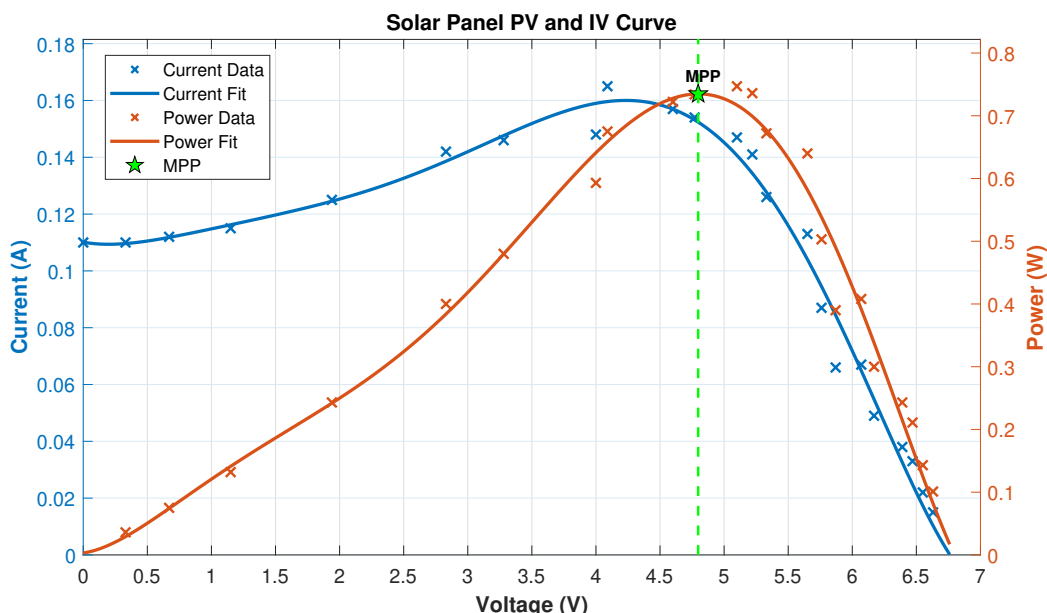


Figure 73: Experimentally obtained Power-Voltage and Current-Voltage curves of a single solar panel

6.3.2 Batteries

The chosen batteries are the Samsung INR18650-35E 3500mAh 8A Li-Ion Battery. This was chosen in contrast to the originally suggested battery from our PDR as the Samsung battery has pre-welded tabs for ease of integration and boasts a larger capacity. Two of the batteries are placed in series (2s) to yield a nominal voltage of 7.6 V at 3500 mAh.

To prevent damage to the battery, we will implement a maximum Depth-of-Discharge (DoD) limit of 80%. We want to prevent a DoD greater than 80% in order to maintain the battery health as deeply discharging Li-Ion batteries can alter their internal cell chemistry and reduce their lifespan. Figure 74, courtesy of [24], plots the DoD in Amp-hours and the corresponding battery terminal voltage. At a DoD of 80% (2.8 Amp-hours) the corresponding terminal voltage is expected to be around 3.4 V, which for our 2s setup gives a cut-off voltage of 6.8 V. To implement this cut-off, the battery voltage

is read by an Analog to Digital (ADC) converter and the OBC uses the digital reading in the state transition functionality.

Given that we will only ever discharge 2.8 Ah of charge, the battery capacity is then

$$C = 2.8 \text{ Ah} \times 7.6 \text{ V}$$

$$C = 21.2 \text{ Wh}$$

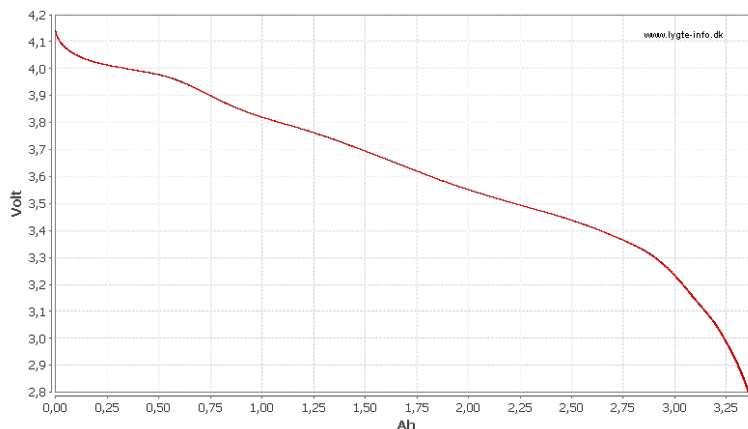


Figure 74: Discharge curve of the INR18650-35 Li-Ion Battery

6.3.3 Reverse-Polarity Protection Circuit

To ensure longevity of the solar panels, a reverse-polarity protection circuit is implemented for each side of the CubeSat using a P-Channel MOSFET as well as a Zener diode. Back-current is problematic for solar panels as it causes them to act as a load instead of a generator, dissipating power as heat which reduces the efficiency of the system and can also shorten the lifespan of the device.

Normally, a Schottky diode would be used to prevent back-current but such diodes typically have a voltage drop of around 0.7V, and thus dissipate a significant amount of power - unideal for our CubeSat system where power margins are slim. Combining a P-MOSFET with a Zener diode as shown in Figure 75 provides back-current protection with a much smaller voltage drop

For the P-MOSFET, the SIA459EDJ from Vishay was chosen for its low $R_{DSon} = 28 \text{ m}\Omega$ to minimize power dissipation. Its drain-source breakdown voltage is -20V, and has a maximum gate-source voltage of $\pm 12\text{V}$. The 1N4733A Zener Diode from Fairchild has a zener voltage V_z of 5.1V, which clamps the gate-source voltage to ensure it does not exceed the 12V rating.

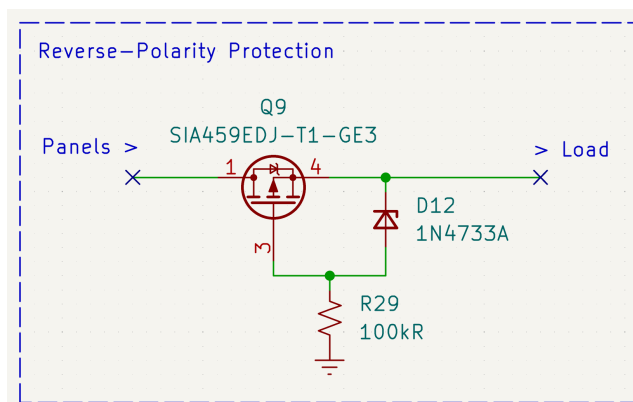


Figure 75: EPS Solar panel reverse polarity protection circuit diagram, the P-MOS terminal 1 is connected to the solar panel positive terminal, and P-MOS terminal 4 connected to the load

The circuit was simulated in LTSpice as shown in Figure 76. The simulated circuit in Figure 76a uses a step voltage source to simulate a change in polarity, and an arbitrary resistor as the load. In Figure 76b, the polarity of the source changes at $t = 1\text{s}$ from 12V to -12V for 1.2s and we can see the load voltage and current drop to zero indicating that no current flows through the circuit when the polarity is incorrect.

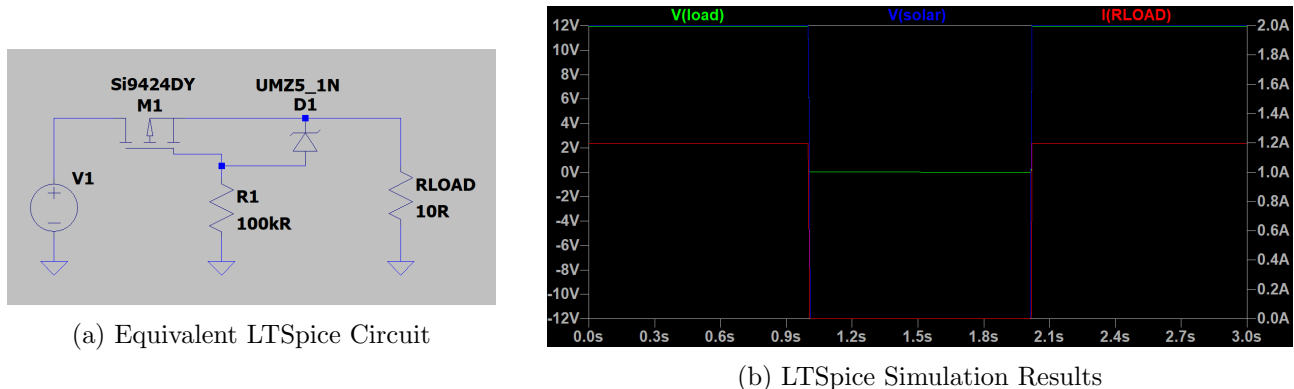


Figure 76: Reverse polarity protection circuit simulation in LTSpice

6.3.4 Solar Charge Controller Circuit

The solar charge controller is centered around the BQ24650 Stand-Alone Synchronous Buck Battery Charge Controller for Solar Power With Maximum Power Point Tracking [25]. The charge voltage can be specified through a resistor divider with equation

$$V_{\text{BAT}} = 2.1 \times \left[1 + \frac{R_{18}}{R_{19}} \right]$$

For our battery configuration, the Li-Ion cells can be charged to a voltage of 4.2V, thus for two cells in series we require $V_{\text{BAT}} = 8.4\text{V}$ which gives us the required ratio to determine the charge voltage as

$$\frac{R_{18}}{R_{19}} = 3$$

and setting $R_{19} = 100\text{ k}\Omega$, we have $R_{18} = 300\text{ k}\Omega$

To set our charge current, the relevant equation is

$$I_{\text{CHARGE}} = \frac{40\text{ mV}}{R_{\text{SR}}}$$

and selecting $R_{\text{SR}} = 20\text{ m}\Omega$ yields a charge current of 2A.

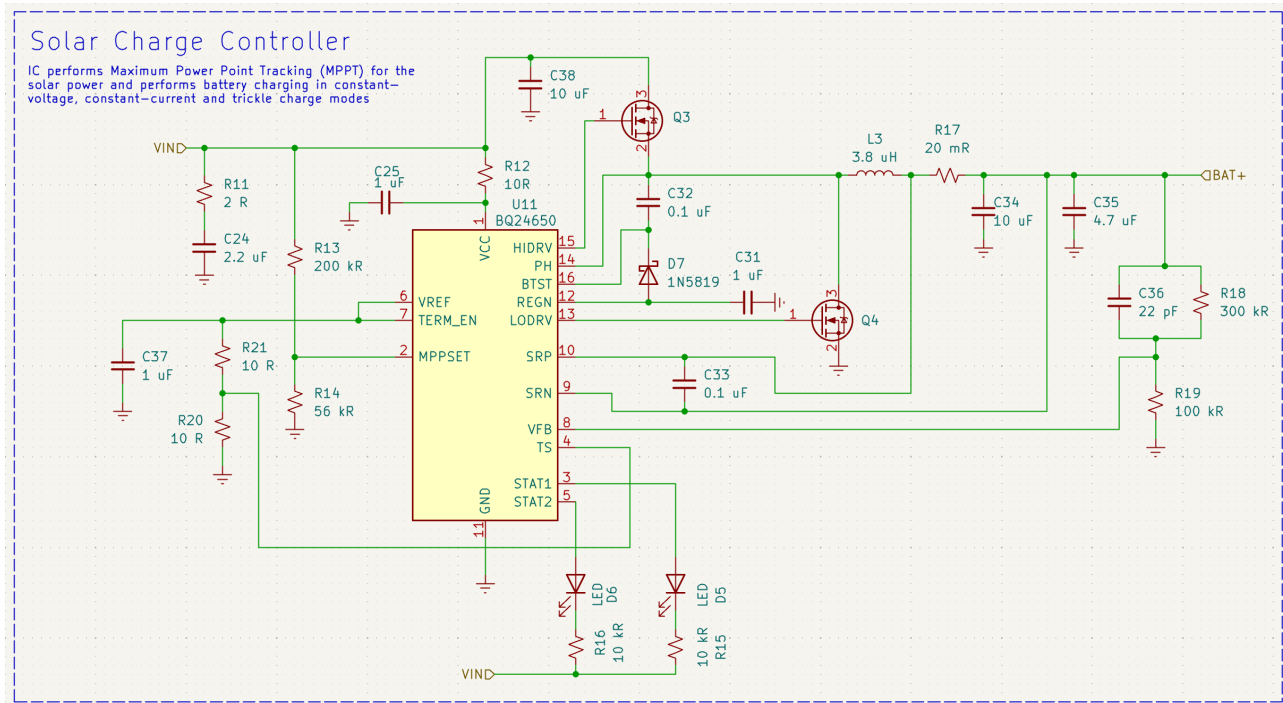


Figure 77: EPS Solar power charge controller circuit diagram

6.3.5 Battery Protection Circuit

The battery protection circuit is centered around the S82A2A Battery Protection IC for 2s Battery Pack [26]. This IC provides the following functionality

- Over-voltage protection
 - Over-discharge protection
 - Discharge over-current protection
 - Charge over-current protection

The pins C0 and D0 in Figure 78 are two gate driving pins for N-Channel MOSFETs which activate when any adverse conditions are detected, disconnecting the battery negative terminal from the charging source.

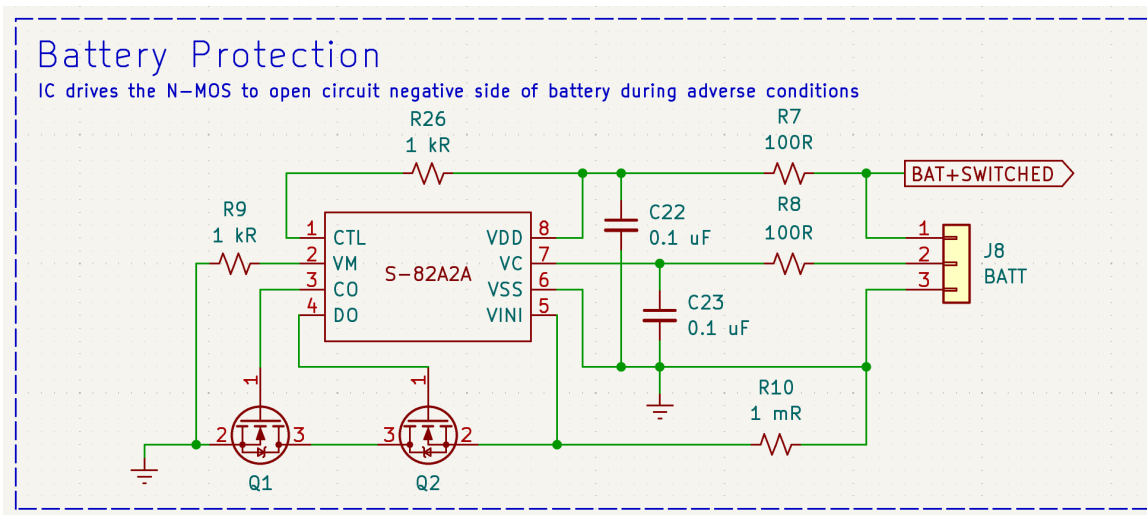


Figure 78: EPS Battery protection circuit diagram



6.3.6 Voltage Regulation Circuit

The voltage regulation circuits are based on the TPS63060 High Input Voltage, Buck-Boost Converter With 2-A Switch Current [27]. The output voltage is determined by the resistor divider between V_{OUT} and FB . For the 3.3 V regulator,

$$R_5 = R_4 \left(\frac{V_{OUT}}{V_{FB}} - 1 \right)$$

Given a typical voltage at the FB pin of 500mV [27], and choosing $R_5 = 120 \text{ k}\Omega$, we can calculate the required R_4 for 3.3V (and R_1 for 5V) respectively and choose the closest value in the E24 resistor series giving

$$3.3\text{V}: R_4 = 680 \text{ k}\Omega$$

$$5\text{V}: R_1 = 1.1 \text{ M}\Omega$$

In Figure 79 the efficiency of the regulators can be seen against their output current in Amps. For an output current between 0.05 and 2 A, efficiencies greater than 80% are achieved, while for output current between 0.2 and 1 A even 90% efficiency are possible. For subsequent power consumption analysis, we will assume that the converters are operating at 80% as a worst case assumption.

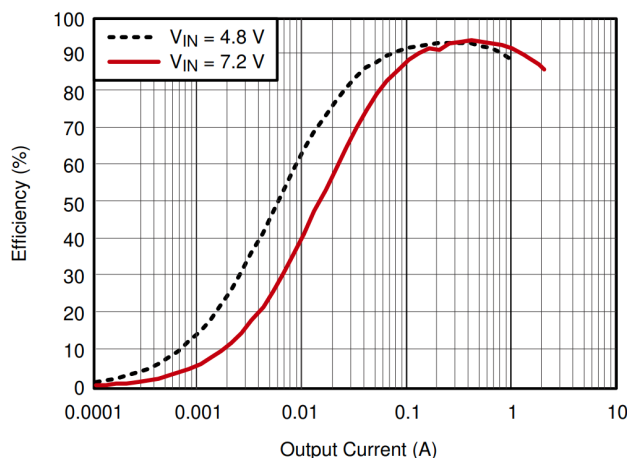


Figure 79: Efficiency versus output current (A) for TPS63060 voltage regulator

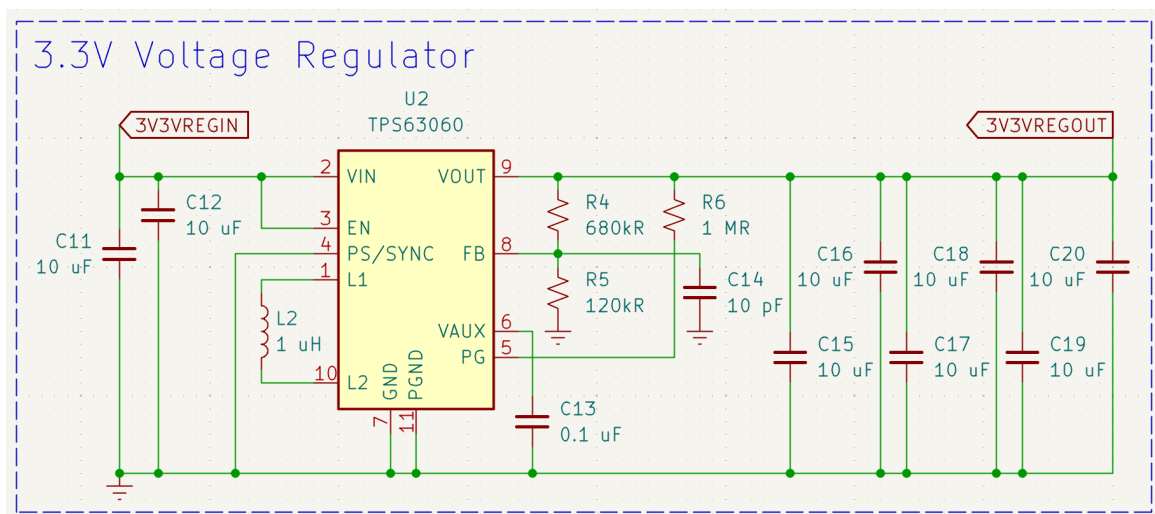


Figure 80: EPS 3.3V voltage regulator circuit diagram



6.3.7 Current Sensing Circuit

The current sensing circuit uses the INA219A Zero \varnothing -Drift, Bidirectional Current/Power Monitor with I2C Interface. The recommended layout from the datasheet [28] was followed closely and is shown in Figure 81. The INA219A interfaces well with I2C which is suitable for integration with our OBC. Two pull-up resistors ensure an appropriate voltage level for the clock (SCL) and data (SDA) lines of the I2C interface.

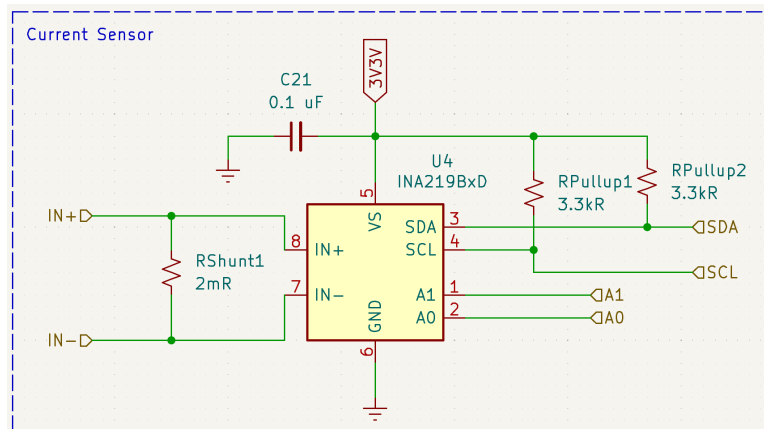


Figure 81: EPS Current sensing circuit diagram

6.3.8 Kill-Switch

As part of our RBF system, we have two mechanical SPST kill-switches to isolate both the solar panels and the batteries from the system before deployment, fulfilling requirement S-EPS-03.

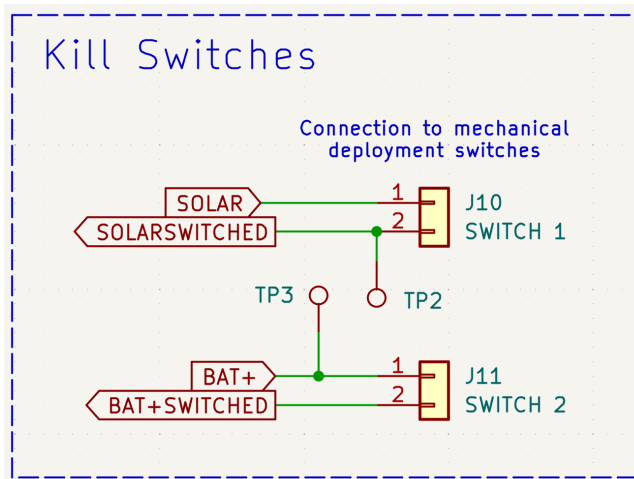


Figure 82: Kill switch circuitry for the solar panels and batteries

6.4 PCB Design

The choice was made to design the PCB in-house. This allows us to save on costs and gives us more freedom in the placement of components in order to save area and the interfaces we use. The ground plane of the EPS PCB also has a capacitive effect which serves to further stabilize the power supplies. Section 7.2 contains a more detailed description of the EPS PCB design process.

6.5 Power Budget

In the following sections, the power consumption of the subsystems with electrical components was considered, along with the power generation of the solar panel. The total power budget can be found



tabulated in the Appendix.

6.5.1 Power Generation Analysis

The power generation (in W) of the solar panels was simulated in MATLAB over two full orbital periods and is plotted in Figure 83. The time spent in sunlight was around 62.9% of the orbital period. It can be observed that power generation peaks at approximately 1.5W, and by integrating the power generation curve we can determine the energy produced in one period

$$\int_0^T P(t)dt = 1.06 \text{ Wh}$$

where $P(t)$ is the solar power produced at time t

Given our batteries have a capacity of 21.2 Wh, it would take 20.0 orbits to charge them from discharged.

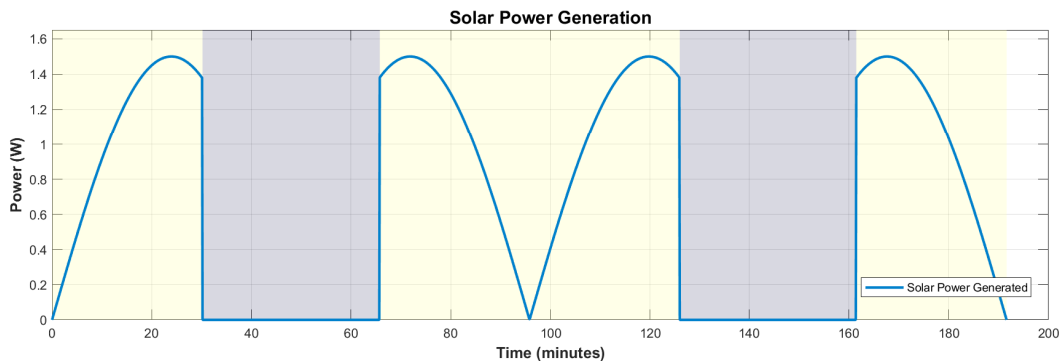


Figure 83: Solar power generation by the solar panels over two full orbital periods

6.5.2 EPS Power Consumption

The EPS itself consumes power through battery charging and inefficiencies in the system. The voltage regulators were previously assumed to work at 80% efficiency as a worst case scenario, the power consumption of the regulators is thus based on the current draw. At a nominal current draw of 0.5 A, the efficiency is 90%, thus the power dissipation is approximately 55 mW.

The reverse-polarity protection circuit has a max power dissipation of $(160 \text{ mA})^2 \times 28 \text{ m}\Omega = 1 \text{ mW}$. The current sensors have a shunt resistance of only 2 mΩ and thus dissipate about 1 mW of power as well. All EPS components are always on and thus the duty cycle is the same for all modes.

The total efficiency of the EPS system given the efficiencies of all sub components is approximately 78%

Table 29: EPS Component Power Usage Across Modes of Operation

Component	#	Power (W)	Mode (Duty Cycle %)
			Nominal
3.3V Voltage Regulator	1	55 mW	100
5V Voltage Regulator	1	55 mW	100
Polarity Protectors	4	1 mW	100
Current Sensors	6	1 mW	100

6.5.3 OBC Power Consumption

The components in the OBC subsystem which will consume power are the Raspberry Pi Pico and Raspberry Pi Zero. The Zero typically consumes around 110 mA with a 5 V power supply giving a 0.55 W power consumption. The Pico consumes less at around 50 mA also at 3.3 V, giving a 0.165 W power draw. In Nominal mode, with several peripherals and GPIO pins active we can assume both boards draw full power, however in Safe mode less peripherals are powered and thus the duty cycle is set at 75%.

Table 30: OBC Component Power Usage Across Modes of Operation

Component	#	Power (W)	Mode (Duty Cycle %)	
			Nominal	Safe
Raspberry Pi Zero W	1	0.55	100	75
Raspberry Pi Pico	1	0.165	100	75

6.5.4 ADCS Power Consumption

The IMU has a consumption of around 14 mA during typical use with an input voltage of 3.3 V, yielding a power consumption of 46 mW. During Safe mode, less complex and therefore less power intensive ADS methodology may be used to reduce the power draw, giving a duty cycle of 50%. The magnetorquers operate 5 V and are set with a saturation current of 0.5 A, thus they consume up to 2.5 W during operation.

The internal MOSFETs of the H-Bridge cause inefficiencies, and their resistance of 280 mΩ yields a 94.4% efficiency at 2.5 A and 5 V operating limit, however, this inefficiency is considered to be included in the power consumption of the magnetorquers, so it is ignored from the power budget table,

The sun sensors (photodiodes) operating at a voltage of 3.3 V consume < 1 mW of power.

Table 31: ADCS Component Power Usage Across Modes of Operation

Component	#	Power (W)	Mode (Duty Cycle %)			
			Safe	Nominal	Detumbling	Pointing
IMU	1	0.046	50	100	100	100
Magnetorquers	3	2.5	0	0	100	100
H-Bridge	3	0	0	0	100	100
Sun Sensors	5	<0.001	100	100	100	100

6.5.5 Comms Power Consumption

The VHF/UHF transceiver module consumes up to 2.2 W during max power TX, and considerably less during RX, with almost no power consumed during idle behaviour. Exact figures for RX and idle were not given in the datasheet, so a low power duty cycle of 5% was assumed. The antenna itself is a passive component and thus does not consume any power.

Table 32: Comms Component Power Usage Across Modes of Operation

Component	#	Power (W)	Mode (Duty Cycle %)		
			Safe	Nominal	TRX
UHF Antenna	1	0	0	0	0
VHF/UHF Transceiver	1	2.2	5	5	75



6.5.6 Payload Power Consumption

The payload spectrometer consumes power only during the Payload mode of operation. At a nominal voltage of 3.3 V with current draw of up to 100 mA depending on the LED illumination level. As a worst case, we assume the power draw is $3.3 \times 0.1 = 0.33$ W

Table 33: Comms Component Power Usage Across Modes of Operation

Component	#	Power (W)	Mode (Duty Cycle %)
			Payload
Sparkfun Spectrometer	1	0.33	100



7 On-Board Computer and On-Board Data Handling Subsystem

7.1 Overview

In this section, the PCB design for LUNATICS-0 as well as the OBC components that we have selected to interface with all parts of the PCB will be described.

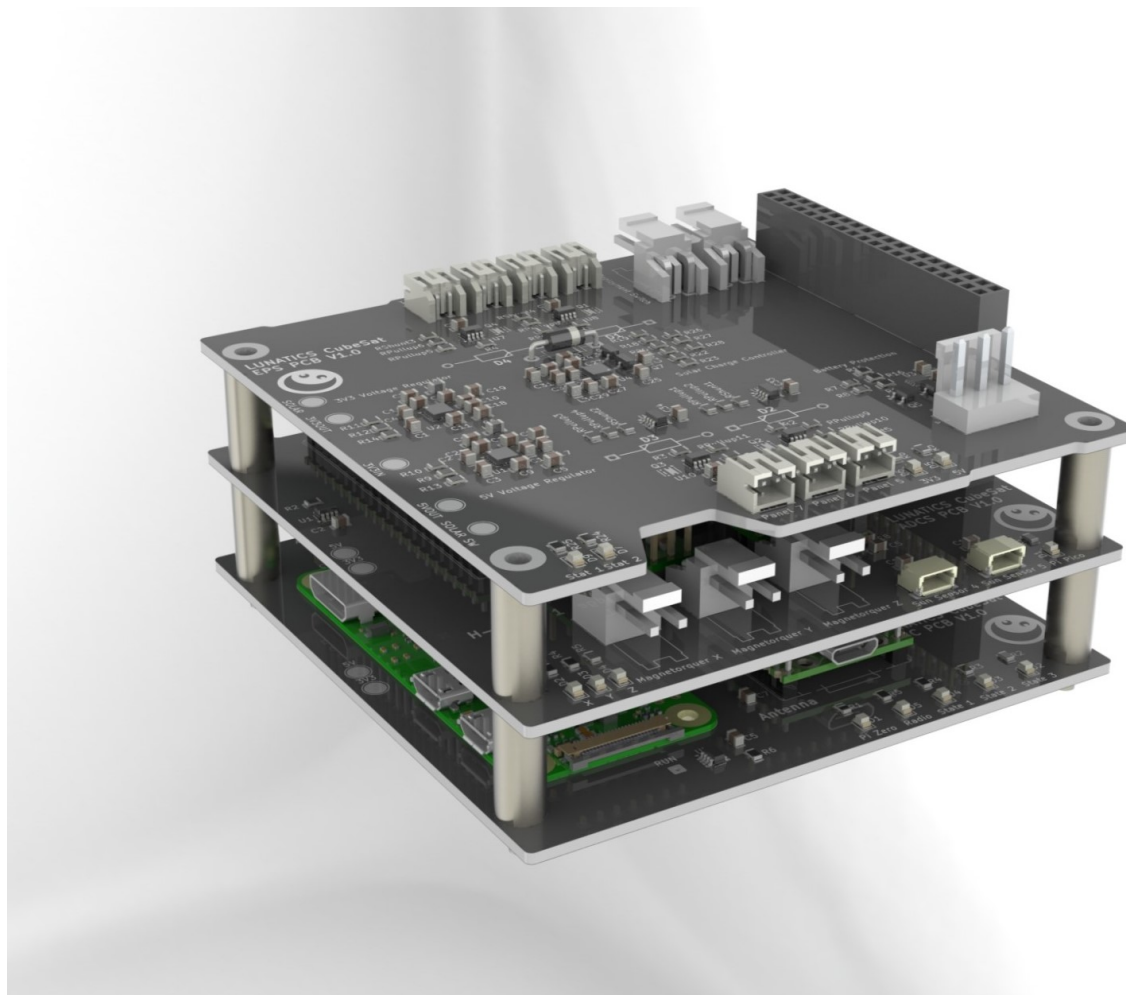


Figure 84: PCB Stack

7.2 PCB Design

7.2.1 PCB Dimensions

For the dimensioning of the PCB, a modified version of the PC/104 specification is utilised with a header bus consisting of 40 pins. In order to fit the PCB within the CubeSat structure, the board size is reduced to 90.17 mm x 90 mm. The specifications of component heights, the header heights and the spacing between the boards in the stack are all according to the standard.

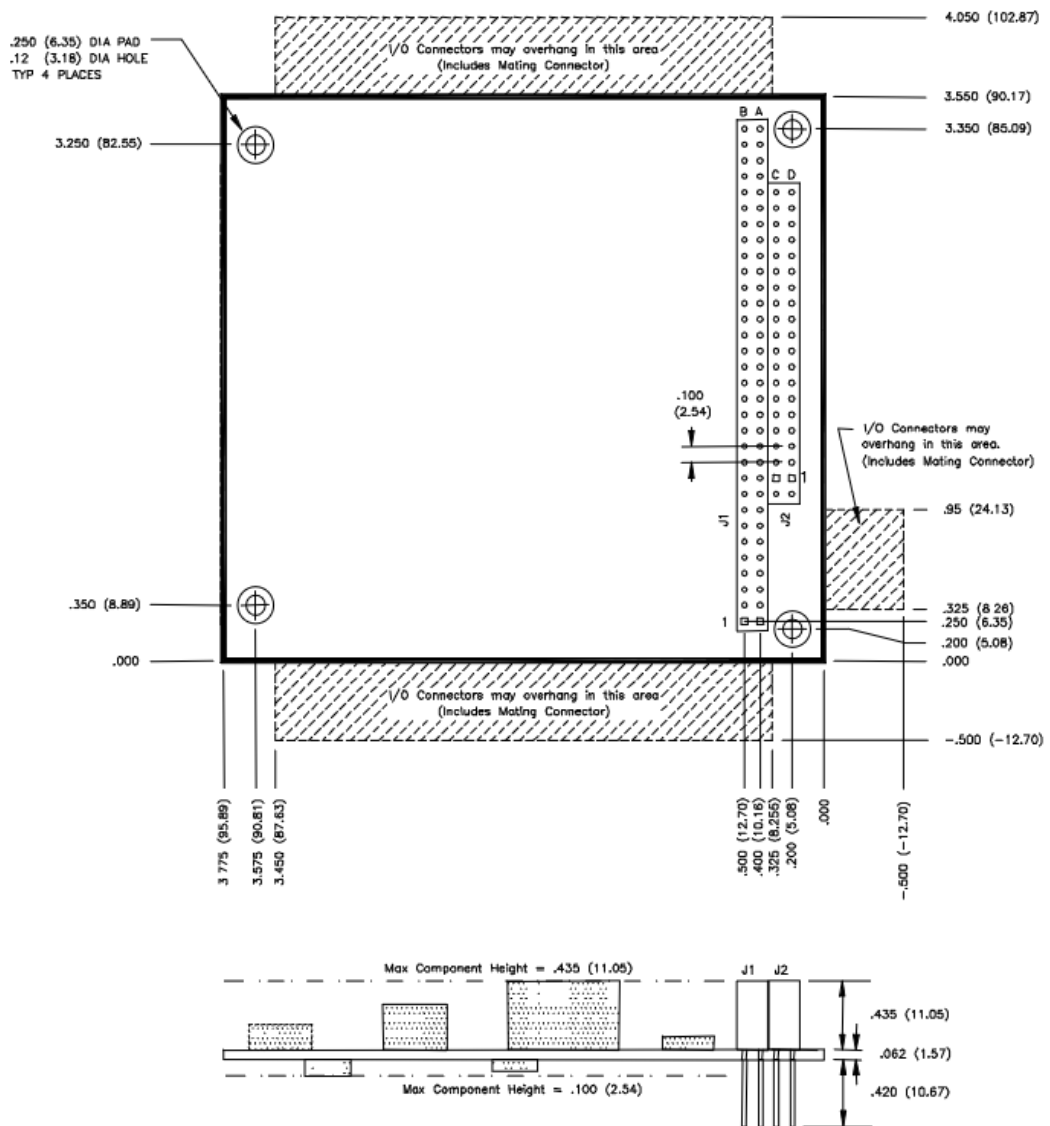


Figure 85: PC/104 Outline Dimensions [6]

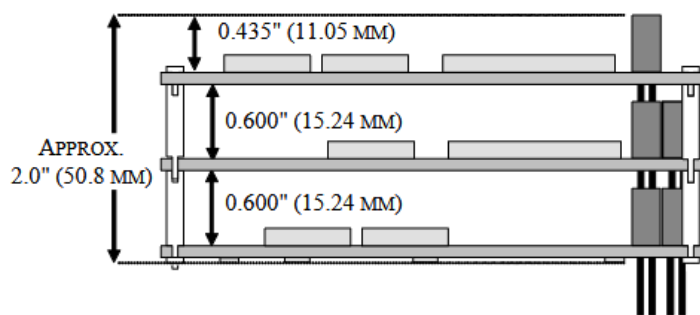


Figure 86: PC/104 Stack Dimensions [6]

7.2.2 PCB Stack

The PCB stack consists of 3 boards, which each serve a distinct purpose.

The top board is the EPS board which contains all of the circuitry associated with regulating the on-board power as well as interfacing with the solar panels and the battery.

The middle board is the ADCS board which contains all of the relevant circuitry for managing the ADCS system such as the h-bridges and outputs for the magnetorquers, the IMU, the RPP2W and the connectors for the sun sensors.

The bottom board contains the RP02W as well as the antenna, the payload interface and the RTC.

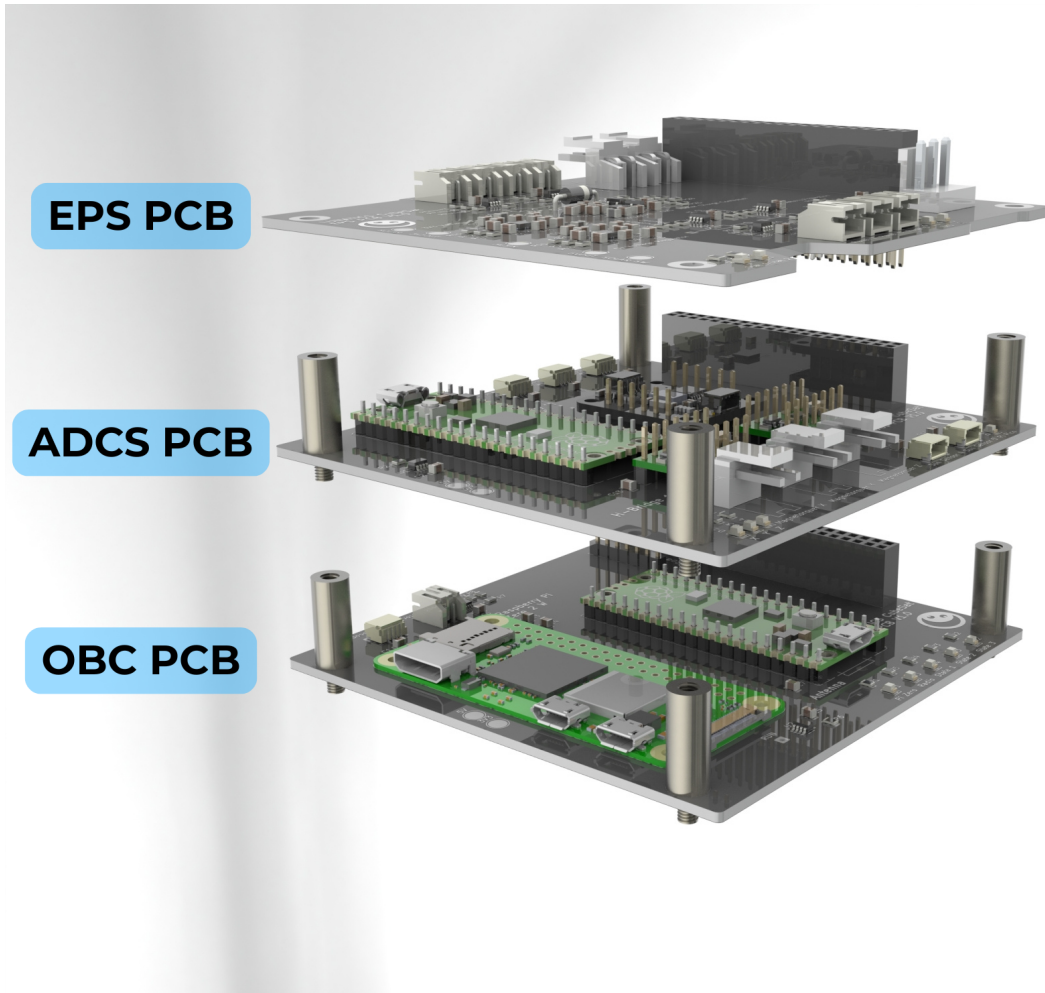


Figure 87: PCB Stack Diagram

7.2.3 Trace Width

To ensure that the traces on the PCB can safely carry the current on-board without excessive heating, the required trace width can be calculated using the IPC-2221 standard [29]. For this PCB there is a limit of 10°C for the temperature rise of traces.

The formulas for the cross-sectional area A_t and width of external PCB traces W are:

$$A_t = \left(\frac{I}{k \cdot (\Delta T)^b} \right)^{1/c} \quad (7.1)$$

$$W = \frac{A_t}{t \cdot 1.378} \quad (7.2)$$

Where k , b and c are empirically derived constants. For external layers on a PCB, $k = 0.048$, $b = 0.44$ and $c = 0.725$. For the manufacturing of this PCB, the thickness t of the traces is 1 oz.

The highest expected current on the PCB is from the battery, where the current may reach up to 2A. Therefore, the required trace width for these traces is 0.7814 mm. Other typical currents we can expect to see are 0.5A from the solar panels and less than 0.1A for typical signals. The required trace widths for these are 0.1154mm and 0.0125mm respectively. Therefore for the routing of the boards a trace width of 0.8mm will be used for traces carrying power from the battery. The minimum trace width for every other signal is 0.3mm, however larger traces will be favoured where possible to reduce impedance.

7.2.4 PCB and Structural Grounding

To reduce electromagnetic interference and provide a low-impedance return path for current, a ground plane is included on the bottom side of each PCB. This also minimises ground loops and supports stable voltage references to ensure that signals are reliable and low noise. The capacitance of this ground plane can be calculated with the following equation:

$$C = \varepsilon_r \varepsilon_0 \frac{A_p}{d_p} \quad (7.3)$$

Where $\varepsilon_r = 4.7$ for FR-4 [30], $\varepsilon_0 = 8.854 \times 10^{-12}$ F/m, $A \approx 8100 \text{ mm}^2$, and $d = 1.6 \text{ mm}$. Therefore the capacitance of the ground plane is 210.67 pF .

The structure is also connected to the ground of the PCB which will mean that accumulated electrostatic charge can be safely dissipated, reducing the risk of electrostatic discharge damage to components.

7.2.5 Connectors

Three key types of connectors are used on the PCB stack for interfacing with other components. Each of these connectors are non-reversible which ensures that the polarity of connectors may not be reversed during the assembly phase.

The largest connector used is the JST VH connector which is a locking connector that supports up to 18 AWG wire. This connector is used for the battery, the deployment switches and the magnetorquers which are high current, critical connections. These connectors are through hole for the highest reliability.

JST PH connectors are used for the solar panels and the thermistor. This connection was chosen to keep consistency with the attached connector on the solar panels in use, reducing the amount of required custom cable creation. These connectors are also through hole.

Finally, JST SH connectors are used for the spectroscopy sensor and the sun sensors to match the header on the boards of these sensors. This reduces the complexity of the wiring and ensures it is easy to obtain suitable wires.



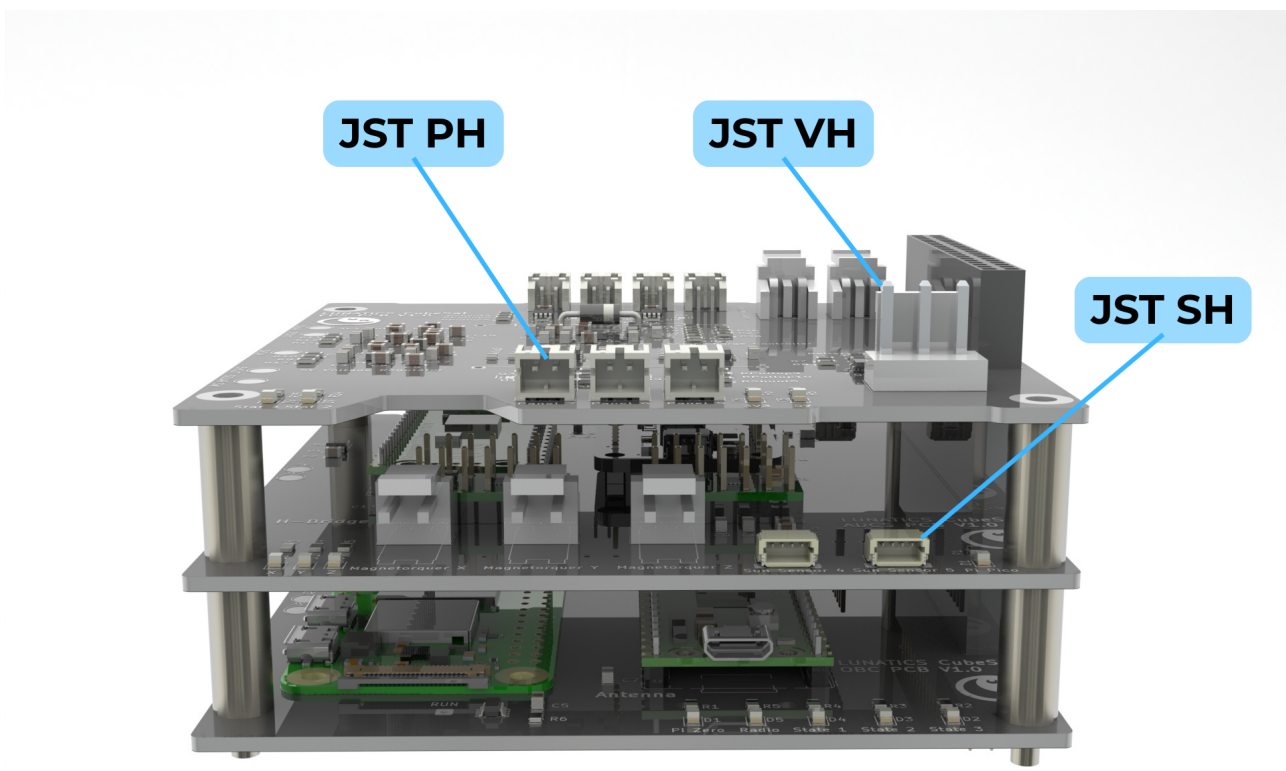


Figure 88: PCB Connector Types

7.2.6 Design For Assembly

In order to ease the process of assembly, cutouts were included on the edge of the upper boards in the stack. These will allow the cables connecting to the lower boards through, ensuring a simple assembly process.

To further ease the assembly process, every connector on the board is non-reversible, and is labelled with the component that it should be connected to.

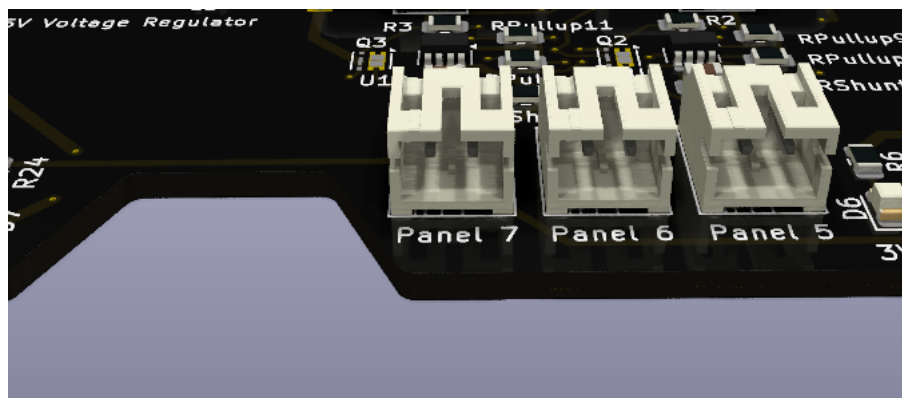


Figure 89: Labelled Connector and Cable Cut-out

7.2.7 Design For Debugging

For easy debugging and testing, two key features were included in the PCB, LED indicators and testing pads. The testing pads provide a simple way to measure the voltage and check for nominal operation.

The LEDs indicate 5V power, 3.3V power, the heartbeat for each Raspberry Pi for the watchdog, the state of the radio and the state of each magnetorquer. Furthermore, through encoding the state of the satellite in binary, the state is represented with 3 LEDs. The inclusion of these indicators provides an easy way to ensure that software is behaving as expected and that operation of the board is nominal.

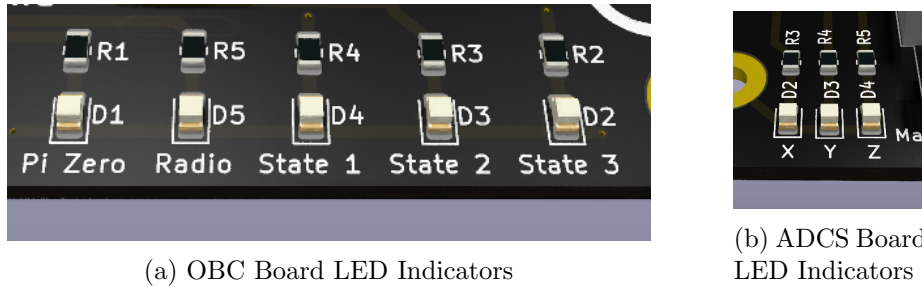


Figure 90: LED Indicators On PCB

7.2.8 PCB Component Placement and Routing

When positioning the components on each board before routing, the components were grouped according to the schematic. This simplifies the routing as any connections within the group are confined, and it also helps to organise the board. When placing components, priority was put on the decoupling capacitors for each Integrated Circuit (IC) such that they were as close as possible. This ensures that they are effective at preventing noise from affecting the IC. When routing, priority was placed on any ICs with many pads for example the I₂C multiplexer on the ADCS board. Many vias were used to connect to the ground plane, ensuring that the path to ground was always as short as possible.

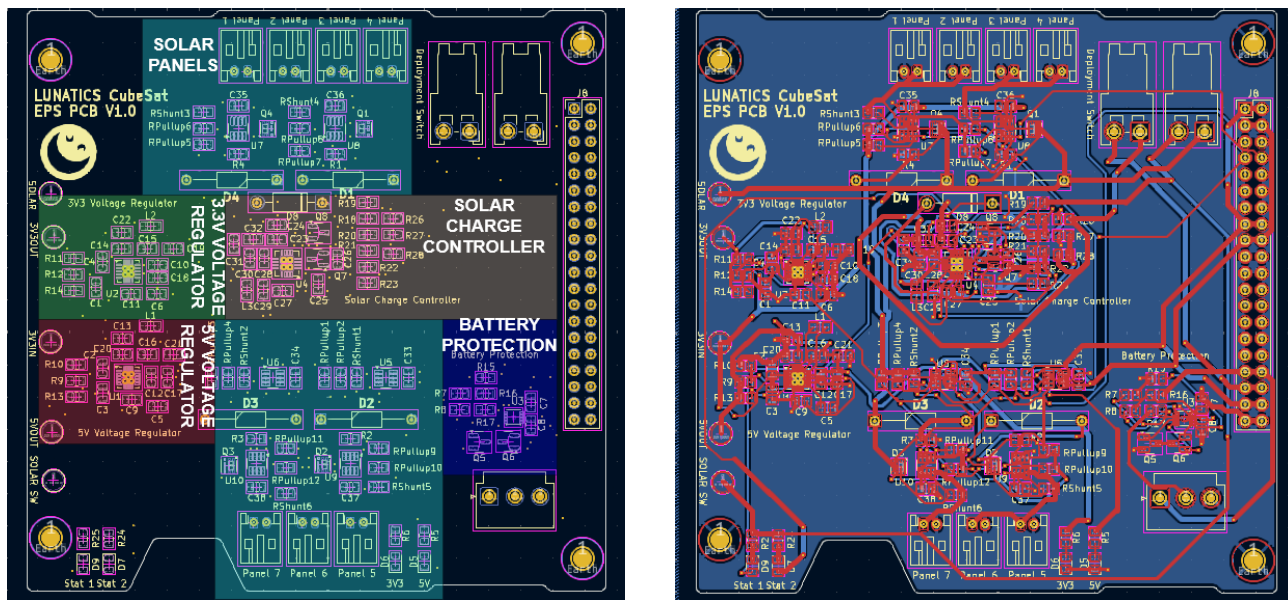
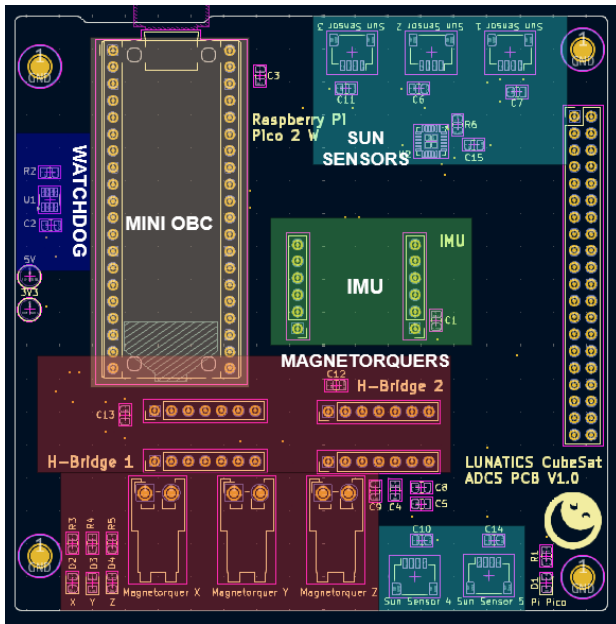
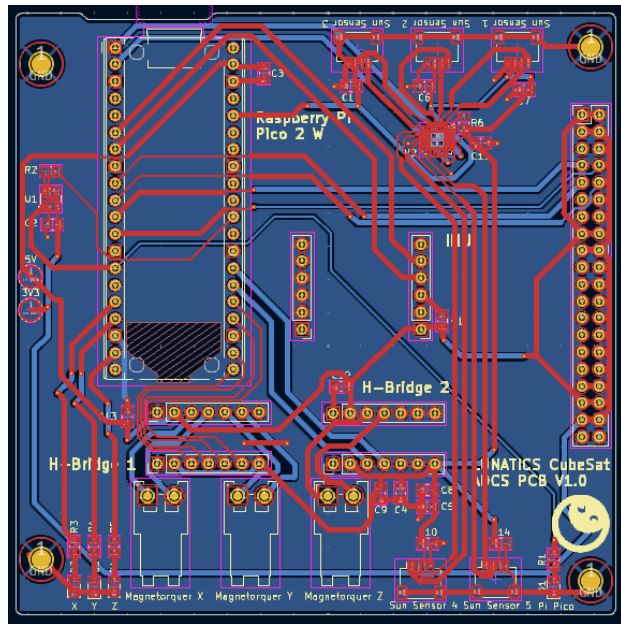


Figure 91: EPS PCB

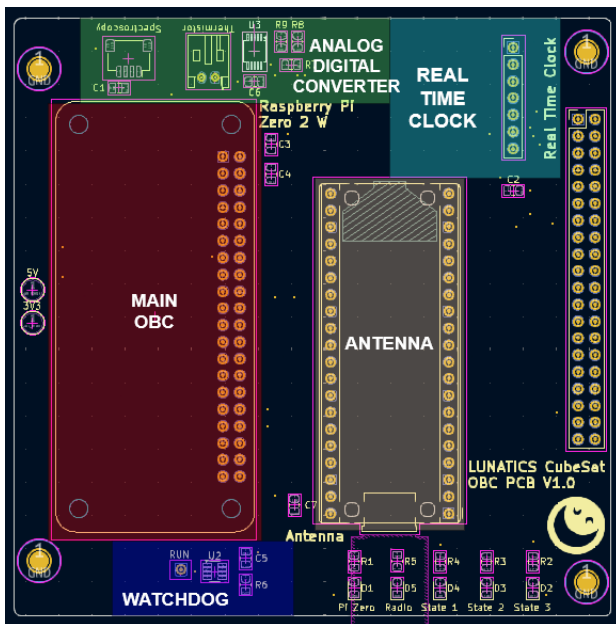


(a) ADCS PCB Component Placement

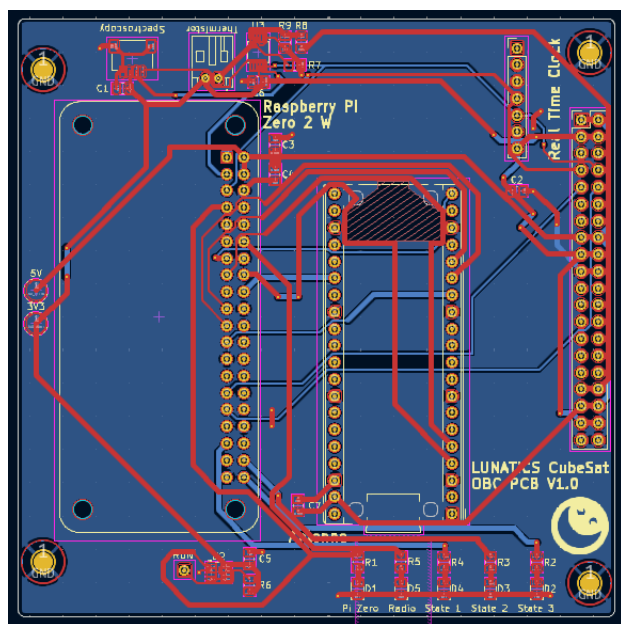


(b) ADCS PCB Routing

Figure 92: ADCS PCB



(a) OBC PCB Component Placement



(b) OBC PCB Routing

Figure 93: OBC PCB

7.2.9 Conformal Coating

After manufacturing, the PCBs will have a layer of conformal coating applied as this is a protective measure which can help to increase the reliability of the PCB throughout the mission. Conformal coating is generally required for PCBs in space missions, for example, NASA standard NASA-STD-8739.1 [31] states that conformal coating is required for PCBs.

Conformal coating forms a thin, non-conductive layer over the entire PCB, shielding it from environmental contaminants, condensation during launch, and ionic residues left over from manufacturing. This layer significantly reduces the risk of corrosion, moisture absorption, and

electrical arcing between closely spaced conductors in a vacuum.

Additionally, conformal coating improves mechanical integrity by reinforcing solder joints and components against high-frequency vibrations and mechanical shocks during launch.

7.3 OBC Components

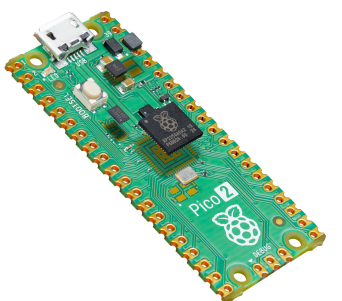
7.3.1 Main Board and Mini Board

The onboard computer that has been selected is the Raspberry Pi Zero 2 W (RP02W), provided by Raspberry Pi. This board has 40 pins of GPIO which is sufficient to communicate with the required peripherals, and features a quad-core 64-bit ARM Cortex-A53 processor clocked at 1GHz with 512MB of SDRAM. The RP02W will run the Raspberry Pi OS, a Linux-based operating system optimized for the Raspberry Pi family of single-board computers with ROS2 (Humble) running as the middleware. As the RP02W is lightweight, we will be using a distro of ROS2 `humble-base`, which does not contain all the overhead of ROS such as Gazebo.

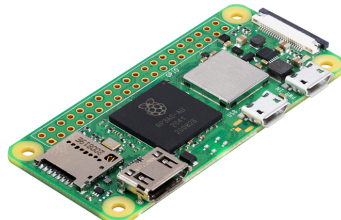
This OBC will do the following tasks onboard LUNATICS-0:

1. Maintain the state of LUNATICS-0. It will be responsible to know what state the satellite is in, as well as be responsible for making all the peripheral changes required when passing through the states. For example if A represents the set of sensors/actuators needed in the first state and B the same for the second state, the OBC will turn *off* any peripherals in $A \setminus B$ and will turn *on* any in $B \setminus A$
2. Manage communications with the ground station. The OBC is directly connected to the TT&C system, and thus will be responsible for sending WOD, as well as downstreaming all the payload data when required. It will also react to any change of state that is sent from the uplink.
3. Finally, it will also be responsible for taking readings from the payload, and storing it in memory when not in view of the ground station.

The OBC is connected to a Raspberry Pi Pico 2 W (RPP2W), also supplied by Raspberry Pi. This micro-controller will be responsible for all the attitude control and determination onboard LUNATICS-0. It will be connected to the 5 sun sensors, the IMU, as well as the H-Bridges that will control the Magnetorquer. A separate controller for ADCS is essential for effectiveness of our ADCS algorithms and control, as increased latency could cause instability in the system.



(a) Raspberry Pi Pico 2 W



(b) Raspberry Pi Zero 2 W

Figure 94: Main OBC and ADCS Microcontroller selection

Both of these devices have been used before in experimental projects such as other CubeSats, however lack proper radiation testing and long-term reliability in space. They each have a Technology Readiness Level (TRL) of 5, with further testing and use in commercial products required for a higher TRL.



7.3.2 Watchdog

For monitoring the health of the OBC, a watchdog is implemented that ensures both the main and the mini board are operating. Figure 95 displays typical operation of this watchdog.

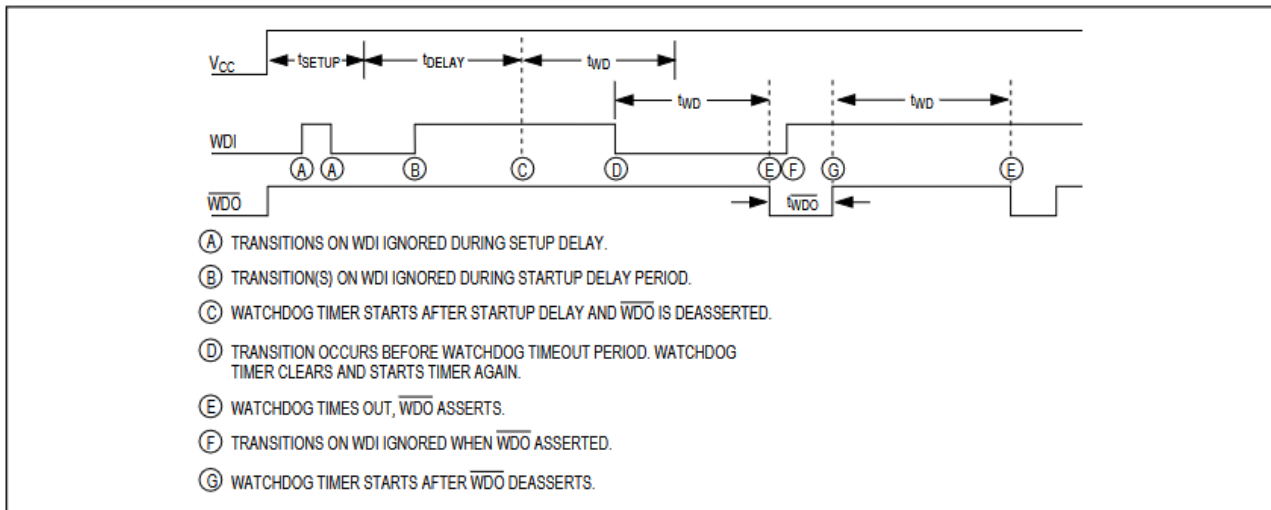


Figure 95: Watchdog Operation [7]

For this OBC, t_{DELAY} is set to 60 seconds to ensure that the OBC has time to start up before monitoring begins. This prevents the possibility of a looping reset which results in the OBC never reaching operation. Furthermore, t_{WD} is set at 60 seconds to reduce the number of pulses required from the main and mini OBC, reducing power consumption. Each board will be sending a heartbeat pulse through GPIO every 10 seconds.

7.3.3 Real Time Clock

To maintain clock accuracy of 500ms during science operations according to S-OBC-04, a Real Time Clock (RTC) is implemented that has a drift rate of $\pm 0.432 \text{ s/day}$. When the CubeSat is communicating with the ground station, a packet will be uplinked to update the clock and ensure it remains within the timing tolerance.



Figure 96: DS3231 MEMS Precise RTC [8]

7.3.4 Analog to Digital Converter

To measure the voltage of the battery as well as its temperature, a 12-bit analog to digital converter was implemented, as there is no built-in converter in the RP02W. This converter communicates

through I²C with the RP02W. The ADS1015 IC was chosen for this as it is readily available for assembly by the manufacturer of the PCB.

7.3.5 I²C Multiplexer

The sun sensors that are used in the ADCS system have only a single option for their I²C address. Therefore, to ensure communication is possible with each sensor, a double throw multiplexer is implemented which will switch which sensor is sending data on the I²C bus.

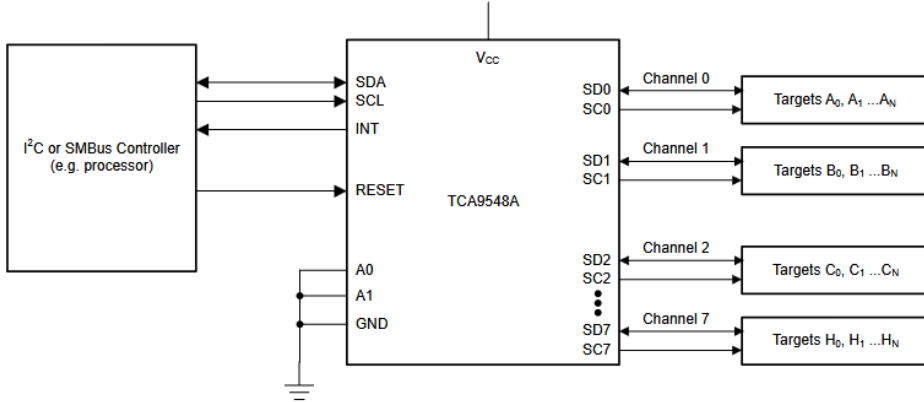


Figure 97: I²C Multiplexer Diagram [9]

7.4 OBC Validation

As validation, a headless setup of the RP02W was made, where after the SD card was flashed with the OS, from the local computer terminal one could directly `ssh` into the device and run all setup code over WiFi. This headless development will ensure that it is easy to work on software onboard the PCB throughout the complete assembly of LUNATICS-0.

After the setup of the RP02W, Docker was installed and using a command (`docker pull ros:humble-ros-base`), a premade docker container was pulled with all the ROS2 dependencies complete. A simple publisher/listener setup was created, seen in Figure 98b. Here, two nodes were created (`talker` and a `listener`) which successfully communicated with each other from two separate terminals.

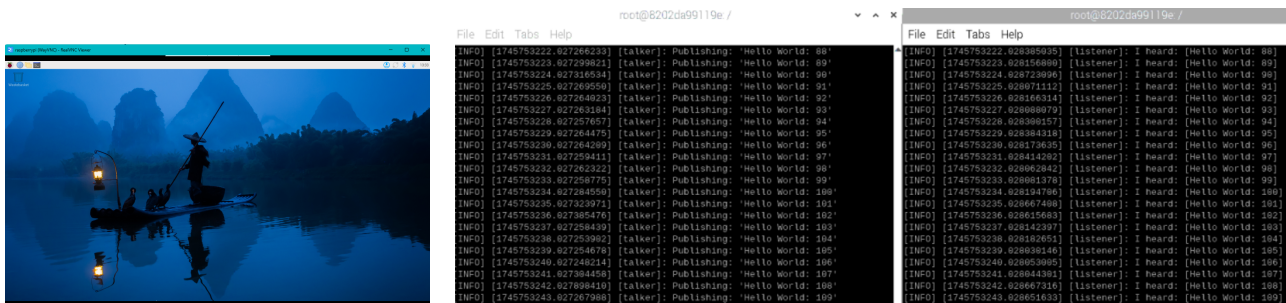


Figure 98: Main OBC and ADCS Microcontroller selection

With this validation complete, we can define the publishers and subscribers for the *whole* system so we can understand how each package will interact. In general, for each sensor/actuator, we will have a node that will manage any subscriptions to get input data, or publishers to output information to the rest of the system. In Figure 99, the FSM is the main node, with its subscriptions to both the

logs from ground and the EPS system determining the state (`curr_state`) of the satellite. This state is then passed to the attitude (a module for communicating with the RPP2W over GPIO) and the spectroscope. The FSM also passes both the WOD data and payload data so that the satellite can transmit the data when required.

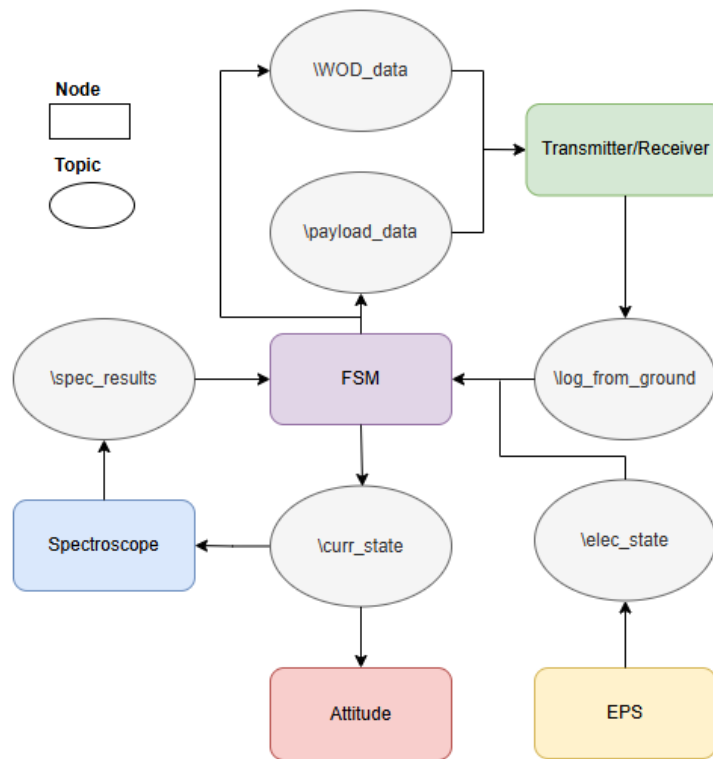


Figure 99: ROS Topics - this is how software modules communicate with each other. In this diagram, an arrow leaving a node means it is publishing and an arrow entering a node means it is subscribing.

7.5 Bus Connections

The OBC and the ACDS microcontroller will be connected to their peripherals as described in Figure 100. I2C will be the main protocol across the whole system due to being more simple and economic than other protocols such as SPI and UART, as only two wires are required for communication to work with multiple devices.

I2C communicates with its target device using packets with a unique address for that device - of which is mentioned in Figure 100 where applicable. In some cases, such as the sun sensors for the RPP2W, only one address can be outputted from the device, meaning a multiplexer was included within our design to organise communication with these sensors.

One of the issues with I2C is a stuck bus - when the SDA line gets held low indefinitely while the SCL line is high. This presents a problem because typically there are multiple I2C devices on the bus and if the SDA line were to get stuck low, then I2C communication can no longer be possible. In order to provide error handling for a stuck bus, we will use both well defined timeouts for our packet requests in the software as well as the watchdog which will reset the boards if no signal is received for 60s. This ensures that the communication bus remains functioning as desired.

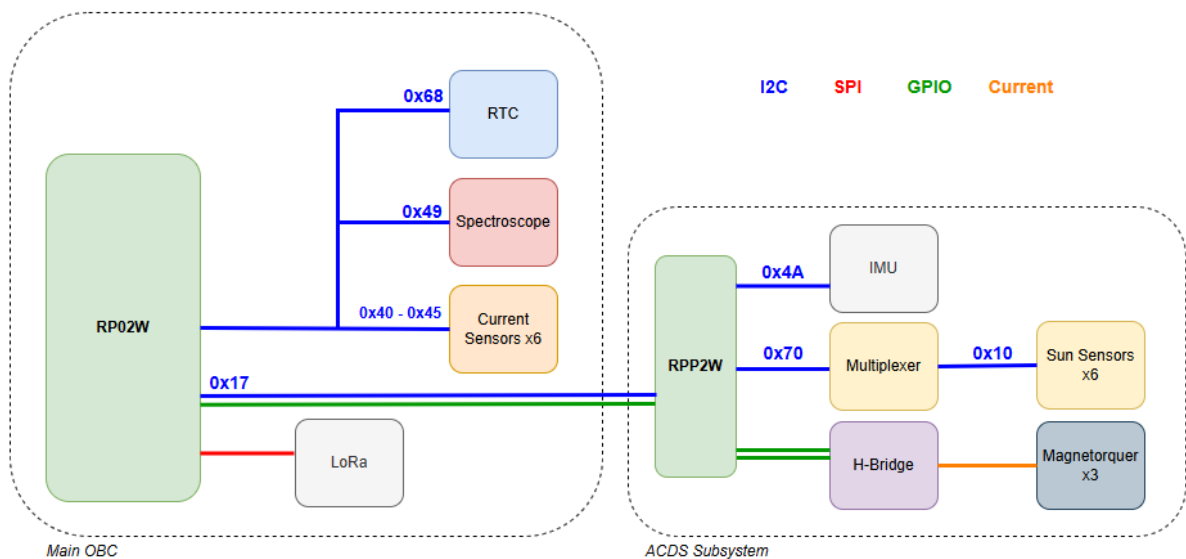


Figure 100: Communication Protocols used within LUNATICS-0

7.6 Modes of Operation

The modes of operations of the whole satellite are detailed in Figure 101. It is the OBC's responsibilities at all parts of the flight to coordinate the transitions between each of these states. In summary, we begin from the launch state where we then initialise all the modules and begin detumbling - which should last less than 2 days. We then sit in a nominal mode until we are required to transition between sending transmissions, storing payload data, and requesting attitude adjustments. At any point, the battery levels can force the OBC to turn off everything and recharge the batteries, before resuming again in nominal mode for normal operations. Based on the DoD referenced in 6, anytime the battery is below 80% charge the satellite will enter a 'safe' mode, which it will only exit once back at 100% charge.

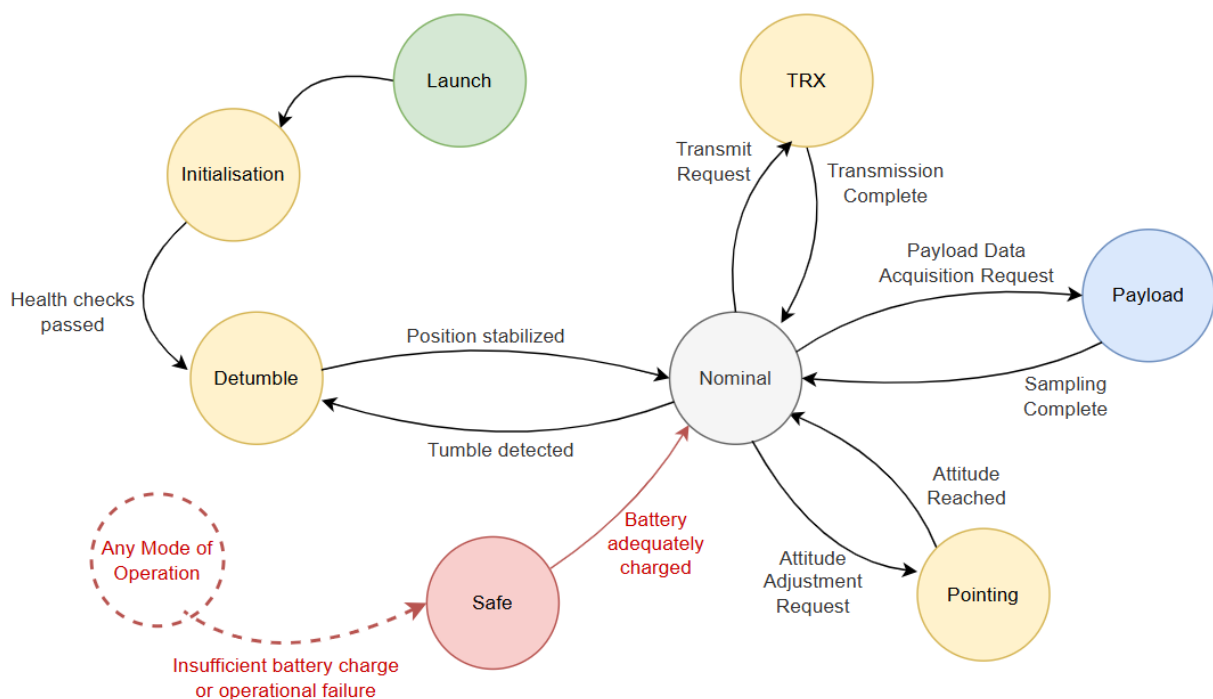


Figure 101: State Machine, showing the modes of operations

7.7 Code Structure

In order to design the system used within LUNATICS-0, the following pseudo code will be implemented in much greater detail within our OBC. It is assumed that this code begins running after the initialisation state in 101.

```
def main():
    current_state = 0
    time_counter = 0 # (s)
    while True:
        # state transition from detumbling to nominal
        if current_state == 0:
            if not is_detumbling():
                current_state = 1
                start_nadir_pointing()

        # nominal state, check battery
        if current_state == 1:
            battery_perc = get_battery_level_perc()
            if battery_perc <= 0.8:
                current_state = 2
                turn_everything_off()

        # safe state, check battery
        if current_state == 2:
            battery_perc = get_battery_level_perc()
            if battery_perc == 1.0:
                current_state = 1
                turn_everything_on()
            else:
                continue

        comms_visible = is_comms_available()

        # send state so that ADCS knows
        send_current_state(current_state)

        if time_counter > 25:
            time_counter = 0
            send_comms(WOD) # send whether in view or not

        if comms_visible:
            send_payload_data()
        else:
            payload_data = get_payload_data()
            save_payload_data(payload_data)
```

Furthermore, we can also write pseudocode for the RPP2W as well. This code holds its own smaller state machine that changes state depending on the OBC. If a state change is detected it turns on/off all peripherals related to the ADCS subsystem. It also then reads from the sensors, calculates the required torques from our control system and then uses the actuators to deliver those torques. This pseudo code abstracts a lot of detailed algorithms in place (such as filtering the sensor data, control algorithm), giving us a high-level insight into the structure of the code.



```

def main():
    # dictionary of all the sensors/actuators for each mode
    mode_sets = {
        0: {...}, # mode 0: idle
        1: {...}, # mode 1: detumbling
        2: {...}, # mode 2: nadir pointing
    }

    prev_mode = 0
    mode = 0
    while True:
        mode = detect_mode_change()
        if mode != prev_mode: # change of state
            for peripheral in mode_sets[mode] \ mode_sets[prev_mode]:
                turn_on(peripheral)
            for peripheral in mode_sets[prev_mode] \ mode_sets[mode]:
                turn_off(peripheral)
        prev_mode = mode
        delay(2)

        if mode == 1:
            pointing = get_reading()
            torques_required = detumbling_algorithm(pointing)
            use_actuators(torques_required)
        if mode == 2:
            pointing, nadir_vector = get_reading_and_nadir()
            torques_required = nadir_pointing(pointing, nadir_vector)
            use_actuators(torques_required)

```

7.8 Data Budget

Our system requirement S-TTC-03 make us follow the AX.25 Protocol [14], meaning we have an upper bound bit rate R_B of 9.6 kbps. We are also required to include headers and error checking in each packet (See Appendix B.6 for the Frame Check Sequence (FCS) algorithm used for error checking). For each packet we send a total of 332 bytes, divided into 256 data bytes and 76 extra information bytes for these checks (see Table 34). This translates to a data rate R_D of roughly 7.4 kbps ($R_b \cdot \frac{256}{332}$).

Table 34: AX.25 UI-Frame Format [14]

Field	Size (Bytes)
Flag	1
Destination Address	7
Source Address	7
Digipeater Addresses (0-8)	0-56
Control Field (UI)	1
Protocol ID	1
Information Field	1-256
FCS (Frame Check Sequence)	2
Flag	1



7.8.1 Uplink Data

For the uplink data, there are two types of flags we will implement. The first 0x48 (H in hexadecimal) will be a heartbeat check. This will be sent to establish a connection with the CubeSat, allowing it to understand that it can now send the information that it has been storing. The Heartbeat data of the CubeSat is presented in Table 35.

Table 35: Heartbeat Data

Field	Size (Bytes)
Padding	256

The second will be 0x4F (O in hexadecimal) which will be a manual override of the state that the CubeSat is in (Table 36). The data in the packets will hold the state for the CubeSat should change to.

Table 36: Override Data

Field	Size (Bytes)
New State	1
Padding	255

7.8.2 Downlink Data

The downlink also has two types of packets that it will send down to the ground station. The first is defined by the 0x54 flag (T in hexadecimal), which will include the Whole Orbit Data. By the system requirement S-TTC-02, the CubeSat is required to send this at least every 30s.

Table 37: Single WOD reading

Parameter	Size (bits)
Mode	1
Battery voltage	8
Battery current	8
3V3 bus current	8
5V bus current	8
Temperature Comm	8
Temperature EPS	8
Temperature Battery	8
<i>Total</i>	57

By Whole Orbit Data (WOD) requirements [32], a reading in the structure found in Table 37 will be recorded at a frequency of 1/60 Hz (once per minute) and will store the last 32 minutes of recording data on the OBC (S-OBC-02).



Table 38: Whole Orbit Data Packet structure

Parameter	Size (bits)
Time	32
Data set 1	57
Data set 2	57
...	1653
Data set 32	57
<i>Total</i>	1856

Table 38 shows the full structure that will be downlinked every 30s. This requirement means that even if LUNATICS-0 is not in view of the ground station, other ground stations through its orbit have the potential to read its WOD status. To note, the **Time** parameter represents the time of the *first* recording. This fits in the AX.25 data in the following way (see Table 39):

Table 39: WOD Data for Ax.25 frame

Field	Size (Bytes)
Whole Orbit Data Packet	232
Padding	24

The final packet type will include the science data that the CubeSat has stored over the course of the orbit that it is not in view of the ground station. See Appendix B.7 for more information on ensuring that we have enough storage to allow this. We will use the 0x53 (S in Hexidecimal) flag for this packet type.

Table 40: Science Structure

Field	Size (Bytes)
High Bytes	18
Low Bytes	18
Timestamp	4
<i>Total</i>	40

Table 40 breaks down each recording that we will do with our Triad Spectroscopy Sensor. To note, the sensor is made up of 18 channels that each have a high and low byte to represent their reading. The final packet for the science data is shown in Table 41.

Table 41: Science Data

Field	Size (Bytes)
Science Structure × 6	240
Padding	16



8 Communication Subsystem

8.1 General Information

The modulation type that has been selected is Binary Phase-Shift Keying (BPSK). This is a modulation technique where the carrier signal's phase is altered by 180 degrees for each symbol - where a shift of 180 degrees represents a zero whilst no shift represents a one. BPSK is simple, efficient and noise resistant, making it a perfect choice for our communication module.

For both the uplink and the downlink systems, we will transmit at 400 Mhz, within the UHF-band of frequencies. As LUNATICS-0 is operating in LEO and a low data rate is sufficient, 400 Mhz ensures that the signal is very robust to noise compared to higher frequencies. Both the uplink and downlink components that have been selected support this frequency, as well as the BPSK modulation from above.

Finally, we will follow the AX.25 protocol for the transmission of our data following requirement S-TTC-02. The implications for this requirement on the communication system is that it recommends using a 9.6 kbps bit rate for transmission, and requires the use of a frame around the data in order to handle error checking, transmission types, and a level of robustness.

8.2 Uplink

The ground station that has been selected for our uplink operations is the in-house University of Sydney's ground station on top of the JO3 building. This station is located in Sydney Australia, and is currently active in communicating with CUAVA-2 [33], meaning it is TRL 9.

This ground station has been selected not just due to its location and ease of use with the LUNATIC team, but also its combatability with the orbit that we have selected. As the orbit is near polar and sun-synchronous, the ground station is in view of the satellite at least once a day for a few minutes (see data budget for more details), ensuring the payload data is regularly streamed down to earth and processed. Figure 102 shows the ground station and when it is visible from the satellite over 5 days. The coordinates of the ground station are 33.8852° S, 151.1801° E.

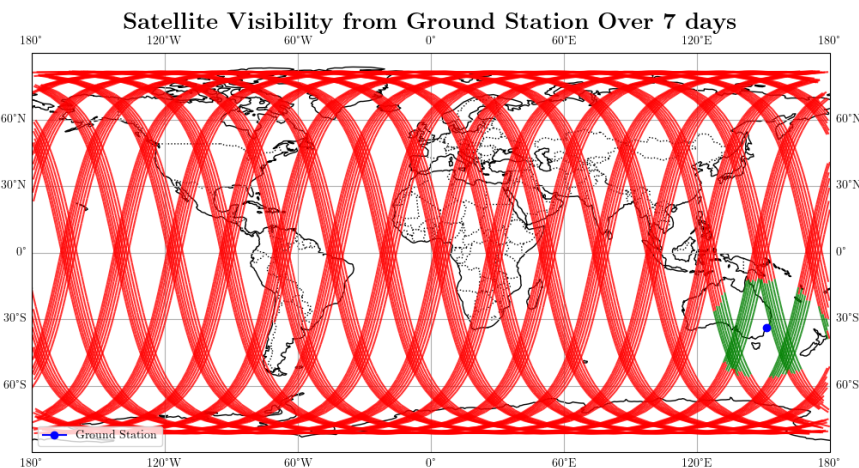


Figure 102: Ground trace showing the visibility of the satellite from the ground station. Green and Red traces are used to represent in view and not in view respectively

The ground station antenna is a Crossed Yagi design that operates at 437.075 MHz (UHF). The antenna supports BPSK modulation and has a baud rate of 9600, satisfying our requirements.



8.3 Downlink

The downlink system consists of the NanoComm AX100UL modem connected to the NanoComm ANT430 omni directional antenna, both provided by Gomspace. Both of these parts are TRL 9, providing robust UHF communication in LEO. The ANT430 antenna has a frequency range from 430-440Mhz, fitting within our requirements.

Gomspace have designed both of these parts to seamlessly integrate into a 2U cubesat structure. Their provided datasheet shows how to connect it to the frame of the satellite, shown in Figure 103.

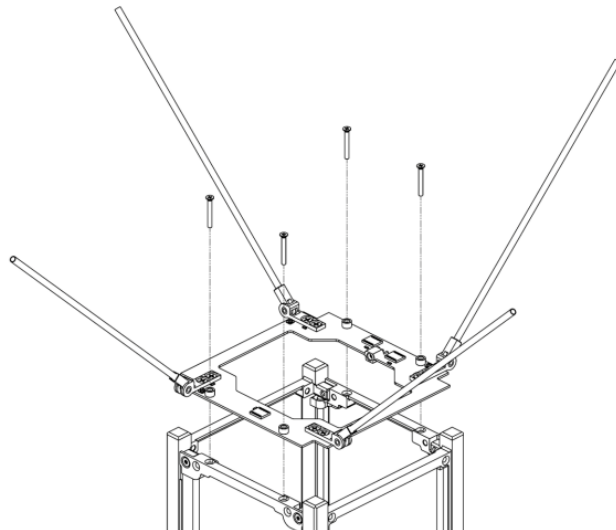


Figure 103: Assembly instructions from Gomspace for the ANT430 Antenna

For the Cubesat that we are developing, we will not be making the screw holes and connections required to fit the ANT430, however modification to our design is possible to accommodate for the custom fitting.

8.4 Testing

In order to simulate the ground station and the transmission of data, LoRa will be used as both the uplink and downlink parts of our system. LoRa allows us to communicate using the internet over distances of roughly 20km in urban areas and offers the closest emulation to our real life space communication as possible.

The part selected is the SX1262 LoRa Node Module for Raspberry Pi Pico, which seamlessly interfaces with a Raspberry Pi Pico to send and receive data from the Internet of Things network. Due to Australian standards, the module will transmit and receive at frequencies of around 928Mhz, still within the UHF band.

As a redundancy, testing using the in built WiFi support of our Raspberry Pi Zero 2 W is another potential option due to the compatibility with our OBC. Initial testing showed that this was quite easy to implement - with validation performed by connecting to a TCP server (on a local computer) created using the python Flask library. When on the same WiFi, a socket can be created on the host computer which the RP02W can access and send information. In Figure 104, CPU temperatures were sent over this connection and displayed on a live frontend.

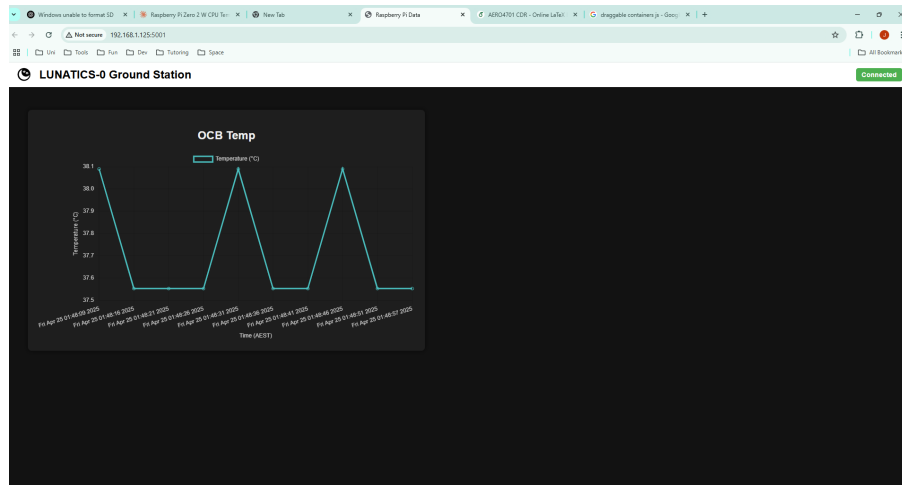


Figure 104: Testing the RP02W, communicating using TCP sockets

This front end will be expanded to display much more onboard information, such as the current state of the satellite, payload data, and more temperature information.

8.5 Link Budgets

The link budget has been created on the Annex Spreadsheet for both the uplink and the downlink parts of the system using the AMSAT-IARU Link Model. As a summary the following results were found:

8.5.1 Uplink

Parameter	Value	Units
Ground Station		
Ground Station Transmitter Power Output	150.0	watts
In dBW	21.8	dBW
In dBm	51.8	dBm
Ground Station Total Transmission Line Losses	3.6	dB
Antenna Gain	16.3	dBi
Ground Station EIRP	34.4	dBW
Uplink Path		
Ground Station Antenna Pointing Loss	0.3	dB
Ground-to-S/C Antenna Polarization Losses	0.1	dB
Path Loss	152.2	dB
Atmospheric Losses	2.1	dB
Ionospheric Losses	0.4	dB
Rain Losses	0.0	dB
Isotropic Signal Level at Spacecraft	-120.6	dBW
Spacecraft (Eb/No Method)		
Spacecraft Antenna Pointing Loss	0.3	dB
Spacecraft Antenna Gain	2.0	dBi
Spacecraft Total Transmission Line Losses	2.0	dB
Spacecraft Effective Noise Temperature	261	K
Spacecraft Figure of Merit (G/T)	-24.1	dB/K
S/C Signal-to-Noise Power Density (S/No)	83.5	dBHz
System Desired Data Rate	9600	bps
In dBHz	39.8	dBHz
Command System Eb/No	43.7	dB
Demodulation Method Selected	BPSK	
Forward Error Correction Coding Used	None	
System Allowed or Specified Bit-Error-Rate	1.0×10^{-6}	
Demodulator Implementation Loss	1.0	dB
Telemetry System Required Eb/No	10.5	dB
Eb/No Threshold	11.5	dB
System Link Margin	32.2	dB

Table 42: Uplink budget parameters for the CubeSat ground-to-spacecraft communication link.



8.5.2 Downlink

Parameter	Value	Units
Spacecraft		
Spacecraft Transmitter Power Output	2.0	watts
In dBW	3.0	dBW
In dBm	33.0	dBm
Spacecraft Total Transmission Line Losses	2.2	dB
Spacecraft Antenna Gain	2.0	dBi
Spacecraft EIRP	2.8	dBW
Downlink Path		
Spacecraft Antenna Pointing Loss	0.3	dB
S/C-to-Ground Antenna Polarization Loss	0.1	dB
Path Loss	152.2	dB
Atmospheric Loss	2.1	dB
Ionospheric Loss	0.4	dB
Rain Loss	0.0	dB
Isotropic Signal Level at Ground Station	-152.3	dBW
Ground Station (Eb/No Method)		
Ground Station Antenna Pointing Loss	0.2	dB
Ground Station Antenna Gain	14.1	dBi
Ground Station Total Transmission Line Losses	2.0	dB
Ground Station Effective Noise Temperature	510	K
Ground Station Figure of Merit (G/T)	-15.0	dB/K
G.S. Signal-to-Noise Power Density (S/No)	61.1	dBHz
System Desired Data Rate	9600	bps
In dBHz	39.8	dBHz
Telemetry System Eb/No for the Downlink	21.3	dB
Demodulation Method Selected	BPSK	
Forward Error Correction Coding Used	None	
System Allowed or Specified Bit-Error-Rate	1.0×10^{-5}	
Demodulator Implementation Loss	0.0	dB
Telemetry System Required Eb/No	9.6	dB
Eb/No Threshold	9.6	dB
System Link Margin	11.7	dB

Table 43: Downlink budget parameters for the CubeSat spacecraft-to-ground communication link.

As expected due to our low frequency, simple modulation scheme, and low altitude, we have a good margin on both the downlink and uplink parts of the system.

8.5.3 Link Budget Assumptions

EIRP (Equivalent Isotropic Radiated Power)

In order to calculate the EIRP value of the transmitter, we can simply apply the following formula.

$$EIRP = P_t + G_t - L_t$$

Free-Space Path Loss (FSPL)

The following formula gives the FSPL.

$$FSPL = 20\log_{10}\left(\frac{4\pi df}{c}\right) \text{ dB}$$



We take c as the speed of light (299,792,458 m/s) and the distance d as the maximum distance between the ground station and the satellite. As an upper bound attitude of 600km, we can calculate the largest visible distance as when the elevation of 10° above the horizon. This corresponds to a maximum distance of 1932.26 km.

Polarisation Loss and Atmospheric Absorption Loss (PAA)

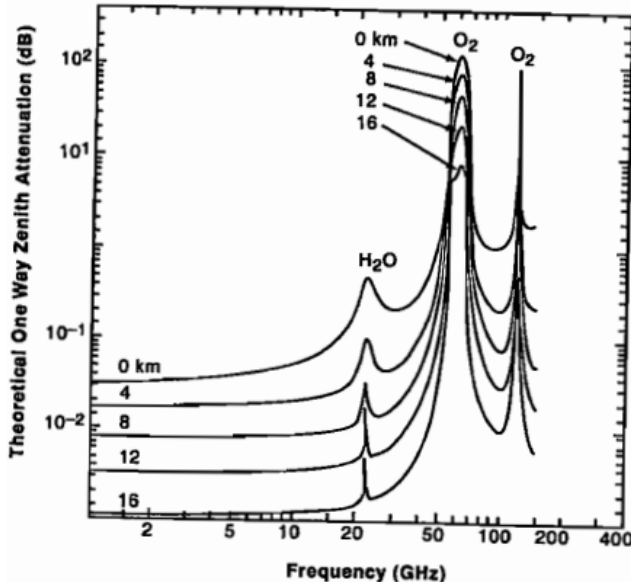


Figure 105: Atmospheric Loss as a function of frequency [10]

Figure 105 shows the amount of attenuation that would occur at different frequencies. From this, we can estimate PAA to be roughly 0.05 dB (very insignificant)

AML

The AML can be calculated from the following formula:

$$AML = 12 \left(\frac{\theta_e}{\theta_{3dB}} \right)$$

Where θ_e is the pointing error, and θ_{3dB} represents the half power bandwidth. This is the angle across which the gain is 50% of the peak gain - estimated from the following:

$$\theta_{3dB} = \frac{21}{fD}$$

Where D is the antenna diameter.

Receiver Signal Power

As the name suggests, this is how much power reaches the receiver. This is simply:

$$P_r = EIRP - \text{Path Loss}$$

Where the path loss takes into account the FSPL, L_p , AA and AML.

G/T (Receiver Figure of Merit)

G/T is a measure of how good a receiver is at receiving the signal. It is calculated as the following:

$$G/T = G_r - L_r - 10\log_{10}(T_s)$$

S/No (Signal to Noise Density Ratio)



S/No represents the signal to noise density ratio. It is calculated as the following:

$$S/No = P_r + G/T - 10 \log_{10} k_B$$

Where k_B is Boltzman's constant, $-10 \log_{10} k$ is equivalent to 228.6 dBW/K-Hz.

Eb/No (Energy per bit to noise power density Ratio)

In order to calculate the actual Eb/No of the system, we can do the following:

$$Eb/No = S/No - 10 \log_{10} D$$

Where D is the data rate of the system.



9 Thermal Subsystem

9.1 Overview

The thermal subsystem is critical to maintaining component integrity, operational reliability, and mission success for the spacecraft. The system must ensure all payloads and subsystems operate within their respective temperature limits under varying mission phases and external thermal environments.

Key thermal requirements include:

- The system must maintain the spacecraft and all its subsystems within a defined operational temperature range. Operation of the spacecraft is expected to take place between -40°C and 80°C.
- All components, including the payload and supporting electronics, must be thermally protected against the on-orbit environment, particularly during peak solar exposure and eclipse conditions.
- A detailed thermal analysis is required, accounting for orbital characteristics, material properties, heat generation, and dissipation pathways. This analysis informs the selection and placement of radiators, thermal interface materials, and insulation.
- The TCS will include passive methods such as surface coatings and insulation. Active components like heaters or heat pipes may be considered depending on the thermal load and control requirements from the FEA simulations.
- Thermal design must integrate with the structural layout to ensure adequate heat conduction paths and avoid thermal-induced stresses or deformations.
- Thermal vacuum and thermal cycling tests are specified to validate the thermal design against simulated space conditions.

9.2 Thermal Design Objectives

The thermal control subsystem is tasked with maintaining all spacecraft components within their operational and survival temperature ranges.

The primary thermal goals are:

- Minimise the use of active thermal control to reduce mass, power consumption, and system complexity.
- Ensure thermal gradients across structural elements remain within allowable limits to prevent warping or misalignment.
- Provide adequate thermal margins to account for material degradation, orbital variations, and uncertainties in thermal loads or properties.

9.3 Thermal Environment

In low Earth orbit (LEO), the spacecraft experiences periodic transitions between sunlit and eclipse phases. These transitions lead to sharp thermal fluctuations. The external thermal environment is characterised by:

- Solar flux of up to 1367 W/m² incident on sun-facing surfaces.
- Earth albedo contributing up to 30% reflectance, depending on surface properties and angle of incidence.
- Earth infrared (IR) radiation of approximately 237 W/m² as a diffuse background.



- Deep space temperature of approximately 3 K, providing a near-ideal radiative sink.

Heat inputs are surface-orientation dependent, while shadowing and eclipse geometry affect net energy gain and loss.

9.4 Temperature Cycles for 4 Orbital Periods

The simulation is from the PiCPoT project and developed at Politecnico di Torino [34]. It was implemented using MATLAB and employs a finite difference method to solve the thermal energy balance of a CubeSat operating in low Earth orbit (LEO). The model accounts for three-dimensional, time-dependent behaviour. It includes both external heat sources such as direct solar radiation, albedo, and Earth's infrared (IR) emission and internal heat generation from the satellite's onboard electronics. Only thermal passive control systems were used.

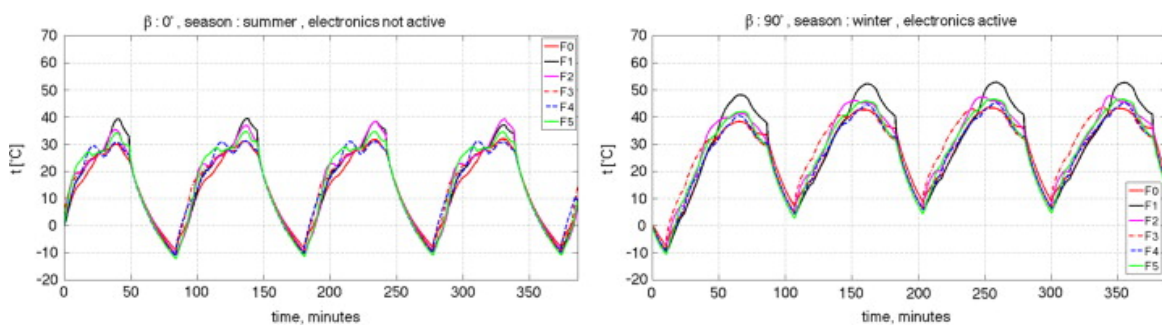


Figure 106: Temperature profiles at the central point of each external face are shown for the most extreme conditions over four orbital cycles. The left side illustrates the coldest case scenario, while the right side depicts the hottest case.

Note that this is only an approximation with an inclination equal to 98° and an altitude of 600 km.

Key Results from Literature Analysis

- Maximum temperature during sunlight exposure: 40°C
- Minimum temperature during eclipse: -10°C
- Thermal range per orbit: $\Delta T \approx 50^\circ\text{C}$
- Duration of periods: 90 minutes

9.5 Thermal Temperatures of Components

Table 44: CubeSat Component Thermal Breakdown

Subsystem	Min Temp (°C)	Max Temp (°C)
Structural Subsystem		
Deployment Switch	-25	85
Attitude Determination and Control Subsystem		
Magnetorquer	-40	85
VFMI-7700 lux Sensor	-25	80
ArdPilot BN0055	-25	80
Electrical Power System		
OBC	-40	80
1W Solar Panel 80x100mm	-40	85
Sony 18650 VTC6 Battery	-20	60

Subsystem	Min Temp (°C)	Max Temp (°C)
Boost Converter	-40	80
Buck Converter	-40	125
Current Sensor	-40	80
OBC & Handling Subsystem		
PCB	-50	125
Communication Subsystem		
Antenna	-40	85
NanoComm AX100UL modem	-30	85
Payload		
Spectroscopy Sensor AS726x	-40	85

9.6 Finite Element Analysis

9.6.1 Thermal Vacuum Cycling

The cyclic thermal analysis modelled a transient temperature profile ranging from -40°C to +80°C, representing a typical orbital thermal environment. The cycle followed a controlled ramp rate of 1°C per minute, increasing from the cold soak up to the hot condition over 120 minutes, before reversing at the same rate. This symmetric profile replicates the slow but continuous heating and cooling experienced in low Earth orbit due to solar exposure and shadow transitions. The simulation was conducted in vacuum, meaning no convective effects were present, and all thermal responses were governed by conduction within the structure and radiative exchange between surfaces. Note that the below shows the FEA at the peak and trough of the cycles.

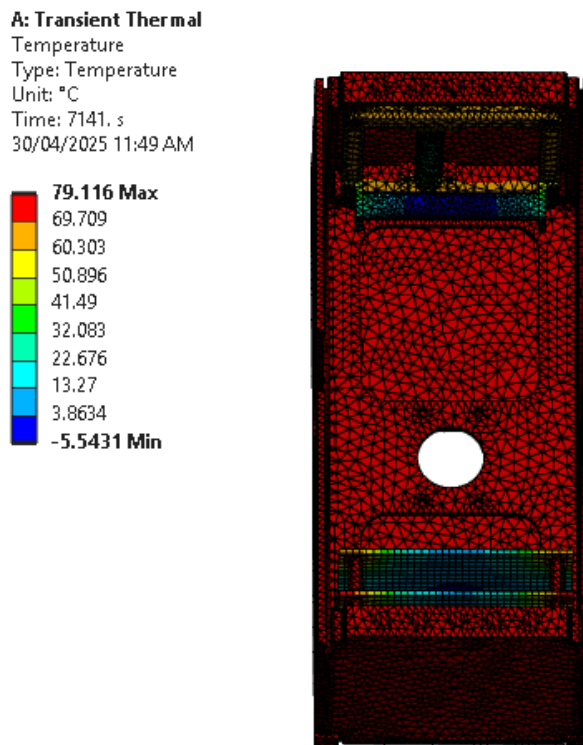


Figure 107: Finite Element Analysis model showing the temperature distribution at the peak of the cyclic thermal test.

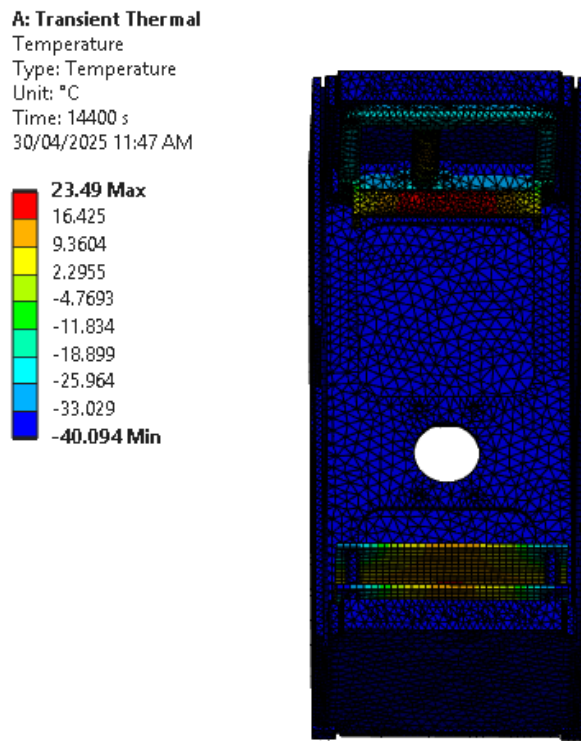


Figure 108: Finite Element Analysis model showing the temperature distribution at the trough of the cyclic thermal test.

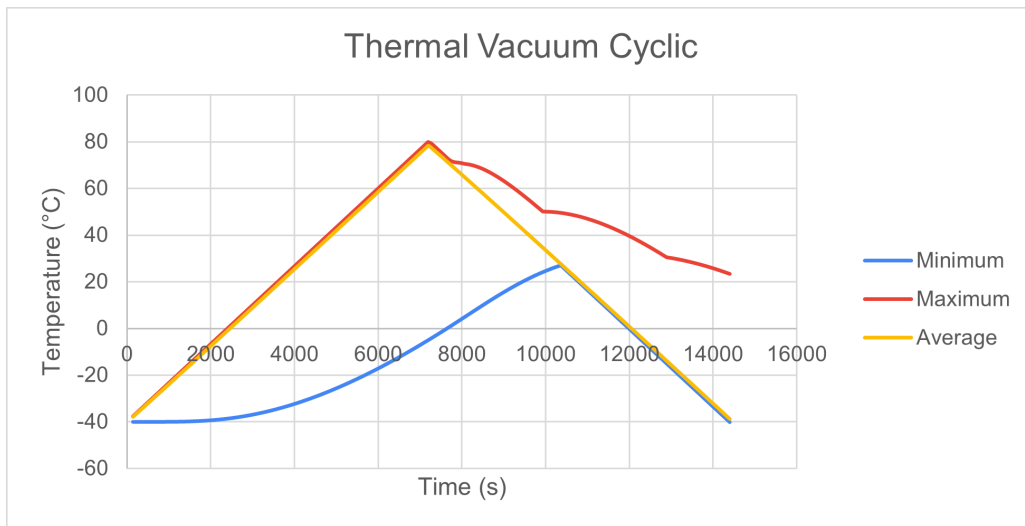


Figure 109: Finite Element Analysis model showing the temperature distribution throughout the cyclic thermal test.

As shown in the temperature-time graph, the maximum, minimum, and average temperatures of the CubeSat varied gradually throughout the cycle. The external surfaces, where the heat flux was applied, reached the maximum temperature of approximately 80°C around 7200 seconds, after which they began to cool. The minimum internal temperatures, however, lagged behind in response to the applied heat, only reaching their peak slightly after the midpoint of the cycle and then cooling more gradually. This delay is attributed to the thermal inertia of the internal components and the natural temperature gradient established between the outer and inner sections of the CubeSat.



Importantly, at no point during the test did the internal or external temperatures exceed the defined operational bounds. The structure remained within the temperature envelope of -40°C to $80^{\circ}\text{C} \pm 2^{\circ}\text{C}$ throughout the duration of the test. This result confirms the feasibility of the current thermal design under simplified cyclic thermal loading. While actual orbital conditions may involve more complex and repeated temperature swings, this test provides confidence that the CubeSat structure can withstand the expected thermal stresses without material degradation or excessive thermal strain.

Overall, the simulation demonstrates sufficient thermal resilience for the intended mission environment. Future work may involve refining the model to incorporate multiple cycles, component-level heat generation, and more realistic orbital heat flux conditions to further validate long-term survivability.

9.6.2 Thermal Vacuum Bake-Out

The thermal bakeout simulation was conducted at a constant external temperature of 80°C for a duration of three hours. Due to the lack of convective heat transfer in vacuum, the model relied solely on conduction through the structure and radiative heat exchange to achieve internal thermal equilibrium. Heat was applied to the outer surfaces of the CubeSat structure, which introduced observable temperature gradients between the exterior panels and internal components.

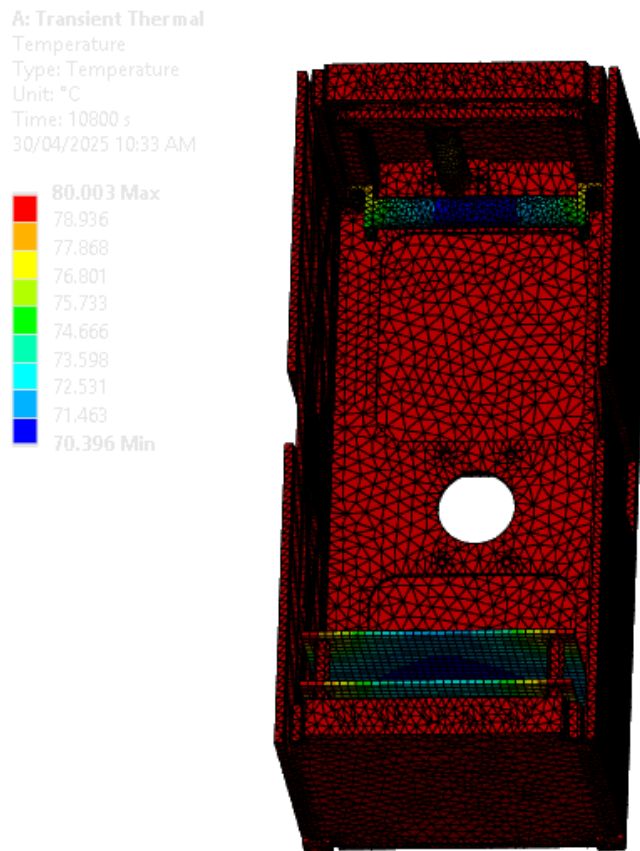


Figure 110: Finite Element Analysis model showing the temperature distribution at the end of the thermal test.

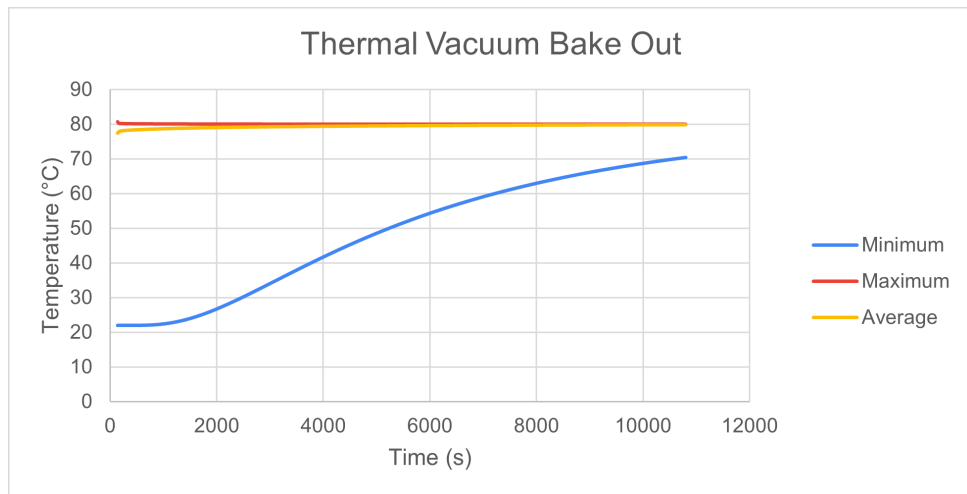


Figure 111: Finite Element Analysis model showing the temperature distribution throughout the bake-out thermal test.

Results from the simulation showed a gradual increase in internal temperatures over time, with outer surfaces reaching 80°C more rapidly than the interior regions. The graphs generated from the analysis plotted maximum, minimum, and average temperatures as functions of time, clearly illustrating the thermal lag within the system. Initially, the maximum temperature climbed quickly as surface elements were directly exposed to the thermal boundary condition, while the minimum temperature, representing the coldest, most insulated internal regions, increased at a slower rate. By the end of the three-hour period, the average temperature approached equilibrium, but a noticeable temperature difference remained between the internal and external parts.

9.7 Thermal Controls

The CubeSat utilises a passive thermal control system that relies on a combination of surface coatings, insulation materials, and thermal tapes to regulate internal temperatures without active mechanisms. This approach is suited for small satellites, where simplicity, mass efficiency, and heritage components are critical.

Titanium Dioxide White Paint is applied to sun-facing surfaces to reflect incident solar radiation and reduce heat absorption. It offers a practical and accessible alternative to space-qualified coatings such as AZ-93, while still delivering high reflectivity and thermal moderation.

Internally, Mylar Multilayer Insulation (MLI) is installed around temperature-sensitive components to minimise radiative heat transfer. Typically consisting of 10 to 20 layers [35], each approximately 12µm thick [36], MLI provides thermal isolation with minimal mass impact. It will be placed between the internal walls of the CubeSat and the boards. Kapton tape is also used to stabilise temperatures around exposed pin or soldered connection while serving as an effective electrical insulator.

These materials were chosen for their thermal performance, compatibility with CubeSat constraints, and established use in space applications.

References

- [1] LUNATICS Team, “Lunatics preliminary design review,” Unpublished group assignment, 2025, assignment submitted for AERO4701 at the University of Sydney.
- [2] A. Eldering, C. Dell, P. Wennberg, D. Crisp, M. Gunson, C. Viatte, C. Avis, A. Braverman, R. Castaño, A. Chang, L. Chapsky, C. Cheng, B. Connor, L. Dang, G. Doran, B. Fisher, C. Frankenberg, D. Fu, R. Granat, and J. Yoshimizu, “The orbiting carbon observatory-2: First 18 months of science data products,” *Atmospheric Measurement Techniques Discussions*, vol. 10, pp. 1–30, 09 2016.
- [3] SparkFun, *AS7265x Smart 18-Channel VIS to NIR SpectralID 3-Sensor Chipset with Electronic Shutter Datasheet*, v1-04 ed., ams, 07 2018.
- [4] PBS, “The origins of life,” n.d., accessed: 2025-05-02. [Online]. Available: https://www.pbs.org/wgbh/nova/teachers/activities/3113_origins_01.html
- [5] V. Semiconductors, *VEML7700: High Accuracy Ambient Light Sensor with I²C Interface*, Vishay Intertechnology, Inc., Malvern, PA, USA, Nov. 2024, accessed: 2025-05-02. [Online]. Available: <https://www.vishay.com/docs/84286/veml7700.pdf>
- [6] PC/104 Embedded Consortium, “PC/104 Specification Version 2.6,” PC/104 Embedded Consortium, Tech. Rep., October 2008, accessed: 2025-05-01. [Online]. Available: https://pc104.org/wp-content/uploads/2015/02/PC104_Spec_v2_6.pdf
- [7] Analog Devices, *MAX6369–MAX6374: Low-Power, Single/Dual-Level, μP Reset Circuits*, 2007, accessed: 2025-05-02. [Online]. Available: <https://www.analog.com/media/en/technical-documentation/data-sheets/max6369-max6374.pdf>
- [8] Core Electronics. (2025) DS3231M MEMS Precise RTC. Accessed: 2025-05-02. [Online]. Available: <https://core-electronics.com.au/ds3231m-mems-precise-rtc.html>
- [9] Texas Instruments, *TCA9548A Low-Voltage 8-Channel I²C Switch With Reset Function*, 2015, accessed: 2025-05-02. [Online]. Available: <https://www.ti.com/lit/ds/symlink/tca9548a.pdf>
- [10] D. F. E. J. R. Wertz and J. J. Puschell, “Space mission engineering: The new smad,” 2011.
- [11] Markforged, “Material datasheet: Composites,” 2021, accessed: 2025-04-28. [Online]. Available: <https://static.markforged.com/downloads/composites-data-sheet.pdf>
- [12] W. Material, “Aluminum 6061, al 6061-t6 alloy properties, density, tensile & yield strength, thermal conductivity, modulus of elasticity, welding,” 2021, accessed: 2025-04-28. [Online]. Available: <https://www.theworldmaterial.com/al-6061-t6-aluminum-alloy/>
- [13] W. D. Callister, *Materials Science and Engineering: An Introduction*, 7th ed. Hoboken, NJ: John Wiley & Sons, 2007.
- [14] J. Jerred, “APRS and AX.25 Demystified: Full Packet Generation and Frame Encoding,” n.d., accessed: 2025-03-20. [Online]. Available: <https://joshuajer.red/blog/2023-01-04-APRS-and-ax25#ax25-frame-generation>
- [15] ahrs, “Extended kalman filter,” 2025, accessed: 20/05/2025. [Online]. Available: <https://ahrs.readthedocs.io/en/latest/filters/ekf.html>
- [16] <https://ahrs.readthedocs.io/en/latest/filters/ekf.html>, “Cubesat attitude determination via kalman filtering of magnetometer and solar cell data,” University of Illinois, Urbana-Champaign, Tech. Rep., 2011.
- [17] P. Alken, E. Thébault, C. D. Beggan, S. Macmillan, A. Chulliat, J. Baerenzung, W. J. Brown, S. C. Finlay, N. Olsen, M. Mandea, and C. C. Finlay, “International geomagnetic reference field:



-
- the thirteenth generation,” *Earth, Planets and Space*, vol. 73, no. 1, p. 49, 2021. [Online]. Available: <https://earth-planets-space.springeropen.com/articles/10.1186/s40623-020-01288-x>
- [18] Jaycar Electronics, “0.5mm enamel copper wire spool,” <https://www.jaycar.com.au/0-5mm-enamel-copper-wire-spool/p/WW4016>, accessed: 2025-04-25.
- [19] “High quality new computer cnc automatic coil winder coil winding machine for 0.03-1.2mm wire 110/ 220v factory outlet,” <https://www.aliexpress.com/item/1005003522101667.html>, accessed: 2025-04-30.
- [20] J. Amin, “The design, assembly, and testing of magnetorquers for a 1u cubesat mission,” Georgia Institute of Technology, Atlanta, GA, AE 8900 MS Special Problems Report, December 2019, advisor: Dr. E. Glenn Lightsey. [Online]. Available: <https://ssdl1.gatech.edu/sites/default/files/ssdl-files/papers/mastersProjects/AminJ-8900.pdf>
- [21] P. A. Capo-Lugo, J. Rakoczy, and D. Sanders, “The b-dot earth average magnetic field,” NASA Marshall Space Flight Center, Preprint M13-2829, 2013, nASA Technical Reports Server (NTRS) Document ID: 20140016484. [Online]. Available: <https://ntrs.nasa.gov/api/citations/20140016484/downloads/20140016484.pdf>
- [22] F. L. Markley, “Quaternion derivatives and integrations of rotational kinematics,” *Journal of Guidance, Control, and Dynamics*, vol. 26, no. 2, pp. 307–315, 2003.
- [23] P. C. Hughes, *Spacecraft Attitude Dynamics*. Dover Publications, 1986.
- [24] HKJ, “Test/review of samsung inr18650-35e 3500mah (pink) 3,” September 2021, accessed: 2025-04-30. [Online]. Available: <https://budgetlightforum.com/t/test-review-of-samsung-inr18650-35e-3500mah-pink-3/67765>
- [25] Texas Instruments, *BQ24650 Synchronous Switch-Mode Battery Charge Controller for Solar Power*, Texas Instruments, 2019, sLUSAJ0C datasheet. [Online]. Available: <https://www.ti.com/lit/ds/symlink/bq24650.pdf>
- [26] ABLIC Inc., *S-82A2A/B/C Series Battery Protection IC For 2-Serial-Cell Pack*, ABLIC Inc., February 2024, rev. 092623 datasheet. [Online]. Available: https://au.mouser.com/datasheet/2/1490/S82A2A_B_C_E-3430427.pdf
- [27] Texas Instruments, *TPS63060 High-Efficiency Single Inductor Buck-Boost Converter With 2-A Switches*, Texas Instruments, 2016, sLVSBL5B datasheet. [Online]. Available: <https://www.ti.com/lit/ds/symlink/tps63060.pdf>
- [28] ——, *INA219 Zero-Drift, Bidirectional Current/Power Monitor With I2C Interface*, Texas Instruments, 2021, sBOS448H datasheet. [Online]. Available: <https://www.ti.com/lit/ds/symlink/ina219.pdf>
- [29] Association Connecting Electronics Industries (IPC), “IPC-2221A: Generic Standard on Printed Board Design,” IPC, Tech. Rep., May 2003, accessed: 2025-05-01. [Online]. Available: <https://www.ipc.org/TOC/IPC-2221A.pdf>
- [30] PCBASIC. (2021) FR4 Dielectric Constant - A Guide to PCB Material Properties. Accessed: 2025-05-02. [Online]. Available: https://www.pcbasic.com/blog/fr4_dielectric_constant.html
- [31] NASA, “NASA-STD-8739.1: Workmanship Standard for Polymeric Applications (Assembly, Staking, Bonding, Coating, and Encapsulation),” National Aeronautics and Space Administration, Tech. Rep., 2013, accessed: 2025-05-02. [Online]. Available: <https://standards.nasa.gov/standard/nasa/nasa-std-87391>
- [32] University of Sydney, “Whole orbit data format,” n.d., accessed: 2025-03-20. [Online]. Available: <https://canvas.sydney.edu.au/courses/63148/files/40577460?wrap=1>



-
- [33] T. U. of Sydney, “Groundstation - arc training centre for cubesats, uavs and their applications,” 2018.
 - [34] P. Fortescue, M. Swartwout, and P. Dervan, “Thermal design of cubesat payloads: A review of lessons learned and future challenges,” *Acta Astronautica*, vol. 115, pp. 247–256, 2015. [Online]. Available: <https://www.sciencedirect.com/science/article/pii/S0094576515001940>
 - [35] NASA Small Spacecraft Systems Virtual Institute, “Thermal control — state of the art report,” 2024, accessed: 2025-05-02. [Online]. Available: <https://www.nasa.gov/smallsat-institute/sst-soa/thermal-control/>
 - [36] Médecins Sans Frontières (MSF), “Blanket, survival, 220 x 140 cm, thickness 12 microns,” 2024, accessed: 2025-05-02. [Online]. Available: <https://unicat.msf.org/cat/product/19000?category=20394>
 - [37] X. Wu, “AERO4701 USyd CubeSat System Requirements and Recommendations,” University of Sydney, Tech. Rep., February 2025.
 - [38] NASA, “U.S. Standard Atmosphere ,” 1976.
 - [39] NASA Space Communications and Navigation (SCaN) Program, “Technology readiness levels,” 2023, accessed: 2025-04-25. [Online]. Available: <https://www.nasa.gov/directorates/somd/space-communications-navigation-program/technology-readiness-levels/>



Appendix A Mission requirements

The following Mission Requirements were taken, adapted, and expanded upon from the University of Sydney AERO4701 CubeSat System Requirements and Recommendations [37].

A.1 CubeSat System Requirements

Table 45: Structural system requirements.

Requirement ID	Description	Verification Criteria	Verification Method	Phase
S-STR-01	The CubeSat SHALL fit within a $100 \times 100 \pm 0.1$ mm footprint.	Measurement within dimension	Dimension measurement	AIT
	The CubeSat SHALL have a height of 227.0 ± 0.1 mm.	Measurement within dimension	Dimension measurement	AIT
	The CubeSat SHALL have feet of $8.5 \times 8.5 \pm 0.1$ mm.	Measurement within dimension	Dimension measurement	AIT
	The CubeSat's external edges SHALL be rounded $R \times 1$ mm or chamfered $45^\circ \times 1$ mm.	Measurement within dimension	Dimension measurement	AIT
S-STR-02	The CubeSat SHALL use the reference frame as shown in Figure 112.	Design stage	ADCS testing	PDR
S-STR-03	The CubeSat SHALL not exceed a mass of 2.66 kg.	$\text{Mass} \leq 2.66 \text{ kg}$	Mass measurement	AIT
S-STR-04	The CubeSat SHALL have its COG within 10 mm of the geometric centre.	COG within limit	COG test	AIT
S-STR-05	The deployment switches SHALL be non-latching (electrically or mechanically).	Deployment switches do not latch	Design	PDR
S-STR-06	The rails and standoffs SHALL be constructed of material that cannot be cold-welded to adjacent materials.	Design stage	Materials testing	CDR

Table 46: Attitude & Orbit Control Subsystem (AOCS) requirements.

Requirement ID	Description	Verification Criteria	Verification Method	Phase
S-AOC-01	The CubeSat SHALL be able to recover from tip-off rates up to $\pm 50^{\circ} \text{ s}^{-1}$ within two days (nominal conditions).	Attitude recovered	Simulation	CDR
	The CubeSat SHOULD be able to recover from tip-off rates up to $\pm 90^{\circ} \text{ s}^{-1}$ in off-nominal situation.	Attitude recovered	Simulation	CDR
S-AOC-02	The CubeSat SHALL be able to point its direction within $\pm 5^{\circ}$.	Pointing within the tolerance	Simulation and measurement	CDR
	The CubeSat SHOULD be able to point its direction within $\pm 2^{\circ}$.	Pointing within the tolerance	Simulation and measurement	CDR
S-AOC-03	The CubeSat SHALL maintain its orbit for six months.	Simulated satellite remains in orbit	Simulation	AIT
	The CubeSat SHOULD maintain its orbit for twelve months.	Simulated satellite remains in orbit	Simulation	CDR

Table 47: Electrical Power System (EPS) requirements.

Requirement ID	Description	Verification Criteria	Verification Method	Phase
S-EPS-01	The power supply SHALL be provided at appropriate voltage by solar array or battery to meet power requirements for all subsystems in all modes of operation.	Satellite runs in all modes	EPS testing	AIT
S-EPS-02	The CubeSat SHALL be able to be commissioned in orbit following the last powered-down state without battery charging, inspection, or functional testing for a period of up to eight months.	Returns after powered down	EPS testing	AIT
S-EPS-03	The CubeSat SHALL be powered off during the launch until deployed from the deployment system.	Satellite is off when not deployed	EPS testing	AIT
S-EPS-04	The CubeSat SHALL have battery current surge and over-charge protection circuits in place.	Batteries do not receive excess current	EPS testing	AIT

Table 48: Onboard Computer & Data Handling (OBC/OBDH) requirements.

Requirement ID	Description	Verification Criteria	Verification Method	Phase
S-OBC-01	The CubeSat SHALL collect Whole Orbit Data (WOD) and log telemetry every minute for the entire duration of the mission. The WOD must contain: time; spacecraft mode; battery bus voltage; battery bus current; current on regulated 3.3V bus; current on regulated 5V bus; communication subsystem temperature; EPS temperature; and battery temperature.	Data passes software tests for data packaging	OBC Testing	CDR
S-OBC-02	The WOD SHALL be stored on the OBC until they are successfully downlinked.	Data before transmission is received	OBC Testing	AIT
S-OBC-03	Any computer clock used on the CubeSat and on the ground segment SHALL exclusively use Coordinated Universal Time (UTC) as time reference.	Computers use UTC	OBC Testing	CDR
S-OBC-04	The OBC SHALL have a real time clock information with an accuracy of 500 ms during science operation. Relative times should be counted/stored according to the epoch 01.01.2000 00:00:00 UTC.	Time stamps of data within tolerance	OBC Testing	CDR
S-OBC-05	The OBSW programmed and developed SHALL only contain code that is intended for use on that CubeSat on the ground and in orbit.	Software is necessary	Design	CDR
S-OBC-06	The OBSW code SHALL include comments and sensible variable names such that functionality and control flow behaviour can be understood.	Code conforms to Google C++ Style Guide	Design	CDR
S-OBC-07	A command SHALL be implemented that can delete any SU data held in mass memory originating prior to a Date-Time stamp given as a parameter.	Data deleted successfully	OBC Testing	AIT
S-OBC-08	The OBC SHALL restart if it stops functioning for 15 seconds.	OBC Restarts	OBC Testing	AIT
S-OBC-09	The software on the OBC SHOULD have deterministic execution	Code runs on a single thread	Design	CDR
S-OBC-10	The software on the OBC SHALL have backup paths and fail over methods	Code uses error management	Design	CDR
S-OBC-11	The software SHALL handle single-event upsets	Code checks the validity of the received data	Design	CDR

Table 49: Telemetry, Tracking & Command (TT&C) requirements.

Requirement ID	Description	Verification criteria	Verification method	Phase
S-TTC-01	The CubeSat SHALL have and make use of its unique satellite ID.	ID used in data transmission	COMMS testing	PDR
S-TTC-02	The CubeSat SHALL transmit the current values of the WOD parameters and its unique satellite ID through a beacon at least once every 30s.	Packets received successfully	COMMS testing	AIT
	The beacon SHOULD be transmitted every 10s during LEOP phase to allow for multiple receptions of the beacon during a pass.	Packets received successfully	COMMS testing	AIT
	The CubeSat SHALL use the AX.25 Protocol.	Data follows protocol	COMMS testing	CDR
S-TTC-03	The data type during downlink SHALL be specified in the Secondary Station Identifier (SSID) in the destination address field of the AX.25 frame.	Data type specified	COMMS testing	CDR
	Science data SHALL be indicated using 0b1111 and WOD with 0b1110	Data indicated properly	Design	CDR
S-TTC-04	A user-friendly and documented software SHALL be implemented, consisting of a) CubeSat data Frames Decoder; b) CubeSat data Packet decoder; and c) CubeSat data Viewer that complies with radio amateur regulations.	Readable, commented software	Design	CDR

Table 50: Thermal Control Subsystem Requirements

Requirement ID	Description	Verification Criteria	Verification Method	Phase
S-THE-01	The CubeSat SHALL maintain all its electronic components within their operating temperature range while in operation and within the survival temperature range at all other times after deployment.	Component temperatures within range	Thermal testing/simulation	CDR
S-THE-02	The CubeSat SHALL survive within the temperature range of -40°C to $+80^{\circ}\text{C}$ from the time of launch until its end of life.	Data transmission continues during thermal cycling	Thermal testing/simulation	CDR
S-THE-03	The CubeSat SHALL undergo Thermal Vacuum Cycling and Bake-Out testing to verify its thermal performance in a space-like environment.	Compliance with Thermal Vacuum requirements	Thermal testing/simulation	CDR
S-THE-04	The CubeSat SHALL not exceed a temperature variation rate of $\geq 1^{\circ}\text{C}/\text{min}$ during testing.	Measured thermal variation	Thermal testing/simulation	CDR

Table 51: General system requirements.

Requirement ID	Description	Verification criteria	Verification method	Phase
S-GEN-01	The CubeSat SHALL be designed to have an in-orbit lifetime of at least six months.	In-orbit lifetime ≥ 6 months	Design	PDR
S-GEN-02	The CubeSat SHALL not use any material that has the potential to degrade in an ambient environment during storage after assembly (as long as two years).	Materials do not degrade within 2 years	Design	PDR
S-GEN-03	The CubeSat SHALL withstand total contamination of 3.1 mg/m^2 at all phases of the launch vehicle ground operation and in-flight.	Components withstand contamination	Design	CDR
S-GEN-04	“Apply Before Flight” items, including tags or labels, SHALL not protrude past the dimensional limits of the CubeSat when fully inserted.	No protrusions on CubeSat	Visual inspection	AIT
S-GEN-05	“Remove Before Flight” items SHALL be identified by a bright red label of at least 4 cm^2 containing the words “REMOVE BEFORE FLIGHT” and the name of the satellite printed in large white capital letters.	Clearly visible	Visual inspection	AIT
S-GEN-06	The CubeSat ID SHALL be printed, engraved, or marked on the CubeSat.	Clearly visible	Design	AIT

A.2 Payload Requirements

Table 52: Science and payload mission requirements.

Requirement ID	Description	Verification criteria	Verification method	Phase
SCIENCE				
P-SCI-01	Spectral data SHALL be gained across the entire atmosphere over the mission duration.	Measurements over defined grid.	Simulation	CDR
P-SCI-02	The CubeSat SHALL be in a sun-synchronous orbit.	Orbit is sun-synchronous	Simulation	PDR
P-SCI-03	The CubeSat SHALL maintain a Nadir-pointing orientation with an attitude stability of $\pm 5^\circ$.	Pointing vector has $\leq \pm 5^\circ$ variation.	ADCS testing	CDR
P-SCI-04	Spectral data SHALL be recorded only when reflected sunlight is available.	Incoming light intensity > dark photocurrent.	Hardware testing	CDR
P-SCI-05	The mission SHALL have a lifetime of at least one year to achieve full global atmospheric mapping.	Mission lifetime > 1 year	Simulation	PDR
PAYLOAD				
P-PAY-01	The spectrometer payload SHALL observe light over a visible to near-infrared wavelength range.	Return wavelengths across range.	Payload testing	PDR
P-PAY-02	The payload SHALL have a field of view that allows for a minimum swath width of 200 km.	Swath width ≥ 200 km.	Simulation	PDR
P-PAY-03	The payload SHALL take measurements at regular intervals with at least 90% overlap to ensure high resolution data readings.	Measurements taken at 2s+.	Design	CDR
P-PAY-04	The CubeSat SHALL downlink at least 2 MB per pass using UHF/S-band with ground station access at least once per day.	2 MB transmitted within visible time frame	COMMS testing	AIT

Appendix B Appendix

B.1 CubeSat Reference Frame

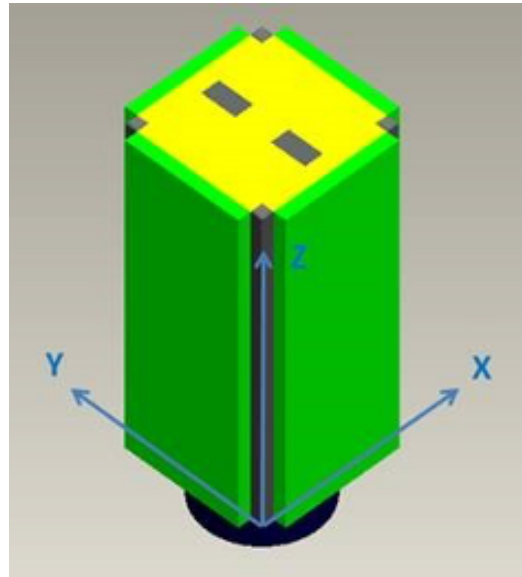


Figure 112: CubeSat reference frame

B.2 QUEST Variable Definitions

$$\sigma = \text{tr}(\mathbf{B}) \quad (\text{B.1})$$

$$\mathbf{S} = \mathbf{B} + \mathbf{B}^T \quad (\text{B.2})$$

$$\mathbf{Z} = \sum_{i=1}^n a_i (\hat{\mathbf{W}}_i \times \hat{\mathbf{V}}_i) \quad (\text{B.3})$$

$$a = \sigma^2 - \mathcal{K} \quad (\text{B.4})$$

$$b = \sigma^2 + \mathbf{Z}^T \mathbf{Z} \quad (\text{B.5})$$

$$c = \Delta + \mathbf{Z}^T \mathbf{S} \mathbf{Z} \quad (\text{B.6})$$

$$d = \mathbf{Z}^T \mathbf{S}^2 \mathbf{Z} \quad (\text{B.7})$$

$$\mathcal{K} = \text{tr}(\text{adj}(\mathbf{S})) \quad (\text{B.8})$$

$$\Delta = \det(\mathbf{S}) \quad (\text{B.9})$$

$$\alpha = \lambda^2 - \sigma^2 + \mathcal{K} \quad (\text{B.10})$$

$$\beta = \lambda - \sigma \quad (\text{B.11})$$

B.3 External Disturbance Justification [1]

- Gravity Gradient: The portion of the satellite at lower altitude will experience a greater gravitational pull, where it will create a torque to align the Z -axis to point towards Earth. Equation (B.12) describes the torque from gravity gradient.

$$T_g = \frac{3\mu}{2R^3} |I_{zz} - I_{yy}| \sin 2\theta \quad (\text{B.12})$$

$\mu = 3.986e10^{14} m^3/s^2$ is the Earth's gravitational constant. The distance between the satellite and Earth's centre is $6936km$. θ is the angle from the Z principal axis and the local vertical; this was assumed to be 45° . The moment of inertia about the Y and Z axis (I_{yy} and I_{zz} respectively) are $0.004433 kg \cdot m^2$ and $0.01922 kg \cdot m^2$. This was calculated assuming the CubeSat was a rectangular prism

- Solar Radiation Pressure (SRP): Momentum from solar radiation exerts varying pressure depending on the reflectance and absorption of different materials of the CubeSat. This imbalance of pressure distribution results in a torque, alternatively a torque is also generated when the COM and Centre of Pressure (COP) are not aligned. Equation (B.13) is used to estimate the torque from SRP, it assumes constant reflectance across the satellite's surface.

$$T_s = \frac{\Phi}{c} A_s (1 + q) (CP_s - COM) \cos \varphi \quad (\text{B.13})$$

The reflectance factor q is assumed $q = 1$ for perfect reflection, as a conservative estimate, since full reflectance results in double the pressure exerted [10]. The solar constant (Φ) in LEO is approximated to be $1367W/m^2$. c is the speed of light at $3e10^8 m/s$. A_s the area illuminated by sunlight to be $0.1112m^2$, this assumes all sides of the CubeSat is illuminated as a conservative estimate. The distance from CP to COM was assumed to be worst case scenario at $0.227m$. φ , the angle of incidence of the Sun was estimated to be 0° .

- Atmospheric Drag: Air particles impacting the satellite create a torque similar to SRP with a misalignment of the atmospheric COP and COM. Torque from atmospheric drag is estimated by Equation (B.14).

$$T_a = \frac{1}{2} \rho C_d A_r V^2 (CP_a - COM) \quad (\text{B.14})$$

Making conservative estimates, the drag coefficient (C_d) is 2.2, ram area (A_r) is $0.1112m^2$, air density (ρ) is $2.210 \times 10^{-13} kg/m^3$ [38], and the distance between the atmospheric CP and COM is $0.1m$.

Table 53: External Torque Disturbances

External Disturbance	Torque ($N \cdot m$)
Gravity Gradient	2.65×10^{-8}
Solar Radiation Pressure	2.30×10^{-7}
Atmospheric Drag	1.57×10^{-7}
Total	4.14×10^{-7}

Each magnetorquer will be able to counteract τ_{max} . The required torque ($\tau_{required}$) will be $6.21 \times 10^{-7} Nm$ to account for a factor of safety of 1.5. The magnetic dipole required $\mu_{required}$ can be obtained through the following relationship where B is the magnetic flux density.

$$\tau_{required} = \mu_{required} \times B \quad (\text{B.15})$$



Using a magnetic flux density of $4.0 \times 10^{-5} T$, we can find the required magnetic dipole to be $\mu_{\text{required}} = 0.016 A \cdot m^2$. This can be related to the number of coils (N), current (I) and loop area (A_L) using the following expression.

$$\mu = N \cdot I \cdot A_L \quad (\text{B.16})$$

We can now use the known supplied current and solonoid areas to determine the required number of coils for the magnetorquer in each direction. The maximum supplied current to the magnetorquer is 1.2 Amps, while the solonoid area varies depending on the axis because rod magnetorquers are used in the X and Y directions while a square plate is used for the Z direction. The full magnetorquer assembly can be seen in Figure 59 and the minimum magnetorquer design required is presented in Table 25.

B.4 B-Dot Supplementary Simulations

Supplementary simulations of the B-Dot controller with varying saturation currents and gains.

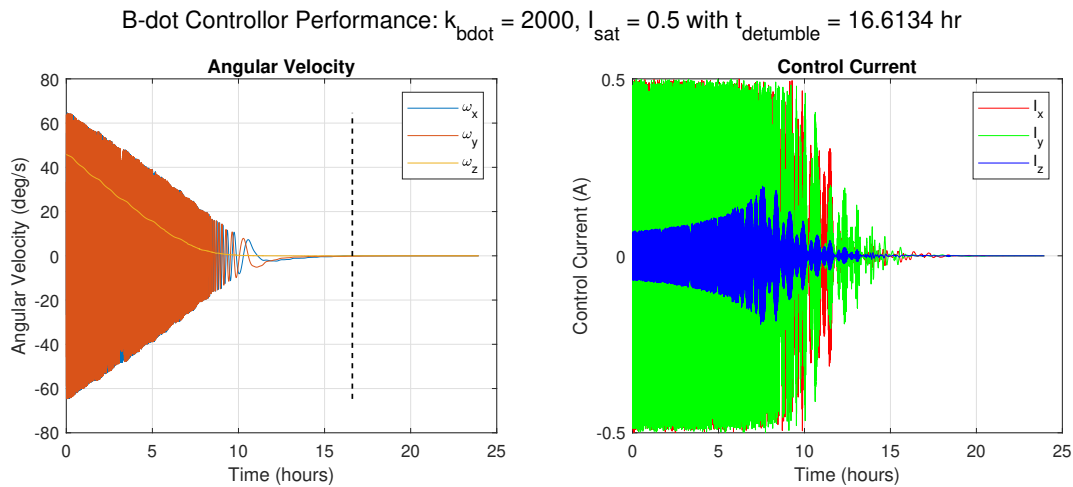


Figure 113: B-Dot Detumbling Simulation 1

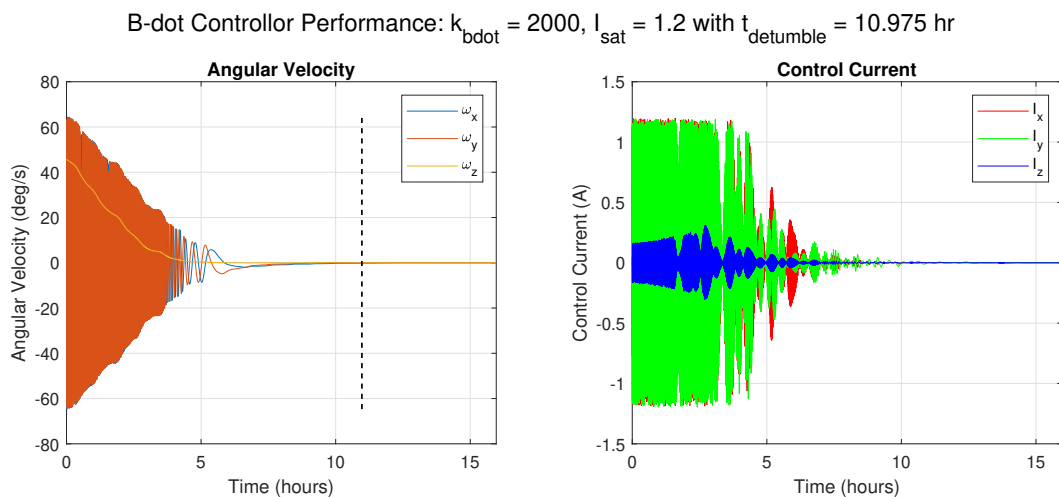


Figure 114: B-Dot Detumbling Simulation 2

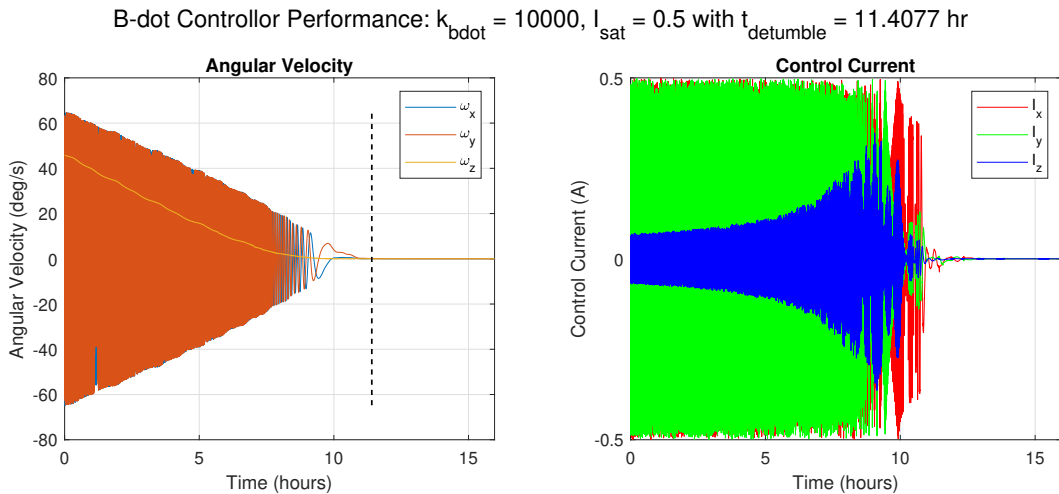


Figure 115: B-Dot Detumbling Simulation 3

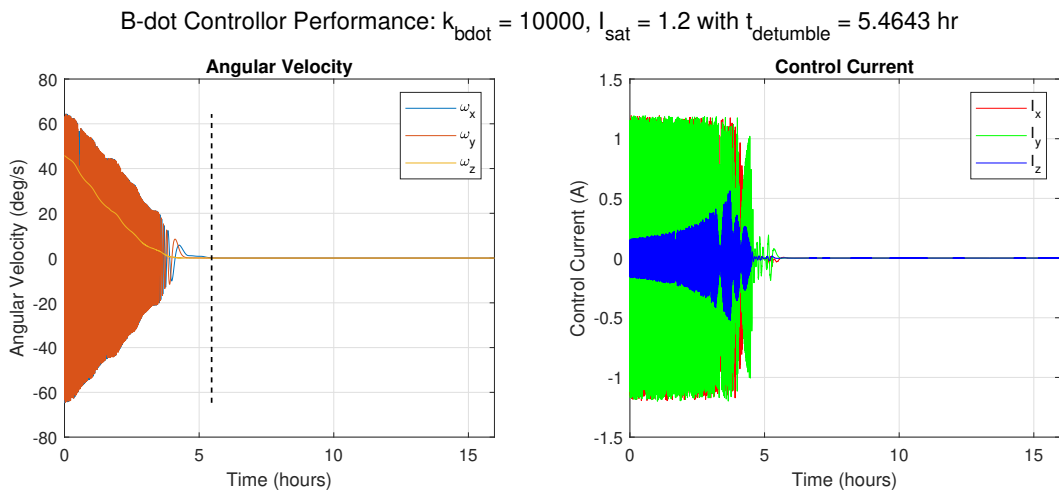


Figure 116: B-Dot Detumbling Simulation 4

B.5 TRL Definition

A TRL, Technical Readiness Level is defined by NASA as "a type of measurement system used to assess the maturity of a particular technology." These levels range from 1 to 9 and are classified by NASA as follows [39].

- **TRL 9** - Actual system "flight proven" through successful mission operations.
- **TRL 8** - Actual system completed and "flight qualified" through test and demonstration (ground or space).
- **TRL 7** - System prototype demonstration in a space environment.
- **TRL 6** - System/subsystem model or prototype demonstration in a relevant environment (ground or space).
- **TRL 5** - Component and/or breadboard validation in relevant environment.
- **TRL 4** - Component and/or breadboard validation in laboratory environment.
- **TRL 3** - Analytical and experimental critical function and/or characteristic proof-of-concept.
- **TRL 2** - Technology concept and/or application formulated.



- **TRL 1** - Basic principles observed and reported.

B.6 FCS Calculation

The FCS is a CRC16 (ISO 3309). This is a standard CRC implemented in many ways, with the code we will use shown below, written by Andres Vahter.

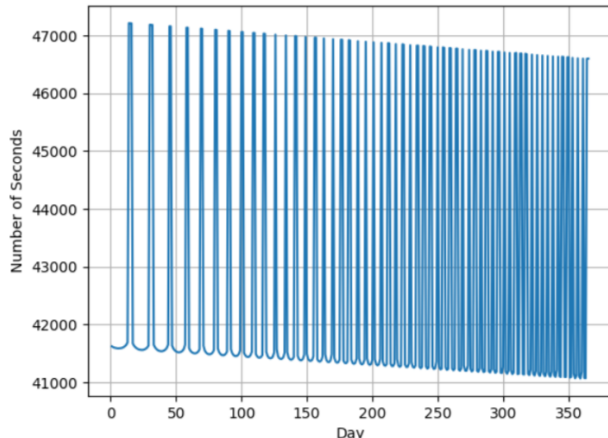
```
uint16_t calculateFcs(const std::vector<uint8_t> &input_data) {
    uint16_t crc = 0xFFFF;
    uint16_t crc16_table[] = {0x0000, 0x1081, 0x2102, 0x3183, 0x4204, 0x5285,
                             0x6306, 0x7387, 0x8408, 0x9489, 0xa50a, 0xb58b,
                             0xc60c, 0xd68d, 0xe70e, 0xf78f};

    size_t length = input_data.size();
    size_t iterator = 0;
    while (length--) {
        crc =
            (crc >> 4) ^ crc16_table[(crc & 0xf) ^ (input_data.at(iterator) & 0xf)];
        crc =
            (crc >> 4) ^ crc16_table[(crc & 0xf) ^ (input_data.at(iterator) >> 4)];
        iterator++;
    }

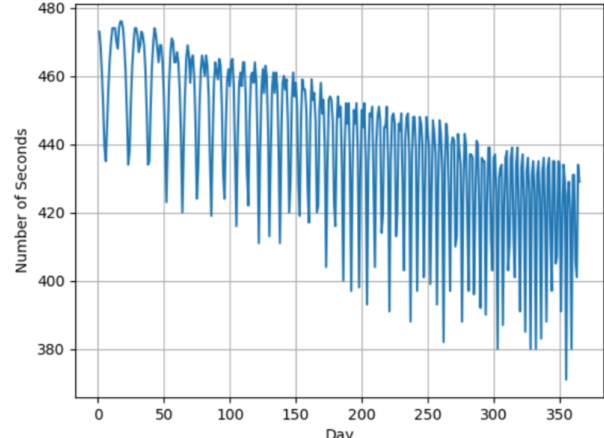
    return (~crc);
}
```

B.7 Data Downlink Storage

In order to validate that we have enough memory to store the scientific data that we have, we need to calculate how much data that will need to store.



(a) Maximum Consecutive Time of Non-Visibility



(b) Minimum Consecutive Time of Visibility

Figure 117: Consecutive Times of Visibility

Figure 117a shows the maximum time per day of non visibility across 12 months. As we want to cover for our worst case, we will take T_{max} as 47,000 seconds. Figure 117b shows the minimum time per day of visibility with the ground station also over 12 months. Once again covering for worst case, this gives us T_{min} as ≈ 375 seconds, or roughly 6 minutes of visibility. Giving an extremely generous room for error of 75 seconds to establish a connection, send WOD, etc, the following amount of data could be transmitted per view.

$$\text{Amount of data} = R_D \cdot 300 = 2.22 \text{ Mb}$$

This means that the maximum amount of data stored can be 2.22 Mb. As each data recording is equivalent to 40 bytes, this means the amount of science recordings that we can is

$$\text{Amount of recordings} = \frac{2220000}{40} = 55500 \text{ recordings}$$

Thus in order to not go over this limit, we would be required to sample at a max speed of:

$$\text{Sampling Rate} = \frac{T_{max} + T_{min}}{\text{Amount of recordings}} = 0.8536 \text{ Samples/s}$$

This allows us to accurately predict the coverage. As the maximum speed is 10.5 km/s, we can *at least* achieve a coverage of:

$$\text{Coverage} = v_{max} \cdot \text{Sampling Rate} = 8.96 \text{ km}$$

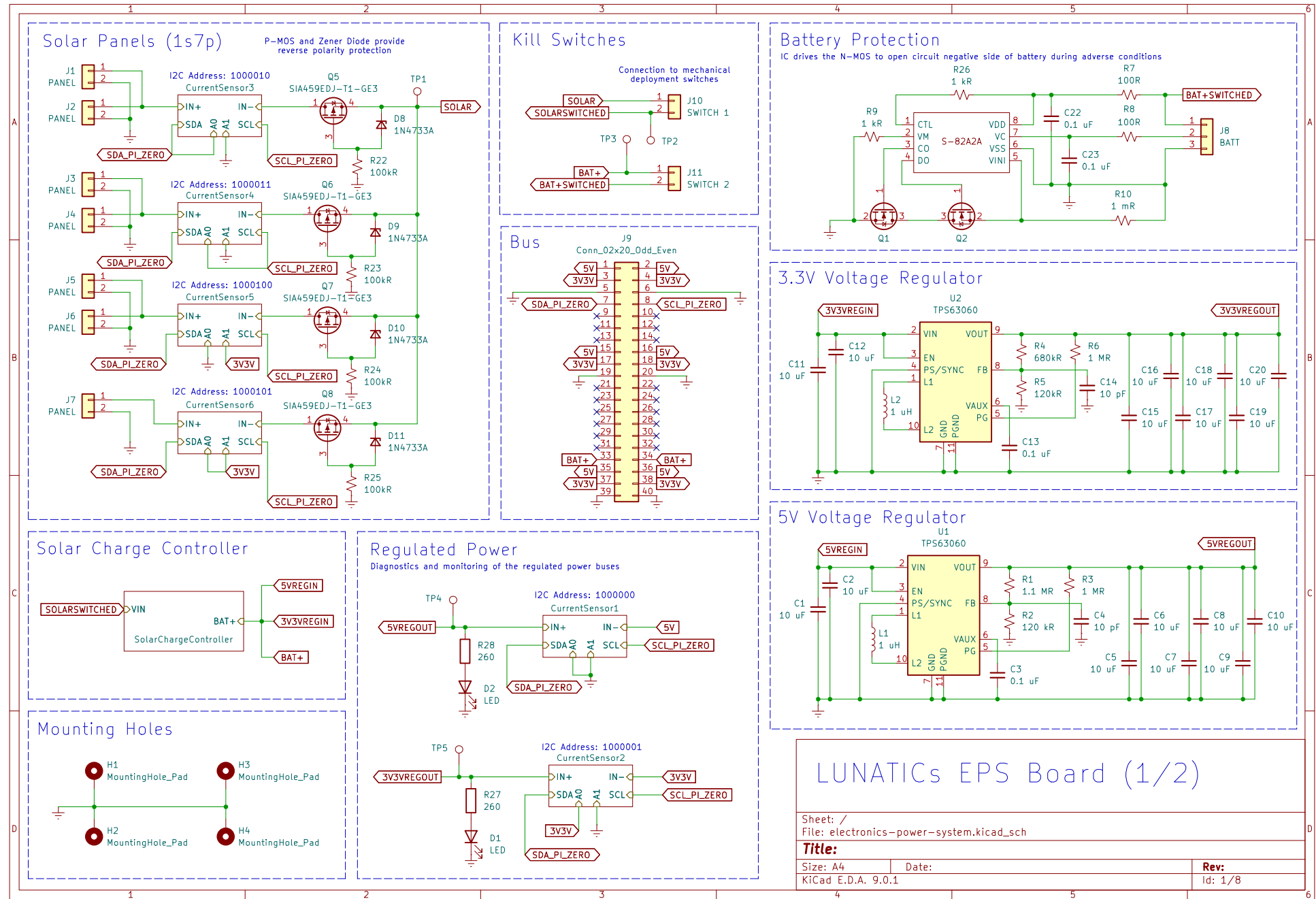
Which comfortably satisfies the requirement of P-SCI-01 and P-PAY-03.

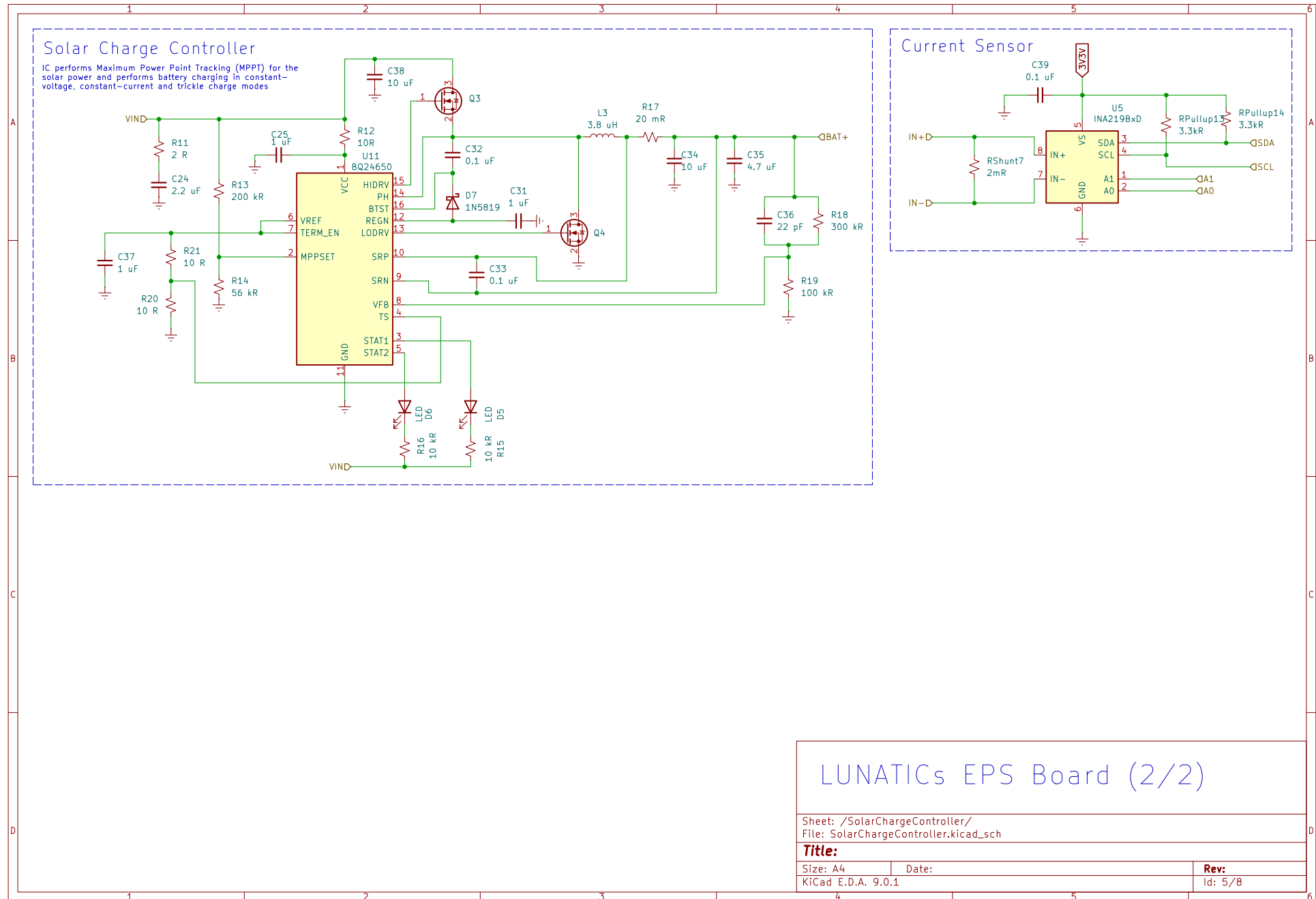
B.8 Code repository

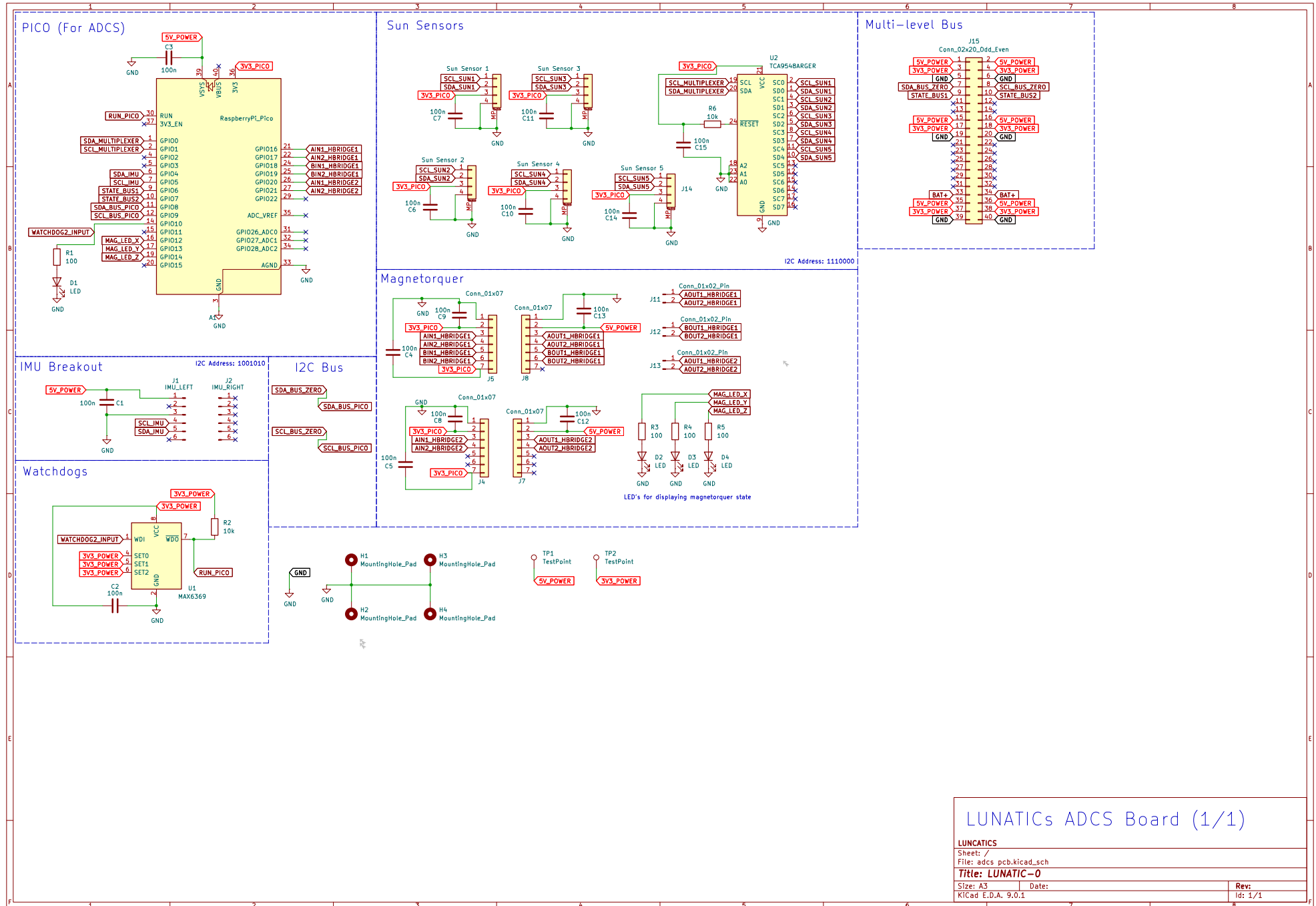
Code for analysis, simulation and plotting data can be found in our Github Repository

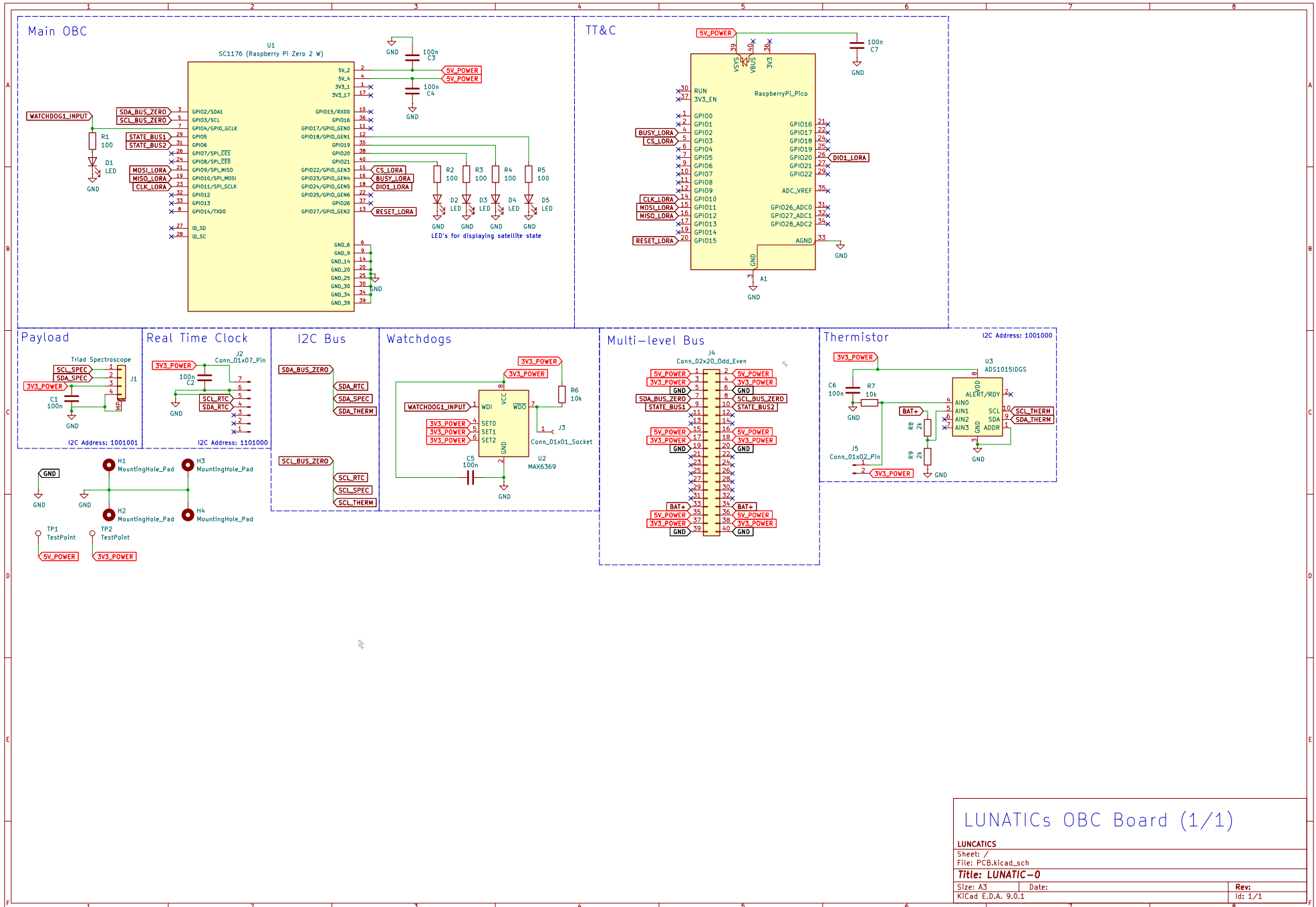
B.9 Electrical Diagrams











B.10 CubeSat Overview Spreadsheet



LUNATICS-0 Design Overview Spreadsheet

Note: Please answer the following questions underneath each cell. And please do not modify the template.

CubeSat Info																						
Reference number	CubeSat name	Lead institute	Country																			
	LUNATICS-0	University of Sydney	Australia																			
Structural Subsystem																						
In-House Development / Procurement	Company / Organization	Total mass with contingency (grams)	Size (2U / 3U)	Sensor Payload (INMS, FIPEX, mNLP or N/A)	Other Payload	Triad AS7265x Spectroscopic Sensor																
In-House Development	University of Sydney	2403.588	2U																			
Attitude Determination and Control Subsystem																						
In-House Development / Procurement	Company / Organization	ADCS offered by Surrey Space Centre (UK)*	Attitude change required by payload or mission scenario	Specify any special requirements on deployment of the CubeSat (if applicable)	Deployables	On board propulsion																
In-House Development	University of Sydney	No	No	NA	No	NA	NA	No onboard propulsion	NA	NA	NA											
Electrical Power Subsystem																						
In-House Development / Procurement	Company / Organization	Overall efficiency of the EPS (%)	Number of solar cells	Battery capacity (Wh)																		
In-House Development	University of Sydney	78	7	21.2																		
On-board Computer and On-board Data handling Subsystem																						
In-House Development / Procurement	Company / Organization																					
In-House Development	University of Sydney																					
Communication Subsystem																						
In-House Development / Procurement	Company / Organization	AX.25	Protocol (if not AX.25)	Uplink		Downlink																
In-House Development	University of Sydney	Yes		Modulation	Frequency (MHz)	Data Rate (bps)	Modulation	Frequency (MHz)	Data Rate (bps)	S/C transmit power (mW)												
				BPSK	437.075	9600	BPSK	437.075	9600	2000												
Ground Segment																						
Satellite Control Software offered by EPFL**		Ground Station							Mini-Network													
No	33.8852	151.1801	1	Yes	Yes	No			Plan to use mini-ground station network***	Have identified mini-network partners	Mini-network partner #1	Mini-network partner #2										
Thermal Control Subsystem																						
In-House Development / Procurement	Company / Organization	Passive / Active																				
In-House Development	University of Sydney	Passive																				
Legal Aspects																						
Agree to have space object registration of the CubeSat through VKI in Belgium	Agree to have frequency allocation through VKI in Belgium?																					
Yes	Yes																					

* The ADCS from SSC is customized for the QB50 project. It is able to meet the QB50 attitude requirements but there are certain limitations.

** The Satellite control Software (SCS) is a ground segment architecture provided by EPFL free of charge for the teams wishing to use it.

*** Mini ground station network is considered to be a network of about 3 to 5 ground stations. The SCS from EPFL has the capability to form a ground station network. Therefore, teams that choose to use the SCS from EPFL are encouraged to collaborate with each other to form a network of 3 to 5 ground stations that is geographically well distributed.

LUNATICS-0 Bill of Materials

Note:

- Please indicate if there are any ITAR components. If so, please indicate the process which is being used to ensure that it will not be problematic.
 - The level of detail in the BOM should be to the degree it can be disassembled. For non-structural components, the material of the board is sufficient (it is not necessary to include the components on the board).
 - Please specify in the comments column if any material is highly degradable or requires special handling instructions (i.e pressurized vessels, propellants).

Component	Material	Shelf Life (in ambient conditions, if applicable)	Quantity	Comments (specify if highly degradable or requires special handling instructions)
Structural Subsystem				
CubeSat Chassis	Aluminum 6061-T6	>20 yrs	1	External painted with titanium dioxide white paint
Deployment Switch	-	>5 yrs	1	Moisture sensitive components
Attitude Determination and Control Subsystem				
BNO085 9DOF IMU Fusion Breakout Board	-	>5 yrs	1	Moisture sensitive components
VEML7700 Lux Sensor	-	>5 yrs	5	Moisture sensitive components
Raspberry Pi Pico H	-	>5 yrs	1	Moisture sensitive components
Magnetotorquers	-	>5 yrs	3	
DRV8835 Dual Motor Driver Carrier	-	>5 yrs	2	Electrostatic charge sensitive components
Electrical Power Subsystem				
Samsung Battery INR18650-35E Li-Ion	Li-Ion	36 months	2	Component is combustible, handle with care
SolarPanelSeedStudio1W	Mono-crystalline	>5 yrs	7	Degradable if shorted, handle with care
EPS PCB	Copper	-	1	Moisture sensitive components
On-board Computer and On-board Data Handling Subsystem				
Raspberry Pi Pico	-	>5 yrs	1	Moisture sensitive components
Raspberry Pi Zero	-	>5 yrs	1	Moisture sensitive components
DS3231M MEMS Precise RTC	-	>5 yrs	1	Moisture sensitive components
ADCs PCB	-	-	1	Moisture sensitive components
OBG PCB	-	-	1	Moisture sensitive components
Communication Subsystem				
VHF/UHF Transceiver	-	>5 yrs	1	Moisture sensitive components
UHF Antenna	-	>5 yrs	1	Moisture sensitive components
Thermal Subsystem				
Mylar layers	-	5-10+ years	1	-
Kapton tape	-	5 years	1	
Space Grade titanium dioxide white paint	-	5 years	1	
Payload				
Spectroscopy Sensor AS7265x	-	>5 yrs	1	-

ITAR export restricted (Yes, No)	Export license for launch in Brazil obtained (Yes, No)	Date
No	No	2/5/2025
No	No	3/5/2025
No	No	3/5/2025
No	No	1/5/2025
No	No	1/5/2025
No	No	1/5/2025
No	No	2/5/2025
No	No	2/5/2025
No	No	3/5/2025
No	No	2/5/2025

LUNATICS-0 Mass Budget

Note that components that are COTS have a contingency of 0.1 of the mass and in house developed components are 0.2.

LUNATICS-0 Power Budget

Note: Please indicate all the assumptions that were used in calculating the power budget. Please note that the worst case attitude should be considered for the power generation in the modes that have no attitude control (i.e Safe mode).

		Assumptions
Altitude (km)		380
Albedo (%)		35
Attitude		Inertial sun stare of the smallest face
Orbit (minutes)		95
Power per solar cell (W)		0.75
Any other assumptions		

			Average Duty Cycle by Mode (%)							
Loads	Power Consumption (W)	Number of Units ON	Safe mode	Nominal mode	Detumble Mode	Pointing Mode	Payload Mode	TRX Mode	Launch	Initialise
RP Zero	0.165	1	75	100	100	100	100	100	0	75
RP Pico	0.55	1	75	100	100	100	100	100	0	75
3.3V Reg	0.055	1	100	100	100	100	100	100	0	100
5V Reg	0.055	1	100	100	100	100	100	100	0	100
IMU	0.046	1	50	100	100	100	100	50	0	0
Magnetorque	2.5	1	0	0	100	100	0	0	0	0
H-Bridge	0	3	0	0	100	100	0	0	0	0
Sun Sensors	0.0006	5	100	100	100	100	100	100	0	0
Spectrometer	0.33	1	0	0	0	0	100	0	0	0
Transceiver	2.2	1	5	5	0	0	0	75	0	0
Antenna	0	1	5	5	0	0	0	75	0	0
Sum loads (W)			0.78	0.98	3.37	3.37	1.20	2.50	0.00	0.65
Efficiency			0.78	0.78	0.78	0.78	0.78	0.78	0.78	0.78
Power Consumed (W)			1.00	1.26	4.33	4.33	1.54	3.21	0.00	0.83
Power Generated (W)			1.50	1.50	1.50	1.50	1.50	1.50	1.50	1.50
Power Margin (%)			33.14	15.90	-188.38	-188.38	-2.91	-113.76	100.00	44.76

LUNATICS-0		NOTE	LUNATICS-0	Date Data Last Modified:
Uplink Command Budget:		Version: 2.5.5		2016 October 20
Parameter:	Value:	Units:	Comments:	
Ground Station:				
Ground Station Transmitter Power Output:	150.0	watts	This value is transferred from "Transmitters" W/S, Cell [E15].	
In dBW:	21.8	dBW	Transmitter power expressed in dB above one watt	
In dBm:	51.8	dBm	Transmitter power expressed in dB above one milliwatt	
Ground Stn. Total Transmission Line Losses:	3.6	dB	This value is transferred from "Transmitters" W/S, Cell [I33]	
Antenna Gain:	16.3	dBi	This value is selected at "Antenna Gain" W/S, Cell [E11]	
Ground Station EIRP:	34.4	dBW	Ground Station Effective Isotropic Radiated Power (EIRP) [EIRP=Pt x L1 x Ga]	
Uplink Path:				
Ground Station Antenna Pointing Loss:	0.3	dB	This value is calculated in the "Antenna Pointing Losses" W/S, and transferred from Cell [K43]	
Grid-to-S/C Antenna Polarization Losses:	0.1	dB	This value is calculated in the "Polarization Loss" W/S and is transferred from Cell [F40].	
Path Loss:	152.2	dB	$L_p = 22 + 20\log(D/\lambda)$, Transferred from "Frequency" W/S	
Atmospheric Losses:	2.1	dB	This value is transferred from "Atmos. & Ionos. Losses" W/S, Cell [D23]	
Ionospheric Losses:	0.4	dB	This value is transferred from "Atmos. & Ionos. Losses" W/S, Cell [D47:D50]	
Rain Losses:	0.0	dB	This value should be estimated by the link model operator and place into Cell [B18]	
Isotropic Signal Level at Spacecraft:	-120.0	dBW	This is the signal level received in space in the vicinity of the spacecraft using an omnidirectional antenna.	
Spacecraft (Eb/No Method):				
Eb/No Method				
Spacecraft Antenna Pointing Loss:	0.3	dB	This value is transferred from "Antenna Pointing Losses" W/S, Cell [K63]	
Spacecraft Antenna Gain:	2.0	dBi	This value is selected at "Antenna Gain" W/S, Cell [E24]	
Spacecraft Total Transmission Line Losses:	2.0	dB	This value is transferred from the "Receivers" W/S, Cell [J52]	
Spacecraft Effective Noise Temperature:	261	K	This value is calculated in the "Receivers" W/S and Transferred from Cell [J67]	
Spacecraft Figure of Merit (G/T):	-24.1	dB/K	$G/T = G_a - 10\log(T_s)$. This is the ultimate measure of the receiver's performance.	
S/C Signal-to-Noise Power Density (S/No):	8600	bps	Boltzman's Constant:	-228.6 dBW/K/Hz
System Desired Data Rate:	39.8	Mbps	Operator selects this value. Be Careful! This is the data rate, not the symbol rate.	
In dBHz:	45.7	Hz	This is simply $= 10\log(R)$; R= data rate	
Command System Eb/No:				
Demodulation Method Selected:	BPSK		Values selected in "Modulation-Demodulation W/S, Cell [E3]	
Forward Error Correction Coding Used:	None		Value selected in "Modulation-Demodulation" W/S, also Cell [E3]	
System Allowed or Specified Bit-Error-Rate:	1.0E-06		The selected value is transferred from the "Modulation-Demodulation W/S, Cells [E6:E23]	
Demodulator Implementation Loss:	1.0	dB	This value is transferred from the "Modulation-Demodulation W/S, Cell[E25]	
Telemetry System Required Eb/No:	10.5	dB	The selected value is transferred from the "Modulation-Demodulation W/S, Cells [F6:F23]	
Eb/No Threshold:	11.5	dB	This is the result of the "Modulation-Demodulation" W/S and is transferred from Cell [H32]	
System Link Margin:	32.2	dB		
Spacecraft Alternative Signal Analysis Method (SNR Computation):			NOTE:	
SNR Method				
Spacecraft Antenna Pointing Loss:	0.3	dB	This value is transferred from "Antenna Pointing Losses" W/S, Cell [K63]	
Spacecraft Antenna Gain:	2.0	dBi	This value is selected at "Antenna Gain" W/S, Cell [E24]	
Spacecraft Total Transmission Line Losses:	2.0	dB	This value is transferred from the "Receivers" W/S, Cell [J52]	
Spacecraft Effective Noise Temperature:	261	K	This value is calculated in the "Receivers" W/S and Transferred from Cell [J67]	
Spacecraft Figure of Merit (G/T):	-24.1	dB/K	$G/T = G_a - 10\log(T_s)$. This is the ultimate measure of the receiver's performance.	
Signal Power at Spacecraft LNA Input:	-120.9	dBW	$P_s = P_{iso} \cdot G_a \cdot L_p \cdot L_t$. This is the signal power that has arrived at the ground station receiver.	
Spacecraft Receiver Bandwidth:	5.000	Hz	Signal Spectrum Must Pass Through This Data Filter.	
Spacecraft Receiver Noise Power (Pn = kTB)	-167.4	dBW	$P_n = K + 10\log(T_b) + 10\log(B)$. This is the total noise power arriving at the ground station receiver.	
Signal-to-Noise Power Ratio at G.S. Rcvr:	46.5	dB	$P_s/P_n = P_s[dBW] - P_n[dBW]$	
Analog or Digital System Required S/N:	14.4	dB	If system is digital, use values from "Modulation-Demodulation" W/S. If analog, use appropriate value from text book.	
System Link Margin	32.1	dB		

LUNATICS-0			NOTE:	LUNATICS-0			NOTE:	LUNATICS-0			Date Data Last Modified:
Downlink Telemetry Budget:				Version 2.5.5							2016 October 20
Parameter:	Value:	Units:		Comments:							
Spacecraft:											
Spacecraft Transmitter Power Output:	2.0	watts		This value is transferred from "Transmitters" W/S, Cell [E50]							
	-37.0	dBW		Transmitter power expressed in dB above one milliwatt							
Spacecraft Total Transmission Line Losses:	2.2	dB		This value is transferred from "Transmitters" W/S, Cell [E68]							
Spacecraft Antenna Gain:	2.0	dB		This value is selected at "Antenna Gain" W/S, Cell [E41]							
Spacecraft EIRP:	2.8	dBW		Spacecraft Effective Isotropic Radiated Power (EIRP) [EIRP=Pt x Lf x Ga]							
Downlink Path:											
Spacecraft Antenna Pointing Loss:	0.2	dB		This value is calculated in the "Antenna Pointing Losses" W/S, and transferred from Cell [K85]							
S/C-to-Ground Antenna Polarization Loss:	0.1	dB		This value is calculated in the "Polarization Loss" W/S and is transferred from Cell [F60].							
Path Loss:	15.2	dB		$L_p = 22 + 10\log(f_s)$, Transformed from Frequency W/S							
Atmospheric Loss:	2.1	dB		This value is transferred from "Atmos. & Ions. Losses" W/S, Cell [D23].							
Ionospheric Loss:	0.4	dB		This value is transferred from "Atmos. & Ions. Losses" W/S, Cell [D47:050]							
Rain Loss:	0.0	dB		This value should be estimated by the link model operator and place into Cell [B18].							
Isotropic Signal Level at Ground Station:	-149.2	dBW		This is the signal level received at the Earth in the vicinity of the ground station using an omnidirectional antenna.							
Ground Station (EbNo Method):											
Ground Station Antenna Pointing Loss:	0.2	dB		This value is transferred from "Antenna Pointing Losses" W/S, Cell [K102]							
Ground Station Antenna Gain:	14.1	dB		This value is selected at "Antenna Gain" W/S, Cell [E58]							
Ground Station Total Transmission Line Losses:	2.0	dB		This value is transferred from the "Receivers" W/S, Cell [I123]							
Ground Station Effective Noise Temperature:	510	K		This value is calculated in the "Receivers" W/S and Transferred from Cell [J138]							
Ground Station Figure of Merit (G/F):	-15.0	dB/K		$G/F = G_s - L_s + 10\log(T_s)$. This is the ultimate measure of the receiver's performance.							
G.S. Signal-to-Noise Power Density (S/N):	8.1	dB		Boltzman's Constant: -228.6 dBW/K/Hz							
System Desired Data Rate:	9.6	bps		Operator selects this value. Be Careful! This is the data rate, not the symbol rate.							
Telemetry System Eb/No for the Downlink:	7.0	dB		This is simply $= 10\log(R_s)$; R= data rate							
Demodulation Method Selected:	BPSK			Values selected in "Modulation-Demodulation W/S, Cell [E30]							
Forward Error Correction Coding Used:	None			Value selected in "Modulation-Demodulation" W/S, also Cell [E30]							
System Allowed or Specified Bit-Error-Rate:	0.0E-05			The selected value is transferred from the "Modulation-Demodulation W/S, Cells [E33:E50]							
Demodulator Implementation Loss:	0	dB		This value is transferred from the "Modulation-Demodulation W/S, Cell [E52]							
Telemetry System Required Eb/No:	9.6	dB		The selected value is transferred from the "Modulation-Demodulation W/S, Cells [F33:F50]							
Eb/No Threshold:	9.6	dB		This is the result of the "Modulation-Demodulation" W/S and is transferred from Cell [H32]							
System Link Margin:	11.7	dB									
Ground Station Alternative Signal Analysis Method (SNR Computation):											
SNR Method											
Ground Station Antenna Pointing Loss:	0.2	dB		This value is transferred from "Antenna Pointing Losses" W/S, Cell [K102]							
Ground Station Antenna Gain:	14.1	dB		This value is selected at "Antenna Gain" W/S, Cell [E58]							
Ground Station Total Transmission Line Losses:	2.0	dB		This value is transferred from the "Receivers" W/S, Cell [I123]							
Ground Station Effective Noise Temperature:	510	K		This value is calculated in the "Receivers" W/S and Transferred from Cell [J138]							
Ground Station Figure of Merit (G/F):	-15.0	dB/K		$G/F = G_s - L_s + 10\log(T_s)$. This is the ultimate measure of the receiver's performance.							
Signal Power at Ground Station LNA Input:	-140.4	dBW		$P_s = P_{av} + G_s - L_s$. This is the signal power that has arrived at the ground station receiver.							
Ground Station Receiver Bandwidth (B):	500	Hz		Signal Spectrum Must Pass Through This Data Filter							
G.S. Receiver Noise Power (Pn = kTB)	-174.5	dBW		$P_n = K + 10\log(T_s) + 10\log(B)$. This is the total noise power arriving at the ground station receiver.							
Signal-to-Noise Power Ratio at G.S. Rcvr:	-14.1	dB		$P_s/P_n = P_s(dBW) - P_n(dBW)$							
Analog or Digital System Required S/N:	9.6	dB		If system is digital, use values from "Modulation-Demodulation" W/S. If analog, use appropriate value from text book.							
System Link Margin	24.5	dB									

NOTE: